# SOLID-PHASE ISOTOPE HARVESTING: HARVESTING RADIOISOTOPES FROM BEAM IRRADIATED TUNGSTEN, BORON, AND LUTETIUM

By

Samridhi Satija

A DISSERTATION

Submitted to
Michigan State University
in partial fulfillment of the requirements
for the degree of

Chemistry – Doctor of Philosophy

2024

## ABSTRACT

During the operation of radioactive ion-beam facilities, such as the recently decommissioned National Superconducting Cyclotron Laboratory (NSCL) and the newly operational Facility for Rare Isotope Beams (FRIB), many radioisotopes get deposited along beamlines in components such as in mass-separator slits, fragment catchers, and beam dumps. The techniques to recover the by-product radioisotopes from these components is called 'solid-phase isotope harvesting' or 'isotope mining' and can help to meet the increasing demand for radioisotopes in a variety of fields. This technique offers a unique approach to access rare isotopes that are often challenging to produce using conventional methods. A comparative analysis with aqueous-phase (harvesting from water) and gaseous-phase (harvesting from gases) methods also shows the distinct advantages of solid-phase harvesting, including simplified chemistry and enhanced flexibility in collection location and material choice.

This work comprises four primary aims, each aiming at advancing the understanding and implementation of solid-phase isotope harvesting. The first is to establish the of proof-of-concept for solid-phase isotope harvesting, with a specific focus on the extraction of $^{88}$Zr from irradiated tungsten foils. This aim seeks to demonstrate the feasibility and efficacy of solid-phase harvesting, and enables comparison with aqueous-phase harvesting. The second aim involves the harvesting of $^{172}$Hf from a tungsten 'heavy-met' alloy beam-blocker/beam-dump that was used to stop unused beams at NSCL. The beam blocker was retrieved after the NSCL facility was decommissioned and was chemically processed to extract $^{172}$Hf and to develop a $^{172}$Hf/$^{172}$Lu generator. This work utilizes the proof of concept study from the first aim and exhibits harvesting from a decommissioned component. The third aim involves the production of $^{172}$Hf from the conventional method of irradiating natural lutetium foil targets at the Brookhaven Linear Isotope Producer

(BLIP), coupled with the development of methodologies for extracting $^{172}$Hf followed by creation of several $^{172}$Hf/$^{172}$Lu generators. This aim helps to compare radionuclides produced by a conventional technique to those obtained from the isotope harvesting efforts shown in the second aim. The fourth aim demonstrates production and separation of $^{7}$Be from natural and enriched boron targets, followed by chemical separation, $^{7}$Be source preparation and $^{7}$Be beam delivery to users at NSCL. This aim demonstrates the practical application of solid-phase isotope harvesting by producing a specific radionuclide for use in scientific experiments.

Collectively, this work describes the radioanalytical techniques and chemical methodologies used in the extraction and purification of embedded radioisotopes from beam-irradiated solid materials of tungsten, boron and lutetium. These four aims have together laid the groundwork for developing robust methodologies to extract and separate long-lived radioisotopes that will accumulate along the FRIB beamline. Ultimately, this work aims to enable solid-phase isotope harvesting on a larger scale at FRIB, when FRIB is operational at full beam power, and at other similar ion-beam facilities. The methods described herein allow harvesting of difficult-to-produce byproduct radionuclides without the need for dedicated beamtime at FRIB.

Dedicated to my loving parents Kanti Raman and Sunita Satija, and younger sister Navani Satija for their unconditional love and support

## ACKNOWLEDGEMENTS

Reflecting on my PhD journey fills me with profound gratitude for the many remarkable individuals who have contributed to my success. First and foremost, I want to extend my deepest gratitude towards my parents and my first teachers in life, Kanti Raman and Sunita Satija and for their unwavering support throughout. The sacrifices they have made to provide the best of everything for me and my sister is still beyond my comprehension and conscious realm. I'm immensely grateful for all the difficult times they stood by me, checked on me every day and every night on video calls for the past five years and made me feel like I was never away from home. I'm beyond blessed to have them as my parents. To my sister, Navani, thank you for always acting like the little 'elder sister' taking care of everything while I was here doing my PhD, I'll be forever indebted. You're simply the best sister and friend I could ask for.

Next, my heartfelt thanks to my PhD advisor, Dr. Greg Severin. Thank you for being infinitely patient and considerate throughout these five years, every time I faltered. You're a great scientist and I've learnt a lot from you in that regard, but you're an even better person, and I've been fortunate to learn from your example in that aspect too. My grad school experience has been exceptional and your support along with the work culture you've ensured in our lab is a huge reason behind it. Looking back, joining your lab was undoubtedly one of the best decisions of my life. I also want to extend a huge thank you to my committee members, Dr. Greg Swain, Dr. Sean Liddick and Dr. Kyle Brown for being so accommodating and always encouraging.

I must express my gratitude to my labmates in this wonderful journey. Dr. Katharina Domnanich, who's been by my side since Day 1. You're the best mentor and a really great friend who I've learnt a great deal from. Thank you for your encouragement, it meant the world to me. Our 'harry potter nights', coffee and food celebrations are memories which will always hold a

very special place in my heart. Thank you, Dr. Chirag Vyas for all your guidance, both professionally and personally all these years. You've always been like an elder brother to me and I knew I could always count on you to solve anything. A big thank you to Chloe, Vlad, and Scott for all the help with so many different and incredibly time consuming experiments, especially when I had gone to BNL. I am really going to miss all the fun we had these years, inside and outside the lab. Thank you to Jose, Tracy, Wes, and Xyla as well for all the assistance I received for all the experiments, you have all been the best labmates ever.

A special thanks to the team at BNL - Dr. Cathy Cutler, Dr. Dmitri Medvedev, Vanessa, Michael, Leah, Jasmine and Courtney. I am grateful for the opportunity to work alongside you for 8 months. It was great to see the National Lab set up for the first time, and you all made it such a special experience for me. Thank you to the BMIS team at NSCL, especially Dr. Chandana Sumithrarachchi, for providing the data I needed even in a short time. I'd also like to thank my advisor, Dr. Sameer Sapra and Dr. Arkajyoti Chakrabarty while I was in IIT, for helping me gain research experience that made me want to pursue PhD at MSU.

To my friends - Debashree, Aamna, Atif, Nidhi, Eagle, Ankita, Haritha, Sunanda, Souvik, Avirup, Himanshu, Benji, Apurva, and Paige - a big thank you for being so kind, for being my family away from home and for all the fun times we had, cooking and celebrating everything. All of you have played a big role in keeping me sane, motivated, and going.

Finally, I am thankful to God, who is omnipotent and omnipresent, and from whom I derive the energy and guidance to navigate life's challenges.

## TABLE OF CONTENTS

# CHAPTER 1: INTRODUCTION

## 1.1 Radioactive ion-beam facilities – NSCL and FRIB

At radioactive ion-beam research facilities, such as the recently decommissioned National Superconducting Cyclotron Laboratory (NSCL) and the recently commissioned Facility of Rare Isotope Beams (FRIB), primary beams of heavy ions are accelerated with the aim to produce secondary radioactive beams for nuclear physics experiments. In this process, a vast array of exotic radionuclides gets produced that finds applicability in multiple fields enabling basic and applied research [1]. Some of the fields where these rare isotopes prove indispensable are medicine, biochemistry, plant biology, astrophysics, stockpile stewardship science, and materials science [1].

The operation of facilities like FRIB and NSCL will result in a significant advancement in rare isotope research capabilities resulting from the production of a broad distribution of radioactive isotopes. FRIB will exhibit intensities from the fragmentation of 400-kW primary beams with energies of about 200 MeV/nucleon [2], [3], [4]. This results in the production of 80% of all known isotopes of elements, and very recently five new isotopes were discovered that had never been seen on the surface of the earth [5]. This is indicative of the promise of FRIB and rare isotope beam science.

During the operation of these radioactive ion-beam facilities, and generally for other facilities as well, byproduct radioisotopes get deposited at multiple places along the beamline, such as mass-separator slits, fragment catchers, beam-dumps and other locations. Over time, this process leads to a considerable accumulation of exotic radionuclides at these locations. These components accumulate long-lived radionuclides throughout their service period and typically have replacement time in the order of years. By the time these components are removed from

operation, potentially useful activities of radionuclides have been built up. In most cases, these accumulated radionuclides are difficult to produce through other conventional means and recovering and extracting them from decommissioned components might be the best option for obtaining them.

### 1.2 Isotope harvesting

The accumulated rare isotopes can be chemically extracted and purified using radiochemical techniques in a process known as ‘isotope harvesting’ or ‘isotope mining’. Specifically for this thesis, ‘solid-phase isotope harvesting’ is the focus as it allows access to rare, usually difficult-to-produce radionuclides that find application in a variety of fields, mentioned previously [1], [6], [7]. Other forms of isotope harvesting include the ‘aqueous-phase harvesting’ which is harvesting from irradiated water, and ‘gaseous-phase harvesting’ which is harvesting from activated gases [8], [9].

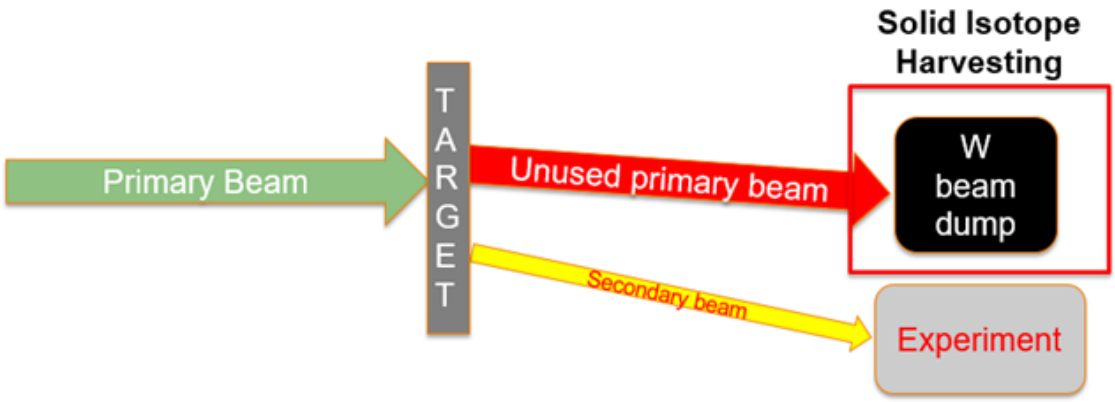


**Figure 1.1:** A simplified schematic showing the process of solid-phase isotope harvesting at the NSCL. Over the last 20 years, primary beams at NSCL have been stopped in a tungsten beam-blocker during the delivery of secondary beams to experimental users. The activation products resulting from the dumped beam are isolated in the process of solid-phase isotope harvesting.

In order to understand how to best implement these novel approaches at FRIB, experiments have been performed at the NSCL, which delivered beams with properties similar to those that are delivered at FRIB, though at lower intensity by several orders of magnitude. A simplified schematic of the process of solid-phase isotope harvesting at the decommissioned NSCL, is shown in **Figure 1.1**. Briefly, before the NSCL was decommissioned, many of the unused nuclides and unused primary beams were embedded into a tungsten 'heavy-met' alloy beam-dump/beam-blocker/beam-stop (referred to as the 'tungsten beam-blocker' herein). The decades-long accumulation of embedded and activation-product radionuclides in the tungsten beam blocker provided a unique opportunity to study isotope harvesting from solid materials. Similarly, it is expected that materials in the FRIB beamlines will become available for harvesting as they are replaced over the course of many years of operation. All of the solid components shown in **Figure 1.2** are potential locations in the FRIB beamline that will accumulate radionuclides continuously without the need for a dedicated beamtime [10].

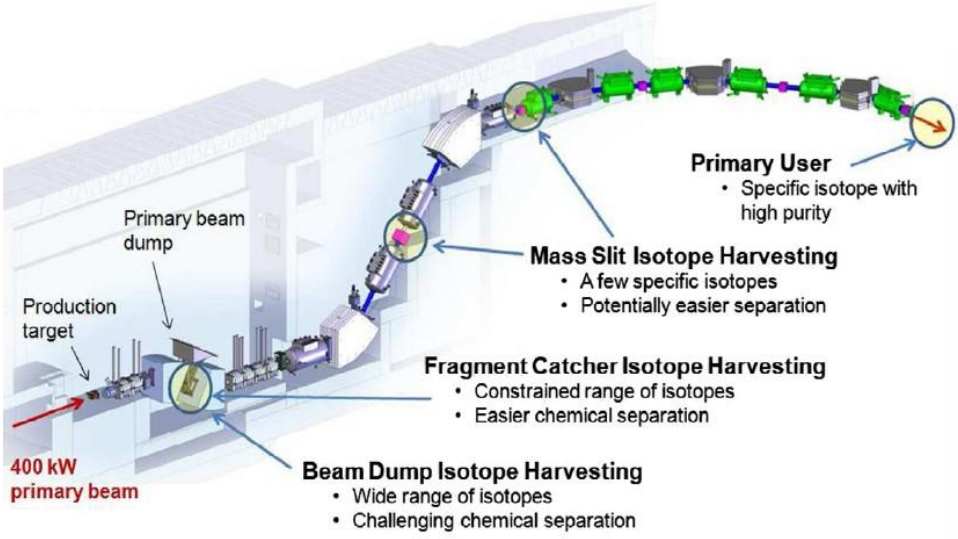


**Figure 1.2:** Schematic of the potential isotope harvesting locations at FRIB that includes beam-dump, fragment catchers, and mass slits. Reprinted from ref [10] with permission from Elsevier.

While there are many advantages of building an 'Isotope harvesting program' for FRIB, some notable ones are as follows - this is a synergistic process and can keep happening without interrupting the beam delivery for physics experiments. Secondly, traditional facilities for isotope production, such as nuclear reactors and medical cyclotrons, face limitations in terms of the resources they can allocate to producing specific radionuclides. This restricts both the quality and quantity of the produced isotopes [1]. It is also a good approach to access hard-to-produce radionuclides from conventional methods.

1.2.1 Isotope harvesting from aqueous and gaseous phases

So far, aqueous isotope harvesting approaches have been investigated extensively at the NSCL, in a series of experiments carried out by delivering NSCL beams into a dedicated aqueous endstation. An experiment facilitating the collection from primary beam of $^{48}$Ca and directing these unused primary beams to an aqueous target and replacing the solid tungsten beam-blocker already present there has been demonstrated [11]. Mastren et al. studied harvesting $^{67}$Cu using an aqueous beam stop built by Pen et al. at the NSCL demonstrating the recovery of the radiochemically pure $^{67}$Cu [4], [12], [13]. This isotope finds great relevance for radiopharmaceutical applications. Loveless et al. investigated harvesting experiments utilizing the same aqueous beam stop for recovery of $^{48}$V [14]. These proof-of-concept studies have demonstrated the importance of aqueous harvesting for providing rare isotopes which are difficult to produce by conventional methods. In parallel, the harvesting of gaseous radionuclides has been another main focus. Noble gas radionuclides that were created in the water targets have been transferred into the gas phase and trapped on selective traps. Recently, the collection of krypton radioisotopes to generate $^{76}$Br and $^{77}$Br depicted successful demonstration of the feasibility of gas-phase isotope harvesting from irradiated accelerator cooling-water [15].

Another promising avenue under investigation is using Metal-Organic Frameworks (MOFs) that have the potential to increase the selectivity of krypton or other noble gas capture to increase collection efficiencies, especially at FRIB. The research suggests that when FRIB reaches full power, substantial quantities of these above-mentioned isotopes could be harvested daily, highlighting the need for these proof-of-concept experiments.

1.2.2 Solid-phase isotope harvesting

Just like the aqueous and gaseous phase harvesting efforts, solid-phase isotope harvesting at NSCL/FRIB has a great potential to provide access to rare isotopes. Similar efforts in solid phase harvesting at other facilities worldwide have been highly successful. Among one of the first such efforts, the ERAWAST (Exotic Radionuclides from Accelerator Waste for Science and Technology) initiative at the Paul Scherrer Institut (PSI) successfully extracted the long-lived isotopes $^{44}$Ti ($t_{1/2}$ = 59.1 y), $^{26}$Al ($t_{1/2}$ = 7.17 x $10^5$ y), $^{53}$Mn ($t_{1/2}$ =3.74 x$10^6$ y), $^{60}$Fe ($t_{1/2}$ = 2.62 x$10^6$ y) and $^{59}$Ni ($t_{1/2}$ = 7.6 x$10^4$ y) that are of importance to astrophysics experiments from a copper beam dump [16], [17], [18], [19], [20], [21], [22]. This copper beam dump was a part of accelerator waste generated at PSI. The extracted $^{60}$Fe ($t_{1/2}$ = 2.62 x$10^6$ y) was used for studying the $^{60}$Fe(n, $\gamma$)$^{61}$Fe cross-section and for half-life measurement experiments [17], [23], [24]. In another study, $^{10}$Be ($t_{1/2}$ = 1.51 x$10^6$ y) was extracted from irradiated graphite wheels, and $^{207}$Bi ($t_{1/2}$ = 31.55 y) from an irradiated lead target at PSI [25], [26]. Because of the success of the ERAWAST project, other facilities are also developing programs for the collection of these by-product radionuclides.

For the majority of radioisotopes that will not emerge as gases, aqueous-phase or solid-phase harvesting will be the only feasible way to collect them. Although, in principle, separating radionuclides from the solid materials will be complicated, there are a few instances where solid-

phase harvesting provides a distinct advantage over the aqueous-phase harvesting procedures. In the case of aqueous-phase harvesting, the chemistry gets complicated because, at least at FRIB, there is an enormous stock of water that must be processed for efficient harvesting. In this situation, the radionuclide of interest, present at sub-nanogram scales, would need to be isolated from up to 8000 L water [27], [28]. This renders the extraction of radionuclides that are prone to hydrolysis very difficult. Additionally, there is also the problem of formation of highly oxidative species, such as hydrogen peroxide, from the stopping of high intensity heavy-ion beams in water. This would complicate the collection of radionuclides with sensitive redox chemistry [29], [30].

Additionally, with this kind of volume, the beam products must be concentrated by reducing the volume of the water by evaporation, co-precipitation, or adsorption to a solid phase such as an ion-exchange resin. Whereas in solid-phase harvesting, smaller volumes are required for the dissolution of collectors/targets which considerably simplifies the post-irradiation chemistry. This offers more flexibility in the development of specific methodologies, such as dissolving the collector/target in the appropriate acid matrix that restricts hydrolysis. Solid-phase harvesting is a general method that should work for nearly all chemical species.

Advantages of solid-phase harvesting also includes flexibility in terms of collection location and the collector material. As shown in **Figure 1.2**, the solid collectors can be deliberately placed in various locations along the beamline, allowing the collectors to intercept the beam for a short time and potentially providing access to shorter-lived species. Additionally, beam products will accumulate in solid beam-dumps whenever the facility is in operation and will therefore offer a wide variety of radionuclides. This will potentially require more

sophisticated chemical separation methods to be developed to harvest these short- and long-lived radionuclides.

Many radionuclides that have been identified as being important for astrophysics and stockpile stewardship have half-lives longer than 30 days and will build up over months or years of facility operation. Therefore, in preparation for the large-scale isotope harvesting at FRIB, it was important to investigate solid-phase harvesting approaches at NSCL and establish proof-of-concept procedures. With a focus on solid-phase, this thesis will involve the harvesting of radionuclides from beam irradiated tungsten, boron, and lutetium. Any of these materials can be used to either accumulate radionuclides from FRIB's rare isotope beams, or can be activated themselves by interactions with beams. Depending on the application, materials and irradiation conditions can be selected and matched with appropriate radiochemical processes to provide useful quantities of rare radionuclides for science.

### 1.3 The four aims for this thesis

#### 1.3.1 AIM I - $^{88}$Zr harvesting: Proof of concept study for establishing solid-phase isotope harvesting approaches

Previously, a study by Shusterman et. al. investigated the extraction and collection of $^{88}$Zr and its daughter $^{88}$Y, when a high-energy secondary $^{88}$Zr beam from a 140-MeV/u $^{92}$Mo primary beam was stopped in an aqueous endstation at the NSCL [31]. This was the first study to access the recovery of a Group IV element that is prone to hydrolysis form an aqueous matrix. As a result, recovery efficiency for $^{88}$Zr post chemical processing from aqueous harvesting was only (26±2)%. Another study was aimed at the collection of $^{48}$V, and showed similar low recovery yields of 47% [14]. It was inferred that for radionuclides that exhibit hydrolysis in water such as Zr, Hf, and V, aqueous harvesting presents considerable challenges due to irreversible formation

of hydrolyzed species and their adsorption on container walls. When micromolar concentrations are exceeded for metals, these group IV (Zr and Hf) and V (V) metals tend to exist in tetravalent and pentavalent oxidation states, and form oxide and hydroxide complexes in aqueous conditions that are not highly acidic [32]. Thus, solid-phase isotope harvesting is a viable option here. Additionally, several Zr isotopes are valuable for nuclear science, such as $^{95}$Zr for astrophysics, $^{86}$Zr and $^{89}$Zr for nuclear medicine, and $^{88}$Zr for stockpile-stewardship applications. For example, $^{88}$Zr ($t_{1/2}$ = 83.4 d) with its characteristic 392.87-keV γ ray (emitted with a γ-ray intensity Iγ = 97.29%) is of interest for interpreting data from radiochemical detectors used in underground nuclear tests [33], [34]. Since the United States no longer conducts nuclear tests, the National Nuclear Security Administration (NNSA) uses a science-based assessment called the Stockpile Stewardship Program for maintaining and enhancing the safety and security of the nuclear weapons stockpile [35]. The recently determined large thermal-neutron-capture cross section of $^{88}$Zr, amounting to (8.61 ± 0.69) x$10^5$ barn, represents an important addition to the cross section data of radioactive nuclei required for the Stockpile Stewardship Program [36]. The simplified decay scheme for $^{88}$Zr is shown in **Figure 1.3**. Furthermore, the daughter of $^{88}$Zr, $^{88}$Y ($t_{1/2}$ = 106.6 d) is of interest to the astrophysics community for p-process investigations and for application as a surrogate for the medically relevant $^{90}$Y in research. Its prolonged half-life and the emittance of easily detectable 898.04 and 1836.06 keV gamma rays (Iγ = 93.7% and 99.2%, respectively) enables the performance of tracer studies, instead of directly employing the diagnostic and therapeutic counterpart [37], [38]. Considering the many uses of zirconium and yttrium, it is worthwhile to explore its chemistry from solid-phase perspective.

In this first proof-of-concept experiment, the beamtime at the NSCL was devoted to the fragmentation of a $^{92}$Mo primary beam and the implantation of the formed secondary $^{88}$Zr beam

in diverse collector materials, such as copper, aluminum, gold and tungsten. These materials were deliberately chosen because they are expected to be used as components in FRIB or have already accumulated beam at NSCL. Thereby, the radionuclides of $^{88,89}$Zr, $^{85-88}$Y, and $^{83-86}$Sr were produced along with other species such as $^{90}$Nb and $^{83,84}$Rb. This allowed for the investigation of extraction and collection of $^{88}$Zr and its daughter $^{88}$Y from the solid collector of tungsten by the method of solid-phase harvesting. Many isotopes of Y which is a lanthanide analog have applications in nuclear medicine and batteries, stockpile stewardship, and materials science.

To sum up the AIM I, the main tasks for solid harvesting of $^{88}$Zr involve the development of chemistries needed to purify Zr, Y, and Sr from the collector material of tungsten, development of a solid harvesting endstation for the proof-of-concept experiments at the NSCL, conducting the heavy-ion irradiation of the solid collector materials using NSCL beams followed by the separation of the collected products by implementing the newly-developed techniques.

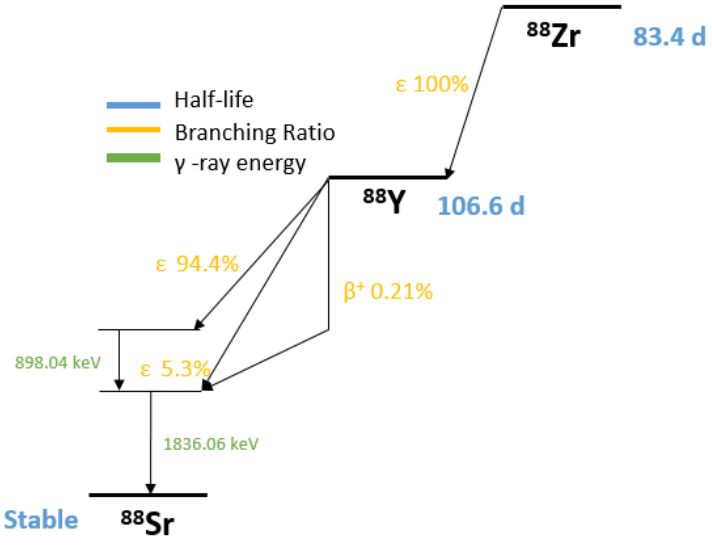


**Figure 1.3:** Simplified scheme for the decay of $^{88}$Zr to produce $^{88}$Y which decays into stable $^{88}$Sr [41].

This proof of concept experiment would provide insight into tungsten and zirconium chemistry, and is particularly important because it will allow comparison to the aqueous collection methods developed for this isotope. This is described in further detail in Chapter 2.

### 1.3.2 AIM II - $^{172}$Hf harvesting from tungsten 'heavy-met' beam-blocker

AIM I served as proof-of-concept for AIM II. The interest in harvesting from the tungsten beam-blocker recovered from the NSCL is due to the presence of radionuclides $^{172}$Hf ($t_{1/2}$ = 1.87 y), and $^{173}$Lu ($t_{1/2}$ = 1.37 y) which are the most abundant after a one-year decay period [39], [40]. Establishing proof of concept methodologies are necessary before attempting harvesting and processing at a higher scale. After achieving AIM I, and having understood the tungsten, zirconium, and yttrium chemistry from the irradiation of the tungsten target in AIM-I, the next step was to process the 'tungsten beam-blocker', and develop separation techniques to primarily separate out $^{172}$Hf from medium Z and high Z radionuclides embedded in the beam blocker. The chemical homologs, $^{88}$Zr and $^{88}$Y, were suitable surrogates for developing separation chemistries (in AIM I) before attempting hafnium and lutetium chemistry from beam-blocker.

This tungsten beam blocker (shown in **Figure 1.4**) was used as a beam stop since 2000. It was water-cooled and located at the exit of the first dipole magnet to block the primary beam (or a primary beam charge state); in the A1900 fragment separator along the beamline. It is an 89-mm (3.5 inches) in length 'heavy-met' alloy (W 95%, Cu 1.5% and Ni 3.5%), 51-mm (2 inches) wide and 102-mm (4 inches) deep. The activity in the beam-blocker (described in more detail in Chapter 3) is due to implantation of radioactive ions and activation from fast secondary light ions and neutrons [41]. Decommissioning of the NSCL had made it possible to harvest isotopes from the beam-blocker which have applications in a number of fields.

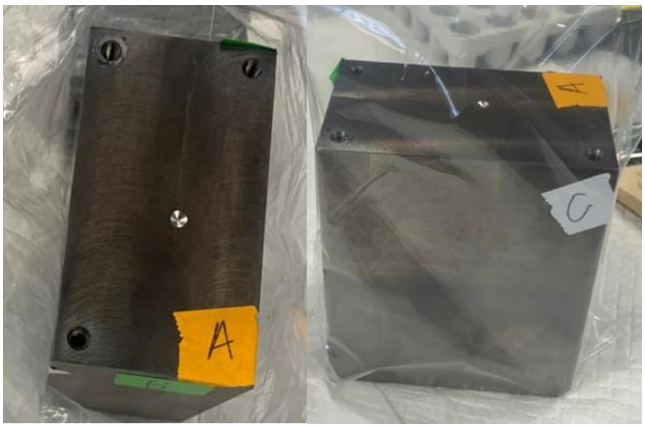


**Figure 1.4:** Different sides of the tungsten 'heavy-met' beam-blocker is shown to provide the reader with dimension estimation.

After the extraction, a $^{172}$Hf/$^{172}$Lu generator was created for application of $^{172}$Lu in Perturbed Angular Correlation Spectroscopy (PAC) described in further detail in Chapter 3. Since the chemistry of zirconium is similar to hafnium and chemistry of yttrium is similar to lutetium, separation techniques developed from the proof-of-concept tungsten irradiation experiment had proved useful. The chemical processing of this beam-blocker at NSCL and potentially the ones when FRIB is in operation in the future could yield substantial quantities of $^{172}$Hf and consequently its daughter, $^{172}$Lu, which finds applicability in several fields. This is described in further detail in Chapter 3.

1.3.3 AIM III - $^{172}$Hf harvesting from lutetium foil target at the Brookhaven Linear Isotope Producer

The third AIM of solid-phase isotope harvesting is to produce $^{172}$Hf from a conventional method of irradiating a natural lutetium foil with protons. This irradiation happened at the Brookhaven Linear Isotope Producer (BLIP) involving the $^{175}$Lu(p,4n)$^{172}$Hf nuclear reaction and was followed by developing chemical methodologies for setting up the $^{172}$Hf/$^{172}$Lu generator from the extracted parent, $^{172}$Hf. A simplified decay scheme is also shown in **Figure 1.5**.

One prime motive of using the solid-phase isotope harvesting approach is to be able to compare separation yields from decommissioned activated material with those that are processed after production from conventional methods, such as after being produced from a cyclotron or reactor. Comparison of the $^{172}$Hf/$^{172}$Lu generator obtained from AIM II and AIM III was also made and is provided in Chapter 4.

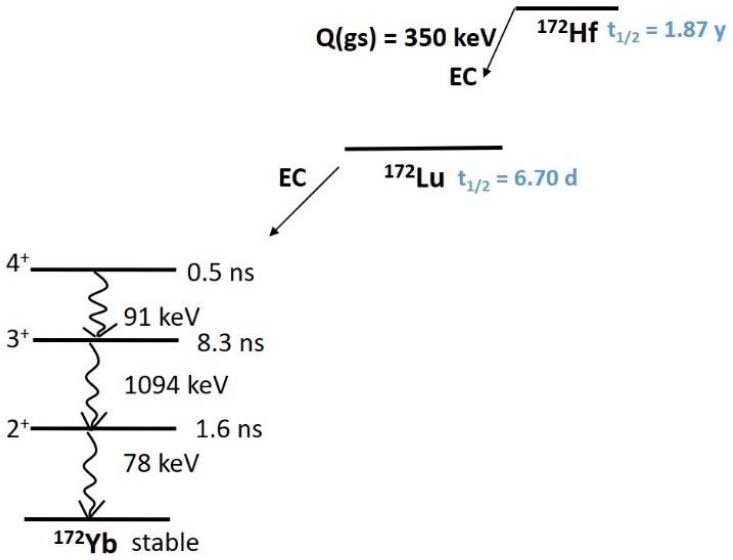


**Figure 1.5:** A simplified decay chain of $^{172}$Hf, $^{172}$Lu, and $^{172}$Yb is shown [43].

### 1.3.4 AIM IV - $^{7}$Be harvesting: Production and separation from boron and beam delivery

Having understood chemistry of the extraction of radionuclides from solid material of tungsten and lutetium in AIM I, II, and III, an opportunity arose for the production and extraction of $^{7}$Be ($t_{1/2}$ = 53.2 d) from a solid natural ($^{10}$B and $^{11}$B) and ($^{10}$B) enriched boron pellet target. This was required to provide the $^{7}$Be beam to experimenters.

This experiment involved investigating the feasibility of the $^{10}B(p,\alpha)^{7}Be$ nuclear reaction (**Figure 1.6**) for the production of $^{7}Be$, carrying out the production at the University of Alabama at Birmingham Cyclotron facility, followed by performing the developed separation methodologies for extracting $^{7}Be$ from the irradiated boron with high purity. This was followed by $^{7}Be$ source preparation for use in the Batch-Mode Ion Source (BMIS) to facilitate the re-accelerator operation at NSCL. The entire pipeline was demonstrated here for creating offline radioactive beams, and the 100% pure $^{7}Be^{4+}$ ion beam was delivered to users.

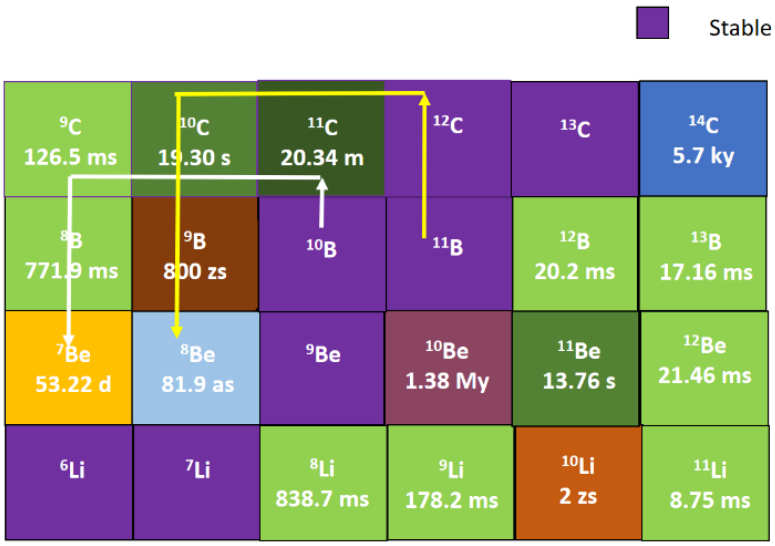


**Figure 1.6**: The relevant portion of the chart of the nuclides is shown to depict the possible production pathways for various shorter-lived radioisotopes in the vicinity of $^{7}Be$, which can be co-produced by proton irradiation of a boron target. This is discussed in greater detail in Chapter 5.

## 1.4 The objective

In preparation for the large-scale isotope harvesting program at FRIB, it is important to establish proof-of-concept procedures and investigate solid-phase harvesting approaches using decommissioned components from the NSCL [41][42]. Collectively, achieving the above-mentioned four AIMs have established guidelines and approaches needed to be able to extract and chemically separate the enormous quantities of long-lived radioisotopes which will

accumulate in several locations along the FRIB beamline during beam delivery to end users (**Figure 1.7**).

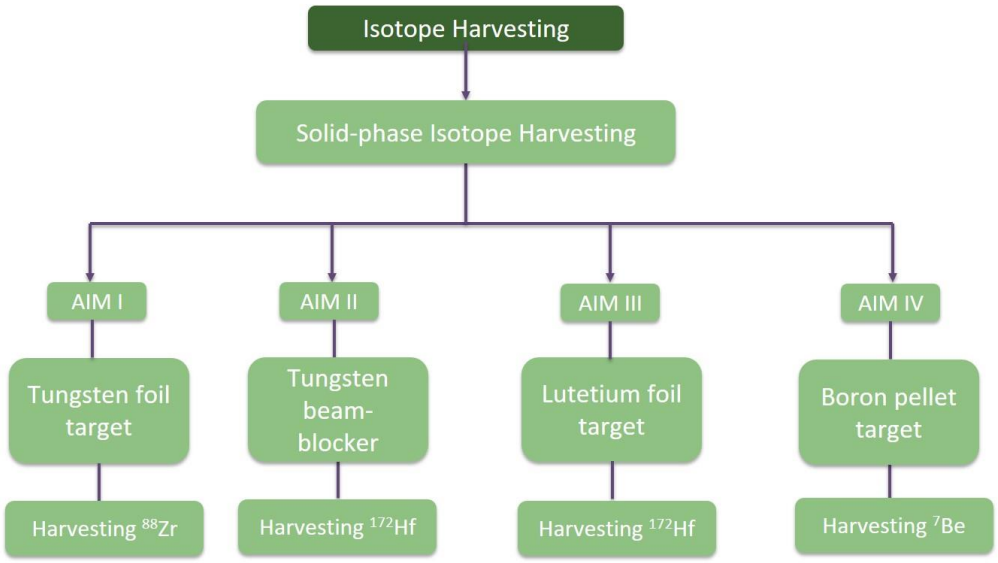


**Figure 1.7:** The schematic of solid-phase isotope harvesting under the broad umbrella of isotope harvesting is shown here, comprising of four AIM's. The first aim involves the harvesting of $^{88}$Zr from a tungsten foil target as a proof of concept experiment, the second aim is to harvest $^{172}$Hf from the tungsten 'heavy-met' beam-blocker, the third aim is to harvest $^{172}$Hf from lutetium foil target, and the fourth aim is to harvest $^{7}$Be from boron pellet target.

## REFERENCES


[1] E. P. Abel *et al.*, 'Isotope harvesting at FRIB: Additional opportunities for scientific discovery', *Journal of Physics G: Nuclear and Particle Physics*, vol. 46, no. 10, 2019, doi: 10.1088/1361-6471/ab26cc.

[2] A. Gade and B. M. Sherrill, 'NSCL and FRIB at Michigan State University: Nuclear science at the limits of stability', *Physica Scripta*, vol. 91, no. 5. Institute of Physics Publishing, Apr. 13, 2016. doi: 10.1088/0031-8949/91/5/053003.

[3] A. B. Balantekin *et al.*, 'Nuclear theory and science of the facility for rare isotope beams', *Modern Physics Letters A*, vol. 29, no. 11. World Scientific Publishing Co. Pte Ltd, Apr. 10, 2014. doi: 10.1142/S0217732314300109.

[4] A. Pen *et al.*, 'Design and construction of a water target system for harvesting radioisotopes at the National Superconducting Cyclotron Laboratory', *Nucl Instrum Methods Phys Res A*, vol. 747, pp. 62–68, 2014, doi: 10.1016/j.nima.2014.02.010.

[5] 'FRIB creates five new isotopes'. Accessed: Mar. 22, 2024. [Online]. Available: https://frib.msu.edu/news/2024/new-isotopes

[6] D. Schumann, E. Maugeri, and R. Dressler, 'Exotic radionuclides - What are they good for?', *Chimia (Aarau)*, vol. 74, no. 12, pp. 932–938, 2020, doi: 10.2533/CHIMIA.2020.932.

[7] D. Schumann and J. Neuhausen, 'Accelerator waste as a source for exotic radionuclides', *Journal of Physics G: Nuclear and Particle Physics*, vol. 35, no. 1, 2008, doi: 10.1088/0954-3899/35/1/014046.

[8] E. P. Abel and G. W. Severin, 'Isotope Harvesting of Aqueous Phase Ions from Heavy-Ion Fragmentation Facilities for the Production of a 47Ca/47Sc Generator', United States -- Michigan, 2020. [Online]. Available: https://ezproxy.msu.edu/login?url=https://www.proquest.com/dissertations-theses/isotope-harvesting-aqueous-phase-ions-heavy-ion/docview/2476547502/se-2?accountid=12598

[9] H. K. Clause and G. W. Severin, 'Demonstrating Gas-Phase Harvesting Capabilities at the NSCL Through the Production and Collection of 76Kr and 77Kr', United States -- Michigan, 2021. [Online]. Available: https://ezproxy.msu.edu/login?url=https://www.proquest.com/dissertations-theses/demonstrating-gas-phase-harvesting-capabilities/docview/2572564689/se-2?accountid=12598

[10] W. Mittig, 'Possible evolutions of rare isotope production methods and the associated instrumentation', *Nucl Instrum Methods Phys Res B*, vol. 317, no. PART B, pp. 186–193, 2013, doi: 10.1016/j.nimb.2013.07.026.

[11] E. P. Abel *et al.*, 'Production, collection, and purification of 47Ca for the generation of 47Sc through isotope harvesting at the national superconducting cyclotron laboratory', *ACS Omega*, vol. 5, no. 43, pp. 27864–27872, 2020, doi: 10.1021/acsomega.0c03020.

[12] T. Mastren *et al.*, ‘Feasibility of isotope harvesting at a projectile fragmentation facility: 67Cu’, *Sci Rep*, vol. 4, pp. 1–6, 2014, doi: 10.1038/srep06706.

[13] T. Mastren *et al.*, ‘Harvesting 67Cu from the Collection of a Secondary Beam Cocktail at the National Superconducting Cyclotron Laboratory’, *Anal Chem*, vol. 87, no. 20, pp. 10323–10329, 2015, doi: 10.1021/acs.analchem.5b02322.

[14] C. S. Loveless *et al.*, ‘Harvesting 48V at the National Superconducting Cyclotron Laboratory’, *Applied Radiation and Isotopes*, vol. 157, no. November 2019, p. 109023, 2020, doi: 10.1016/j.apradiso.2019.109023.

[15] H. K. Clause *et al.*, ‘Harvesting krypton isotopes from the off-gas of an irradiated water target to generate 76Br and 77Br’, *Sci Rep*, vol. 12, no. 1, Dec. 2022, doi: 10.1038/s41598-022-05500-8.

[16] R. Dressler *et al.*, ‘44Ti, 26Al and 53Mn samples for nuclear astrophysics: The needs, the possibilities and the sources’, *Journal of Physics G: Nuclear and Particle Physics*, vol. 39, no. 10, 2012, doi: 10.1088/0954-3899/39/10/105201.

[17] D. Schumann *et al.*, ‘Preparation of a 60Fe target for nuclear astrophysics experiments’, *Nucl Instrum Methods Phys Res A*, vol. 613, no. 3, pp. 347–350, 2010, doi: 10.1016/j.nima.2009.09.072.

[18] M. Ayranov and D. Schumann, ‘Preparation of 26Al, 59Ni, 44Ti, 53Mn and 60Fe from a proton irradiated copper beam dump’, *J Radioanal Nucl Chem*, vol. 286, no. 3, pp. 649–654, 2010, doi: 10.1007/s10967-010-0732-0.

[19] J. Chen, B. Singh, and J. A. Cameron, ‘Nuclear Data Sheets for A = 44’, *Nuclear Data Sheets*, vol. 112, no. 9, pp. 2357–2495, 2011, doi: 10.1016/j.nds.2011.08.005.

[20] M. S. Basunia, ‘Nuclear Data Sheets for A=59’, *Nuclear Data Sheets*, vol. 151, pp. 1–333, 2018, doi: 10.1016/j.nds.2018.08.001.

[21] M. S. Basunia and A. M. Hurst, ‘Nuclear Data Sheets for A = 26’, *Nuclear Data Sheets*, vol. 134, pp. 1–148, 2016, doi: 10.1016/j.nds.2016.04.001.

[22] E. Browne and J. K. Tuli, ‘Nuclear data sheets for A = 60’, *Nuclear Data Sheets*, vol. 114, no. 12, pp. 1849–2022, 2013, doi: 10.1016/j.nds.2013.11.002.

[23] G. Rugel *et al.*, ‘New measurement of the Fe60 half-life’, *Phys Rev Lett*, vol. 103, no. 7, pp. 14–17, 2009, doi: 10.1103/PhysRevLett.103.072502.

[24] A. Wallner *et al.*, ‘Settling the half-life of Fe 60: Fundamental for a versatile astrophysical chronometer’, *Phys Rev Lett*, vol. 114, no. 4, pp. 1–6, 2015, doi: 10.1103/PhysRevLett.114.041101.

[25] D. Schumann, T. Stowasser, R. Dressler, and M. Ayranov, ‘Possibilities of preparation of exotic radionuclide samples at PSI for scientific investigations’, vol. 101, no. 8, pp. 501–508, 2013, doi: doi:10.1524/ract.2013.2058.

[26] S. Heinitz, D. Kiselev, N. Kivel, and D. Schumann, 'Separation of weighable amounts of 10Be from proton irradiated graphite', *Applied Radiation and Isotopes*, vol. 130, pp. 260–263, 2017, doi: https://doi.org/10.1016/j.apradiso.2017.10.012.

[27] A. Visser and N. Scielzo, 'Feasibility of Harvesting Radon from FRIB Beam Dump', *Llnl-Tr-709438*, 2016.

[28] M. Avilov *et al.*, 'Thermal, mechanical and fluid flow aspects of the high power beam dump for FRIB', *Nucl Instrum Methods Phys Res B*, vol. 376, pp. 24–27, 2016, doi: 10.1016/j.nimb.2016.02.068.

[29] K. A. Domnanich, E. P. Abel, H. K. Clause, C. Kalman, W. Walker, and G. W. Severin, 'An isotope harvesting beam blocker for the National Superconducting Cyclotron Laboratory', *Nucl Instrum Methods Phys Res A*, vol. 959, no. January, p. 163526, 2020, doi: 10.1016/j.nima.2020.163526.

[30] E. P. Abel *et al.*, 'Durability test of a flowing-water target for isotope harvesting', *Nucl Instrum Methods Phys Res B*, vol. 478, no. May, pp. 34–45, 2020, doi: 10.1016/j.nimb.2020.05.011.

[31] J. A. Shusterman *et al.*, 'Aqueous harvesting of Zr 88 at a radioactive-ion-beam facility for cross-section measurements', *Phys Rev C*, vol. 103, no. 2, pp. 1–12, 2021, doi: 10.1103/PhysRevC.103.024614.

[32] T. Kobayashi, T. Sasaki, I. Takagi, and H. Moriyama, 'Solubility of zirconium(IV) hydrous oxides', *J Nucl Sci Technol*, vol. 44, no. 1, pp. 90–94, 2007, doi: 10.1080/18811248.2007.9711260.

[33] E. A. McCutchan and A. A. Sonzogni, 'Nuclear Data Sheets for A = 88', *Nuclear Data Sheets*, vol. 115, no. 1, pp. 135–304, 2014, doi: 10.1016/j.nds.2013.12.002.

[34] R. D. Hoffman, K. Kelley, F. S. Dietrich, R. Bauer, and M. Mustafa, 'Modeled Neutron and Charged-Particle Induced Nuclear Reaction Cross Sections for Radiochemistry in the Region of Yttrium, Zirconium, Niobium, and Molybdenum', *Ucrl-Tr-222275*, p. UCRL-TR-222275, 2006.

[35] V. Reis, R. Hanrahan, and K. Levedahl, 'The big science of stockpile stewardship', *AIP Conf Proc*, vol. 1898, no. November 2017, 2017, doi: 10.1063/1.5009218.

[36] J. A. Shusterman *et al.*, 'The surprisingly large neutron capture cross-section of 88Zr', *Nature*, vol. 565, no. 7739, pp. 328–330, 2019, doi: 10.1038/s41586-018-0838-z.

[37] A. C. Larsen *et al.*, 'Experimentally constrained (p,γ) y 89 and (n,γ) y 89 reaction rates relevant to p -process nucleosynthesis', *Phys Rev C*, vol. 93, no. 4, pp. 1–13, 2016, doi: 10.1103/PhysRevC.93.045810.

[38] G. F. Steyn *et al.*, 'Large-scale production of 88Y and 88Zr/88Y generators: A proof of concept study for a 70 MeV H− cyclotron', *Applied Radiation and Isotopes*, vol. 168, no. June 2020, 2021, doi: 10.1016/j.apradiso.2020.109469.

[39] B. Singh, ‘Nuclear Data Sheets for A=172’, *Nuclear Data Sheets*, vol. 75, no. 2, pp. 199–376, 1995, doi: https://doi.org/10.1006/ndsh.1995.1025.

[40] V. S. Shirley, ‘Nuclear Data Sheets for A = 173’, *Nuclear Data Sheets*, vol. 75, no. 2, pp. 377–488, 1995, doi: https://doi.org/10.1006/ndsh.1995.1026.

[41] S. Satija *et al.*, ‘Harvesting 88Zr from heavy-ion beam irradiated tungsten at the National Superconducting Cyclotron Laboratory’, *Applied Radiation and Isotopes*, vol. 197, p. 110831, 2023, doi: https://doi.org/10.1016/j.apradiso.2023.110831.

[42] J. A. Bence *et al.*, ‘Solid-phase isotope harvesting of 88Zr from a radioactive ion beam facility’, *Applied Radiation and Isotopes*, vol. 189, no. August, p. 110414, 2022, doi: 10.1016/j.apradiso.2022.110414.

[43] ‘National Nuclear Data Center’. Accessed: Mar. 22, 2024. [Online]. Available: https://www.nndc.bnl.gov/nudat3/

# CHAPTER 2: $^{88}$Zr HARVESTING: PROOF OF CONCEPT STUDY[1]

This work was the first in the series to demonstrate proof-of-concept for establishing solid-phase isotope harvesting where extraction of radioisotopes from solid tungsten is explored. Tungsten is a widely used material in numerous radioactive ion-beam facilities, where it often undergoes activation through interactions with the beam. The resulting activated products have many potential applications in both basic and applied sciences, provided they can be efficiently recovered with high extraction efficiency. To explore the radiochemistry and harvest Group (IV) elements, an experiment was conducted at NSCL, embedding a heavy-ion $^{88}$Zr beam into a stack of tungsten foils. A method was then developed to separate and recover $^{88}$Zr. This involved dissolving the tungsten foils in 30% $H_2O_2$ and chemically purifying the $^{88}$Zr from the tungsten matrix and other co-implanted radionuclides like $^{85}$Sr and $^{88}$Y. The purification process utilized strong cation-exchange chromatographic resin (AG MP-50) in $H_2SO_4$ media. The resulting $^{88}$Zr was obtained in approximately 60 mL of 0.5 M $H_2SO_4$ with no detectable radio-impurities, achieving an overall recovery yield of (92.3 ± 1.2)%. This is then compared to the recovery of (26±2)% from aqueous methods, making solid-phase harvesting a favorable approach for hydrolyzable elements. This experiment contributes to the development of methods for harvesting elements from tungsten and tungsten-alloy parts commonly irradiated in heavy-ion beam facilities like NSCL/FRIB.

## 2.1 Introduction

The $^{92}$Mo primary beam was fragmented, with the resulting secondary beam, specifically tuned to $^{88}$Zr, implanted into various collector materials including copper, aluminum, gold, and

1 This chapter draws heavily from the published paper S. Satija *et al.*, "Harvesting $^{88}$Zr from heavy-ion beam irradiated tungsten at the National Superconducting Cyclotron Laboratory," *Applied Radiation and Isotopes*, vol. 197, p. 110831, 2023, doi: https://doi.org/10.1016/j.apradiso.2023.110831.

tungsten. While the studies focusing on copper, aluminum, and gold collectors have been described in Bence et al., this chapter explains the extraction and collection process of $^{88}$Zr and its daughter $^{88}$Y from the solid tungsten collector [1].

## 2.2 Experimental

### 2.2.1 Materials

Before the irradiation, the tungsten foils (99.95%, 0.05- mm thick, Alfa Aesar) and tantalum foil backing (99.95%, 0.127-mm thick, Alfa Aesar) were cleaned with ethanol (ACS Reagent, 99.5%, Sigma Aldrich). Post-irradiation chemical processing and dissolution of the tungsten foils was performed with the following reagents: sulfuric acid (ACS reagent, 95.0–98.0%, Sigma Aldrich and OmniTrace, 93–98%, EMD Millipore), hydrogen peroxide (29–31%, Sigma Aldrich), and MilliQ water (obtained from the Thermo Scientific MicroPure Ultrapure Water System, 18.2 MΩ cm). TraceCERT® Zirconium ICP Standard (998 ± 3 ppm Zr, in 2% $HNO_3$ and 0.2% HF, Sigma Aldrich), Yttrium ICP Standard (10,000 ppm, in 5% $HNO_3$, GFS Chemicals), and nitric acid (ACS Plus, 15.8 M, Fisher Chemical) were used in methodology development experiments with stable elements.

Column construction using cation-exchange resin - Cation-exchange resin AG MP-50 (100–200 mesh, H+ form, BioRad) was slurry packed in columns and employed for the separations. The column was constructed from rigid polycarbonate tubing (3/8″ OD, 1/4″ ID, McMaster-Carr, PN:9176T1) and chemical-resistant push-to-connect fittings (Straight Reducer, for 3/8″ x 1/4″ Tube OD). Two pieces of glass wool were inserted on each end of the column to hold the resin in place.

Instruments - All the separations were performed with a peristaltic pump (Ismatec® Reglo Peristaltic Pumps with independent channel control operated with pump tubing of 1.65-

mm internal diameter). For the development of the separation method, the identification and quantification of stable tungsten, zirconium, and yttrium was performed with a 5900 Agilent inductively coupled plasma-optical emission spectrometer (ICP-OES) together with the Agilent ICP Expert software. An HPGe Canberra BEGe γ-ray Detector (BE2020) was used to detect and quantify the radionuclides. A second HPGe detector from PHDS Inc. (Fulcrum Compact HPGe Gamma-ray Spectrometer) was used for detection of radionuclides immediately after the irradiation in NSCL. Phosphor imaging of the tungsten foils was done with an Amersham Typhoon™ Biomolecular Imager (GE Healthcare).

### 2.2.2 Experimental setup

#### 2.2.2.1 Solid-phase harvesting apparatus and irradiation of the tungsten target

The solid-phase collection setup comprised a series of tungsten foils arranged in a stack, depicted in **Figure 2.1**. The outer body of this solid-phase collection setup was made from an aluminum-based KF-40 flange, as shown in **Figures 2.2 (a)** and **2.2 (b)**. This KF-40 flange underwent machining to accommodate metal foils within a cavity which was secured by an outer ring and screws as shown in **Figures 2.2 (a)** and **2.2 (b)**. Ten tungsten foils, each measuring 0.05 mm in thickness and weighing between 540 and 570 mg, along with a 0.127-mm tantalum backing foil, were utilized, resulting in a combined foil stack thickness of 0.627 mm. Before assembling together, the tungsten foils and tantalum backing were wiped with ethanol, then stacked sequentially and securely clamped into the collector assembly between the ring clamp and the KF-40 flange. The foils were labeled from 1 to 10, with the lowest numbered foil positioned closest to the ring clamp. The tantalum backing, situated furthest downstream, served to stop any beam that was not stopped by the foils. This collector assembly was subsequently plugged at the end of the beamline, as depicted in **Figure 2.2 (c)**.

At the NSCL, $88Zr^{39+}$ secondary beam was generated through the fragmentation of a 140-MeV/u primary beam of $^{92}Mo$, directed at a beryllium production target with a thickness of 446 mg/cm$^2$ [2]. A mostly unpurified $88Zr^{39+}$ secondary beam was requested to showcase the collection of a diverse array of beam products. Throughout the 8-hour irradiation period targeting the tungsten material, the beam current was monitored continuously. This was accomplished by inserting a Faraday cup positioned immediately upstream of the endstation, resulting in an integrated beam current of $3.90 \times 10^{-8}$ eA on the tungsten target.

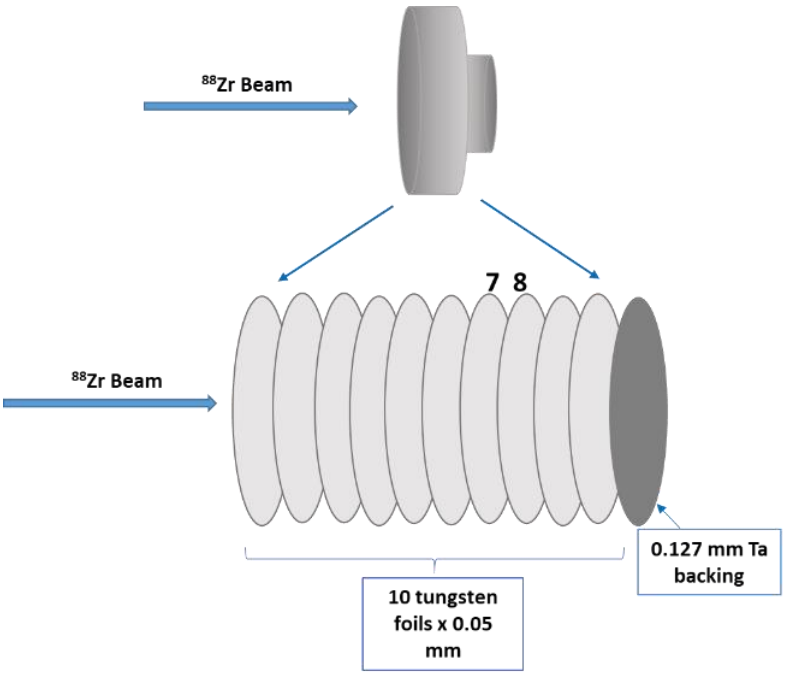


**Figure 2.1**: A schematic of the solid-phase harvesting apparatus used for the irradiation experiment at the NSCL is shown. A thin foil stack of 10 tungsten foils, each 0.05-mm thick, and a 0.127-mm thick tantalum backing foil is housed in the solid collector made of aluminum. Foil 7 and 8 marked here are the most radioactive ones [22].

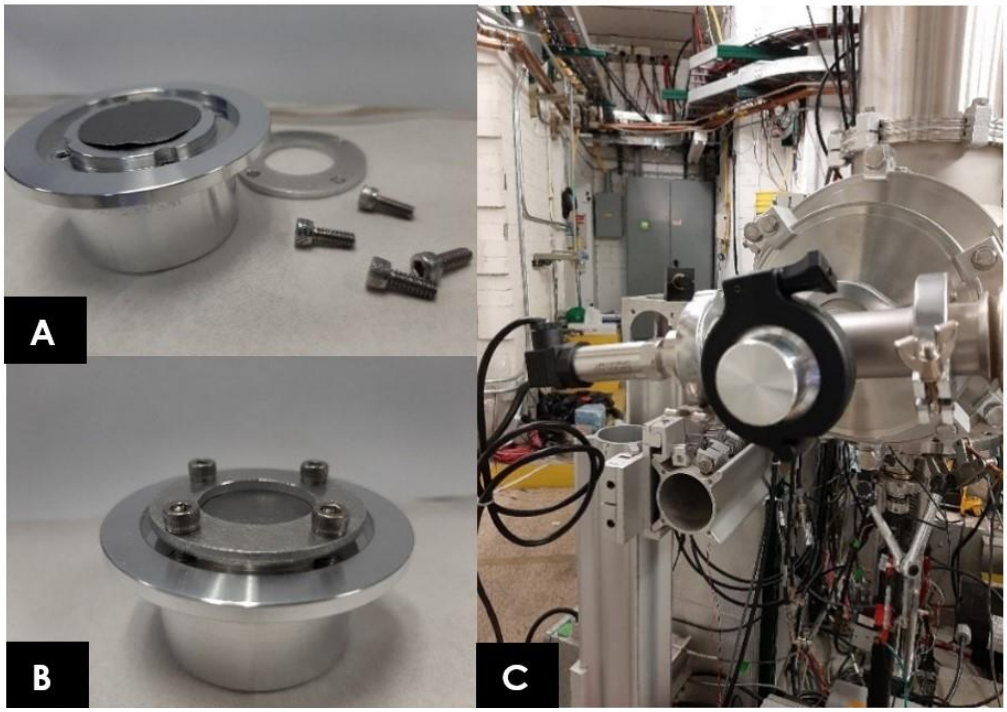


**Figure 2.2:** The disassembled aluminum solid collector apparatus with the ring and screws is shown in (a) and the assembled aluminum solid collector set up containing the clamped tungsten foils and the tantalum backing held by ring and screws is shown in (b). This assembled solid collector body plugged at the end of the S1/S2 user beamline at NSCL is shown in (c) [22].

2.2.2.2 Quantification of radionuclides and comparison with estimated production

Before the irradiation, the LISE++ simulation software was employed to model nuclear reactions at the NSCL and optimize beam parameters with the A1900 fragment separator. This software estimated the radionuclide production rates when fragments interact and get stopped with a solid tungsten matrix. This is illustrated in **Figure 2.3.** These estimated production rates were then used to predict radionuclide activities [3]. Furthermore, LISE++ enabled the determination of range distributions for implanted radionuclides within the tungsten target, which is shown in **Figure 2.3,** where 100% of fragmentation products were expected to stop within the first 440 μm of tungsten. Through this analysis, the main radionuclides identified were $^{88}$Zr, $^{88}$Y, and $^{85}$Sr isotopes.

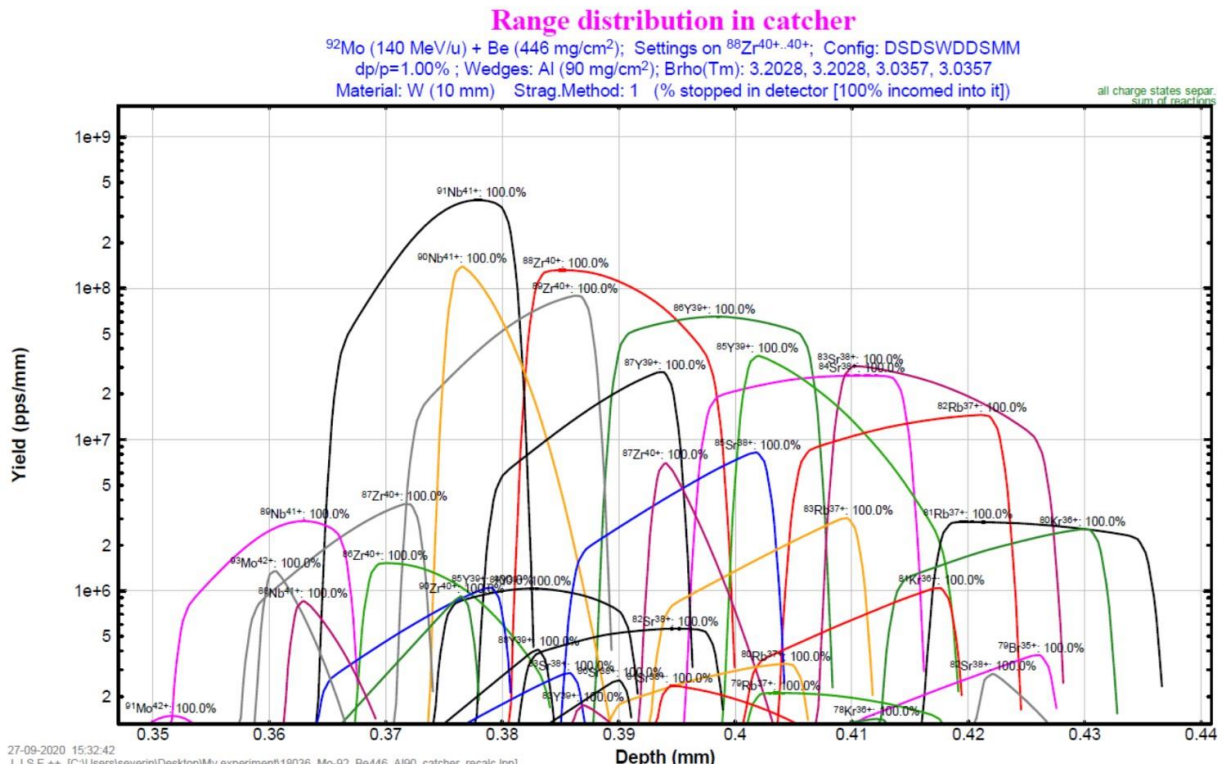


**Figure 2.3**: This range distribution generated from LISE++ for the tungsten catcher illustrates that 100 % of the beam product mixture is expected to stop within the first 0.44 mm of tungsten. Image provided by Dr. Thomas Baumann.

The experimental activities of $^{88}$Zr and $^{88}$Y were determined through γ-ray spectroscopy. At the end of the bombardment (EOB), the solid collector was removed from the NSCL S1/S2 beamline and positioned 50 cm in front of the PHDS HPGe detector, shown in **Figure 2.4**, where it was counted as a complete assembly over varying durations, ranging from approximately 19 minutes to 2.8 hours. To maintain consistent positioning, a ring-stand was employed to elevate the sample as shown in **Figure 2.4**, ensuring the holder remained centered in front of the detector. Immediate counting post-bombardment allowed for the identification of short-lived radionuclides.


**Figure 2.4**: The solid collector housing irradiated tungsten foils counted as a whole in front of the PHDS HPGe detector outside the S1/S2 vault in NSCL to assess the short-lived species.

Following transportation to the MSU Chemistry laboratory, the solid collector underwent disassembly after being counted on the HPGe γ-ray detector as a whole. Each foil was then individually counted to evaluate the radionuclide inventory using the HPGe γ-ray detector. All the calibrations of energy and efficiency for fractions obtained from resin-based separations described in section 2.2.4.2 was conducted using a $^{152}$Eu source (1 μCi, Eckert & Ziegler Analytics), evenly distributed in 10 mL of epoxy within a sealed 15 mL falcon tube positioned at distances of 15 cm and 25 cm from the detector face. To ensure uniform geometry with the calibration setup made for the HPGe detector, all resulting fractions from separations in this study were collected and measured in 15 mL falcon tubes, filled up to 10 mL, and placed in a fixed acrylic holder at the specified distances of 15 and 25 cm.

The analysis of energy spectra was performed using the Genie 2000 software (Mirion Technologies), which identified the characteristic γ-ray emissions of the radionuclides, conducted the background subtraction, and computed the activities based on the net photopeak areas. Throughout all the measurements, the average dead time remained below 3%. Additionally, other long-lived, co-implanted radionuclides, such as $^{85}$Sr, were identified and quantified when observable above the limit of detection. The details of the characteristic γ-ray

emissions and intensities can be found in **Table 2.1**. A comparison was then drawn between the determined activities from gamma spectroscopic measurements and the numbers obtained from the LISE++ models previously mentioned.

2.2.3 Post-irradiation techniques and chemical processing of irradiated tungsten foils

Autoradiography was carried out for the examination of the distribution profile of the radioactive species within the tungsten foils. The assembled tungsten collector along with individual active foils were exposed to a film measuring 20 × 40 $cm^2$ (BAS-IP SR, 2040; GE Healthcare) for durations ranging from 10 to 60 seconds. The Image acquisition was performed using the Amersham Typhoon™ software (version 1.1.0.7, GE Healthcare), while ImageQuant TL (version 8.2.0.0, GE Healthcare) was used for image analysis. The autoradiograph of the

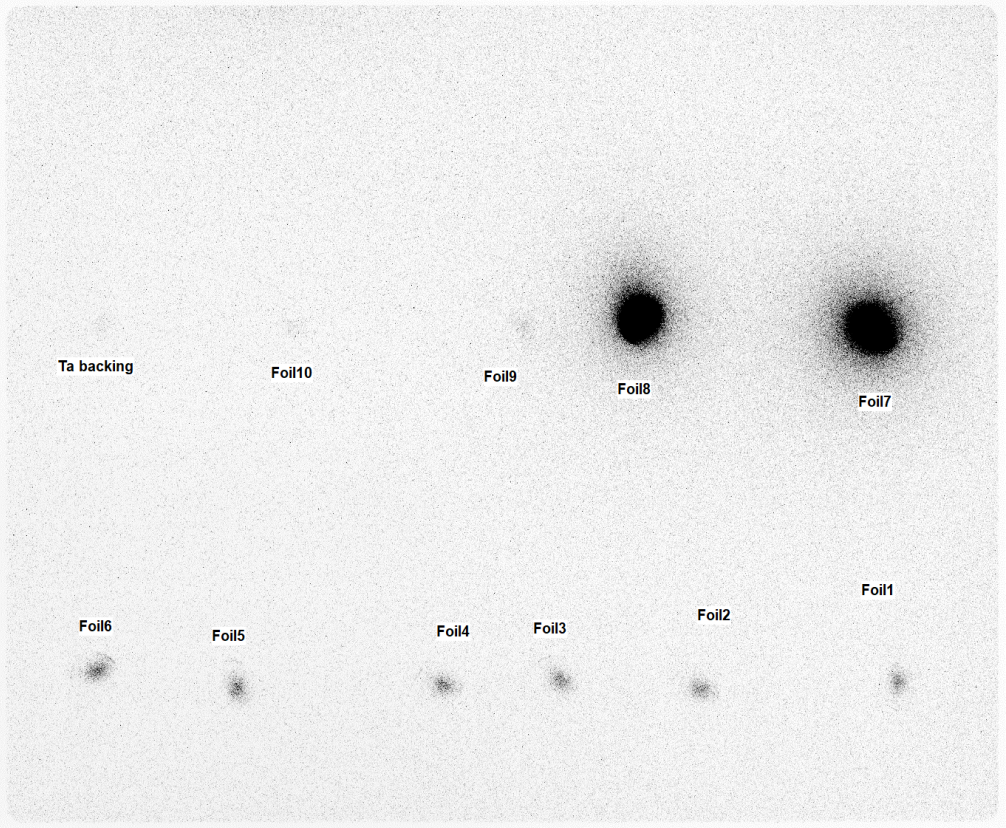


**Figure 2.5**: Autoradiograph generated from the individual tungsten foils numbered 1 through 10 and the tantalum backing where Foil 7 and 8 are the most radioactive.

individual foils numbered 1 through 10 and the tantalum backing foil is shown in **Figure 2.5**. By utilizing this technique, the most radioactive foils i.e., Foil 7 and 8 were identified, and were required to be chemically processed.

Table 2.1: This shows the short- and the long-lived radionuclides present in the secondary beam and their associated gamma-ray emissions used for identification [4].

| **Radionuclide** | **Half-life** | **Gamma-ray Energy [keV] (Intensity)** |
|---|---|---|
| $^{81}$Sr | 22.3 min | 147.76 (30), 153.54 (34), 188.27 (15.4), 443.34 (17.5) |
| $^{82}$Sr | 25.34 days | None |
| $^{83}$Sr | 32.41 hours | 762.65 (26.7) |
| $^{85}$Sr | 64.85 days | 514.0048 (96) |
| $^{83}$Rb | 86.2 days | 520.3991 (45), 529.5945 (29.3), 552.5512 (16) |
| $^{84}$Rb | 32.82 days | 881.6041 (68.9) |
| $^{83}$Y | 7.08 min | 489.9 (5.4), 882.1 (6.2) |
| $^{84}$Y | 39.5 min | 793.1 (98.3), 974.3 (78), 1039.7 (56) |
| $^{85}$Y | 2.68 hours | 231.65 (84), 504.44 (60) |
| $^{86m}$Y | 47.4 min | None |
| $^{86}$Y | 14.74 hours | 627.72 (32.6), 777.37 (22.4), 1076.63 (82.5), 1153.05 (30.5), 1920.72 (20.8) |
| $^{87m}$Y | 13.37 hours | None |
| $^{87}$Y | 79.8 hours | 388.5276 (82.2), 484.805 (89.8) |
| $^{88}$Y | 106.63 d | 898.042 (93.7), 1836.063 (99.2) |
| $^{86}$Zr | 16.5 hours | 242.8 (95.84) |
| $^{87}$Zr | 1.68 hours | 1227 (2.8) |
| $^{88}$Zr | 83.4 d | 392.87 (97.3) |
| $^{89}$Zr | 78.41 h | 909.15 (99.04) |
| $^{88}$Nb | 14.55 min | 271.8 (30.1), 399.4 (31.8), 502.9 (60), 671.2 (64), 1057.1 (100) |
| $^{89}$Nb | 2.03 hours | 1627.2 (3.5) |
| $^{90}$Nb | 14.6 h | 141.178 (66.8), 1129.224 (92.7), 2318.959 (82.0) |
| $^{91}$Nb | 680 years | None |
| $^{90}$Mo | 5.56 hours | 257.34 (77) |
| $^{93}$Mo | 4000 years | None |

### 2.2.4 Separation chemistry development

#### 2.2.4.1 Separation chemistry development with stable elements

Establishing chemistry techniques with stable tracers is an important prerequisite before attempting radiochemical separations. In order to establish a procedure for separating $^{88}$Zr and $^{88}$Y from the tungsten matrix, solutions of stable Zr and Y in a $H_2SO_4$ medium were prepared by using the ICP-OES standards. Subsequently, these solutions were separated from 18-500 mg of stable dissolved tungsten foil in 30% $H_2O_2$. The separation process involved employing the cation exchange chromatographic resins, specifically DOWEX 50W-X8 and AG MP-50. The separation was carried out using a peristaltic pump, following the calibration of the flow rate, and, fractions of 10-14 mL were collected.

To assess the efficacy of the separation, aliquots were withdrawn from each fraction and appropriate dilutions in 0.6% tartaric acid + 2% $HNO_3$ were made for subsequent analysis via ICP-OES. Calibration curves for sample analysis were established by diluting standards to 0.01 - 50 ppm. The separation efficiency was quantified by expressing the total eluted amount in all fractions as a percentage of the loaded amount for each element.

#### 2.2.4.2 Separation with active foils 7 and 8

Post autoradiography, a waiting period of 10 weeks was observed to allow for the decay of shorter-lived isotopes such as $^{90}$Nb ($t_{1/2}$ = 14.6 hours), $^{83}$Sr ($t_{1/2}$ = 32.4 hours), $^{85}$Y ($t_{1/2}$ = 2.7 hours), $^{86}$Y ($t_{1/2}$ = 14.7 hours), $^{87}$Y ($t_{1/2}$ = 79.8 hours), and $^{89}$Zr ($t_{1/2}$ = 78.4 hours) [4]. A schematic is shown in **Figure 2.6** which is a snippet of the chart of the nuclides of the radionuclides embedded. Before chemically processing, approximately 1 mm of the inactive circular edges of both foil 7 and foil 8 were cut to reduce the excess tungsten mass.

A total of three separations were carried out, one with foil 7 and two with foil 8 and the results were compared. The active tungsten foils 7 and 8 were dissolved in 8.3 mL and 8.5 mL of 30% hydrogen peroxide, respectively. To ensure complete dissolution, these solutions were heated at approximately 60°C for a duration of 8 hours. Upon dissolution, volumes of 1.9 mL and 2.0 mL were withdrawn from the solutions corresponding to a mass of approximately 100 mg tungsten each. These aliquots were subsequently adjusted to achieve a concentration of ≤0.2 M $H_2O_2$ and 0.1 M $H_2SO_4$ through the addition of dilute sulfuric acid. The resulting loading solutions, with volumes of 93 mL and 98 mL, respectively, were used for the subsequent radiochemical separations.

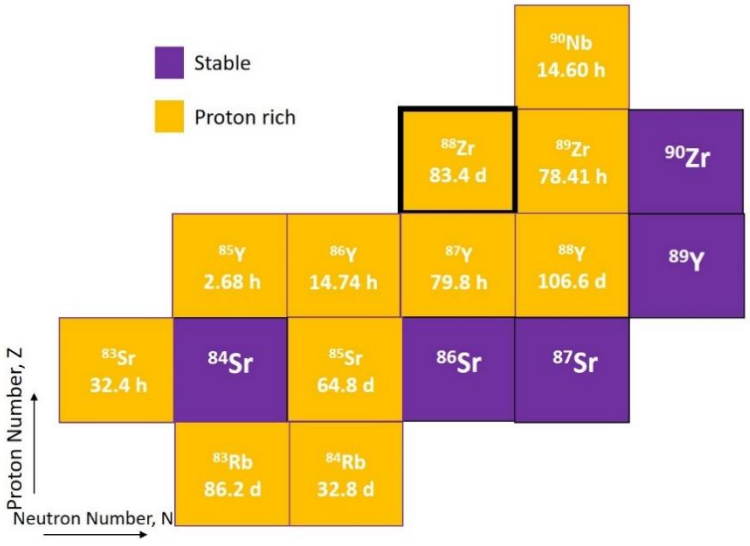


**Figure 2.6**: Schematic of the radionuclides generated when the secondary $^{88}$Zr beam is embedded in the tungsten collector.

Three columns slurry packed with AG MP-50 resin (9 mm outer diameter, 6 mm inner diameter, and 15–18 cm in length) were prepared for use. Rinsing was done sequentially with 30 mL of MilliQ water, 24 mL of 2 M $H_2SO_4$, and finally conditioned with 24 mL of a mixture comprising 0.2 M $H_2O_2$ + 0.1 M $H_2SO_4$. Subsequently, the prepared loading solutions were passed over these pre-conditioned columns. The majority of tungsten present in the loading

solution passed through the columns and was collected in 10 mL fractions. To ensure a thorough removal of any remaining tungsten, a rinse step was performed using 28–30 mL of 0.1 M $H_2SO_4$.

In the next step, $^{88}$Zr was eluted by passing 60–70 mL of 0.5 M $H_2SO_4$ through the columns. This was followed by the elution of $^{88}$Y, $^{85}$Sr, and any residual $^{88}$Zr using 30 mL of 6 M $H_2SO_4$. The flow rate was maintained at a constant 0.8 mL/min throughout the process of conditioning and separation.

2.2.5. Stable element analysis

The load and rinse fractions obtained from the radiochemical separations were analyzed using ICP-OES to determine the concentration of tungsten. Each fraction was used for preparing two different dilutions of the same concentration, by extracting an aliquot and diluting in a solution containing 0.6% tartaric acid + 2% $HNO_3$. The quantification and analysis were performed using Agilent ICP software.

For the analysis, the emission lines with the highest intensity for tungsten (207.912, 209.475, 220.449, 224.876, 203.000 nm), zirconium (343.823, 327.307, 349.619, 327.927, 339.198 nm), and yttrium (371.029, 360.074, 377.433, 361.104, 378.869 nm) were selected. The ICP-OES analysis was conducted under conditions of axial plasma view, with a plasma gas flow rate of 12 L/min, auxiliary gas flow of 1.0 L/min, nebulizer gas flow of 0.7 L/min, and make-up flow of 0.00 L/min.

**2.3 Results and discussion**

2.3.1. Radionuclide identification and quantification

As observed from **Figure 2.3**, The LISE++ simulation indicated that the majority of beam particles were expected to penetrate and stop in a depth ranging from 0.34 to 0.44 mm within the tungsten foil [3]. This is supported by the observation that foil 7 (0.30–0.35 mm) and

foil 8 (0.35–0.40 mm) showed the highest levels of activation following irradiation, as confirmed by subsequent post-irradiation γ-spectroscopy (**Figure 2.8**) and autoradiography measurements (**Figure 2.5**).

The beam current measurements showed that, on average, $(1.59 \pm 0.01) \times 10^7$ particles per second per particle nano-Ampere of $^{92}$Mo primary beam (pps/pnA) of $^{88}Zr^{39+}$ impinged on the tungsten foils. Further details regarding beam tuning can be found in Bence et al. [1]. Consequently, a total of $4.42 \times 10^{11}$ atoms of $^{88}$Zr were accumulated on the tungsten foils by the end of bombardment, which spanned a duration of 7.70 hours.

Through gamma spectroscopic measurements post irradiation, no activity was detected on the collector body, tantalum backing, or the screws, while the ring exhibited minimal activity, indicating the beam was well centered on the target. The evaluation of all the foils started 92 hours post-irradiation, and an HPGe spectrum of the non-active foil 3 and active foil 7 is depicted in **Figure 2.7** and **Figure 2.8**, respectively.

The radionuclides $^{88}$Y and $^{85}$Sr, as the radioactive daughters of $^{88}$Zr and $^{85}$Y, respectively, were detected in foil 8, given the short half-life of $^{85}$Y ($t_{1/2}$ = 2.68 hours) at the time of measurement [5]. By the time of radiochemical separations, conducted 10 weeks after EOB, the short-lived $^{87}$Zr ($t_{1/2}$ = 1.68 hours) and $^{89}$Zr ($t_{1/2}$ = 78.4 hours) had already decayed, leaving $^{88}$Zr as the sole radioactive zirconium isotope [6], [7].

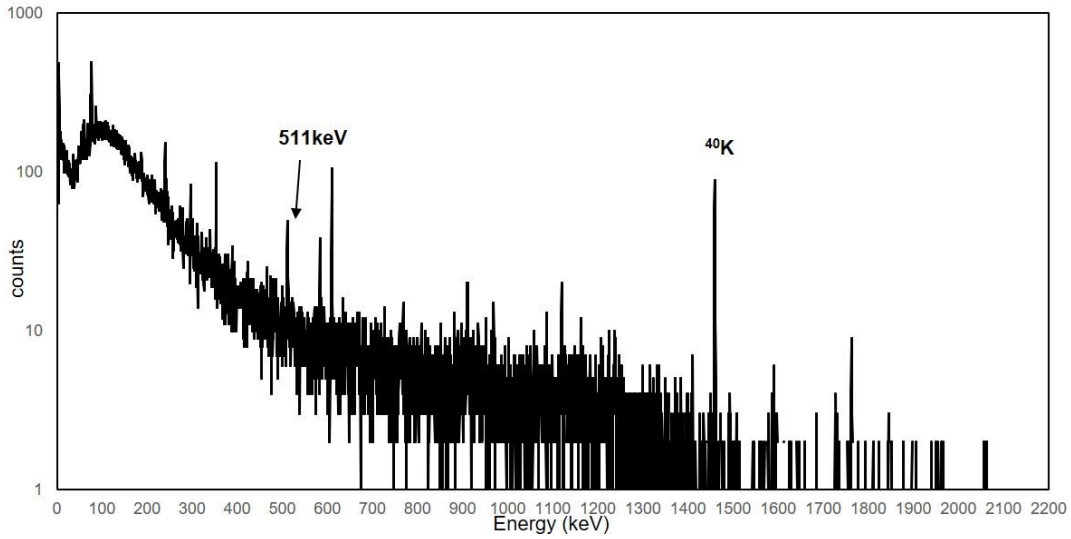


**Figure 2.7**: Gamma spectrum for the non-active foil 3 indicating the absence of $^{88}$Zr and peaks for other radionuclides.

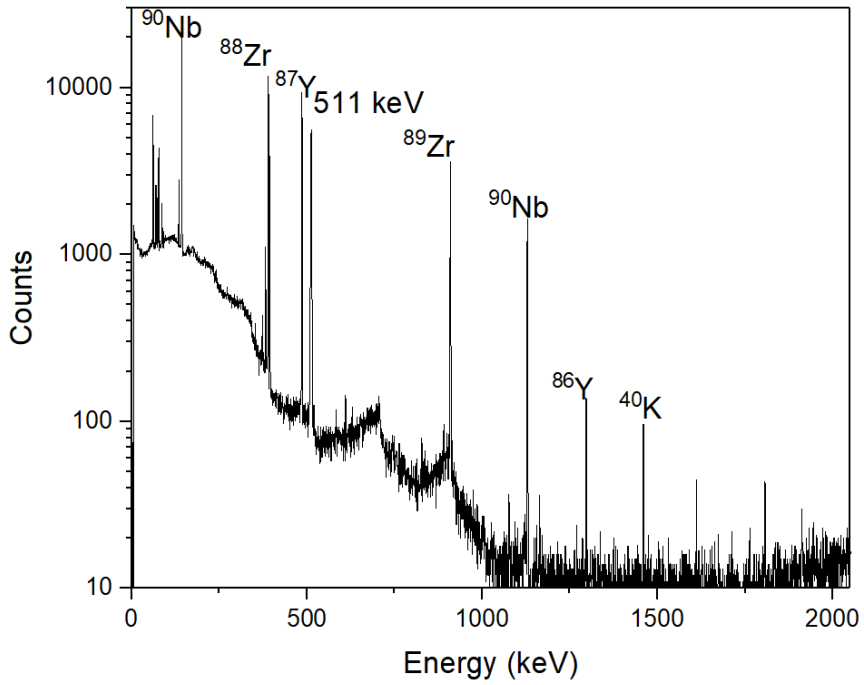


**Figure 2.8**: Gamma spectrum of the active foil 7. HPGe spectrum of foil 7 recorded 92 h after EOB. The co-implanted radionuclides include $^{88}$Zr, $^{89}$Zr, $^{86}$Y, $^{87}$Y, and $^{90}$Nb. The remaining peaks are those from the background [22].

Based on gamma spectroscopic measurements, the cumulative activity of $^{88}$Zr measured in tungsten foils 7 and 8 (decay corrected to EOB) was determined to be 42.55 ± 0.37 kBq,

aligning within 1σ agreement with the theoretically predicted yield of 42.51 kBq for $^{88}$Zr.

2.3.2. Post-irradiation techniques and chemical processing of irradiated foils

2.3.2.1 Separation chemistry

Tungsten foils are typically dissolved using either hydrofluoric acid or concentrated peroxide, as noted in prior studies [8], [9], [10], [11]. In this study, hydrogen peroxide was selected over hydrofluoric acid to prevent fluoride ion-related effects and the creation of zirconium fluoride complexes. The irradiated tungsten completely dissolved in the hydrogen peroxide solution without any visible precipitation. Additionally, previous literature describes several methods utilizing acidic hydrogen peroxide solutions for cation exchange-based separations to elute tungsten as an anionic peroxy complex, thereby preventing W(VI) hydrolysis [8], [12], [13].

Hence, this separation is based on the inability of the prevalent anionic peroxy complex of tungsten to retain on cation exchange resin under dilute sulfuric acid conditions. Sulfuric acid was selected due to the enhanced stability of W(VI) in $H_2SO_4$ compared to HCl or $HNO_3$. Given that the foils underwent heating in 30% $H_2O_2$ for approximately 8 hours, peroxide decomposition and consumption were inevitable, thereby establishing 0.2 M $H_2O_2$ as the 'upper limit' for achievable peroxide concentration. Employing the previously outlined elution conditions, tungsten was quantitatively eluted with high radiopurity.

Table 2.2: $K_d$ values in $H_2SO_4$ with a sulfonated polystyrene resin for Zr(IV) and Y(III) [14].

| | **0.05 M $H_2SO_4$** | **0.1 M** | **0.25 M** | **0.5 M** | **1.0 M** | **1.5 M** |
|---|---|---|---|---|---|---|
| **Zr (IV)** | 546 | 474 | 98 | 4.6 | 1.4 | 1.2 |
| **Y(III)** | $>10^4$ | $>10^4$ | 1380 | 253 | 49.9 | 18.0 |

At low acidity, such as 0.1 M $H_2SO_4$, the cationic $Zr(IV)SO_4^{2+}$complex is adsorbed to cationic resin, as shown from distribution coefficient ($K_d$) values in **Table 2.2**. [15]. The elution

of Zr becomes possible when the molarity is increased to 0.5 M $H_2SO_4$, which promotes the formation of anionic Zr species $Zr(SO_4)_3^{2-}$ and $Zr(SO_4)_4^{4-}$ with poor affinity towards the cationic resin [15]. Additionally, with 0.5 M $H_2SO_4$, the distribution coefficients of Y(III) and Sr(II) are still high compared to Zr(IV), thus allowing the elution of pure zirconium [14].

The gamma spectrum analysis of the $^{88}$Zr fraction, conducted immediately after the separation of foil 8 (shown in **Figure 2.10**), showed no gamma-ray peaks attributable to $^{88}$Y or $^{85}$Sr. The retrieval of $^{88}$Zr amounted to (94.2 ± 1.4)% of the loading solution for foil 7 and (91.3 ± 1.1)% for foil 8, across a volume range of 55–58 mL, without any detectable $^{88}$Y or $^{85}$Sr peaks. This represents a significant increase in $^{88}$Zr recovery compared to the aqueous harvesting results of (26 ± 2)% discussed earlier [16]. In subsequent fractions eluted using 6 M $H_2SO_4$, the recovery of $^{88}$Y averaged (95.8 ± 5.7)% of the loaded solution for both foil 7 and foil 8, within a volume range of 33–37 mL, accompanied by the co-elution of the remaining $^{88}$Zr and the entirety of $^{85}$Sr. It's worth noting that while the yttrium fraction wasn't radiopure, there exists several methods for separating Y from Sr and Zr [17], [18], [19]. One of the methods that was tried but wasn’t successful is detailed below. The separation process utilizing AG MP-50 described in this study is illustrated in **Figure 2.9**, and **Figure 2.11** serves as a representative elution profile for the separation involving foil 7.

To further purify the obtained $^{88}$Y fractions from the first separation step, the $^{85}$Sr-, $^{88}$Zr- and $^{88}$Y-containing mixture in 6 M $H_2SO_4$ was complexed with Oxalic acid and adjusted to yield a final concentration of 0.3 M Oxalic acid + 3 M $H_2SO_4$. This solution was loaded on the DGA-resin containing column. In this case, an average of (107.0 ± 5.6)% $^{88}$Zr eluted for Foil 7 and Foil 8 separation, and an average of (86.6 ± 5.5)% $^{85}$Sr eluted for Foil 8 separation for the load

solution and the 0.3 M Oxalic acid + 3 M $H_2SO_4$ rinse leaving only $^{88}Y$ adsorbed to the DGA column.

However, only (32.6 ± 3.7)% $^{88}Y$ could be recovered with 0.01 M $H_2SO_4$ for Foil 7, while no elution was observed in the case of Foil 8 separations. This irreversible adsorption was observed despite attempts of increasing the $H_2SO_4$ concentration and thereafter changing the medium to HCl. This adsorption behavior of $^{88}Y$ onto the DGA is in contrast to the cold separations, where >80 - 90 % recovery of Y was observed with 0.01 M $H_2SO_4$ and the largest losses in the entire process were due to the irreversible adsorption of $^{88}Y$ to the DGA column. One of the reasons could be the adsorption of $^{88}Y$ to the resin backbone [20]. An average quantitative recovery of (73.0 ± 5.9)% $^{88}Y$ for Foil 7 and 8 was only possible with the addition of pure ethanol, which also eluted the TODGA functional groups from the solid support material. A

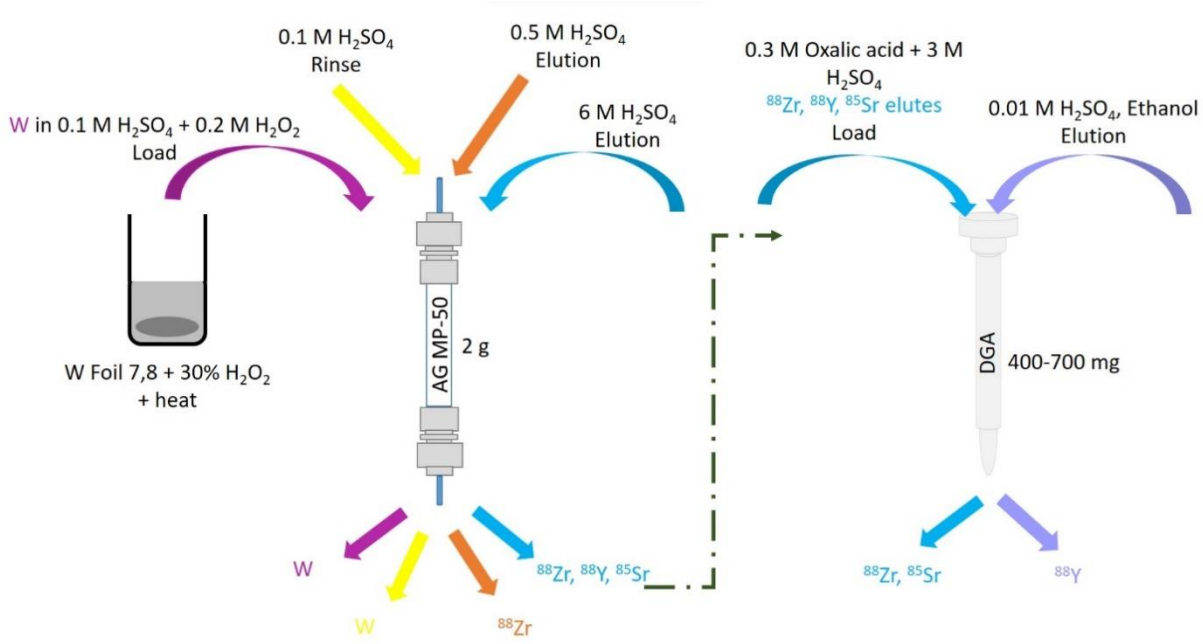


**Figure 2.9**: A schematic of the separation scheme (from left to right) employing the use of AG MP-50 and DGA resin for the recovery of $^{88}Zr$ and $^{88}Y$.

possible suggested extraction of the $^{88}$Y from the eluted TODGA-ethanol mixture could be done by the addition of dodecane, followed by a back-extraction with 0.1 M $HNO_3$ [20], [21].

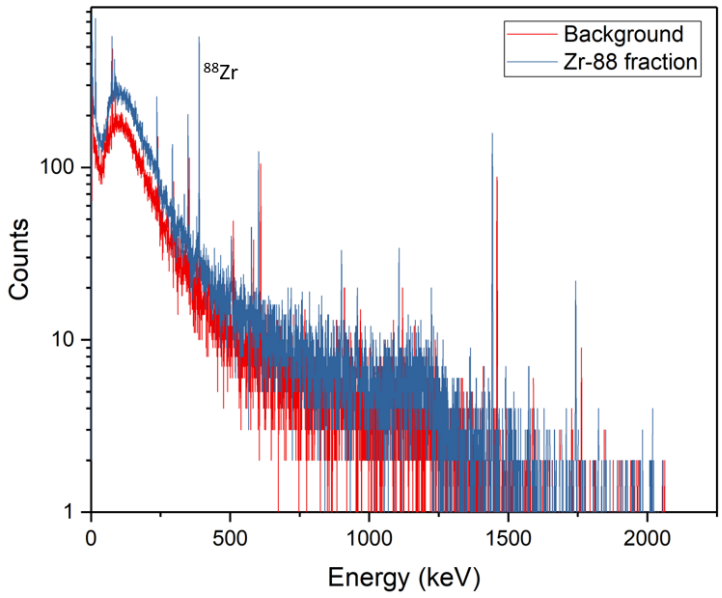


**Figure 2.10**: Gamma spectrum for the purified $^{88}$Zr fraction, directly after elution showing peaks from $^{88}$Zr with no accompanying $^{88}$Y peaks, overlaid with the background spectrum.

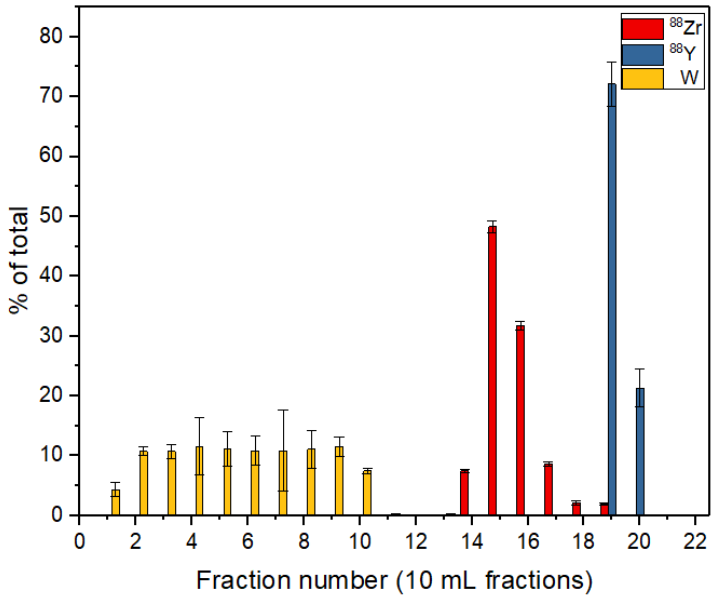


**Figure 2.11**: The elution profile obtained for tungsten foil 7 separation using AG MP-50 resin for the extraction of $^{88}$Zr [22].

## 2.4 Conclusion

This first proof-of-concept study aimed to establish and evaluate radiochemical techniques for separating Zr from a tungsten matrix using radioactive samples. The implanted $^{88}$Zr was successfully isolated from the tungsten matrix utilizing cation-exchange resin. The methodologies developed in this work yielded a recovery rate of (92.3 ± 1.2)% for $^{88}$Zr with high radionuclidic purity, establishing that solid-phase harvesting is a better approach over aqueous-phase methods, which only achieved a recovery rate of (26 ± 2)% of the $^{88}$Zr content [16]. Similar conclusions were drawn from the study of Al, Cu, and Au collectors for solid-phase harvesting [1].

Given the analogous chemistry of Hf to Zr and Lu to Y, it is expected that the solid-phase harvesting techniques developed in this study could be applied to recover Hf and Lu from tungsten-alloy components at NSCL, one of which is the heavy-met alloy beam blocker discussed in the next chapter. This will provide a viable route to obtaining $^{172}$Hf, which can be challenging to produce in high purity through alternative means. Additionally, the solid-phase harvesting system constructed as part of this endeavor can be used for future solid-phase isotope harvesting endeavors at FRIB.

## REFERENCES


[1] J. A. Bence *et al.*, "Solid-phase isotope harvesting of 88Zr from a radioactive ion beam facility," *Applied Radiation and Isotopes*, vol. 189, no. August, p. 110414, 2022, doi: 10.1016/j.apradiso.2022.110414.

[2] D. J. Morrissey, B. M. Sherrill, M. Steiner, A. Stolz, and I. Wiedenhoever, "Commissioning the A1900 projectile fragment separator," *Nucl Instrum Methods Phys Res B*, vol. 204, pp. 90–96, 2003, doi: 10.1016/S0168-583X(02)01895-5.

[3] O. B. Tarasov and D. Bazin, "LISE++: Radioactive beam production with in-flight separators," *Nucl Instrum Methods Phys Res B*, vol. 266, no. 19–20, pp. 4657–4664, 2008, doi: 10.1016/j.nimb.2008.05.110.

[4] "National Nuclear Data Center." Accessed: Mar. 22, 2024. [Online]. Available: https://www.nndc.bnl.gov/nudat3/

[5] B. Singh and J. Chen, "Nuclear data sheets for A = 85," *Nuclear Data Sheets*, vol. 116, no. 1, pp. 1–162, 2014, doi: 10.1016/j.nds.2014.01.001.

[6] T. D. Johnson and W. D. Kulp, "Nuclear Data Sheets for A = 87," *Nuclear Data Sheets*, vol. 129, pp. 1–190, 2015, doi: 10.1016/j.nds.2015.09.001.

[7] B. Singh, "Nuclear Data Sheets for A = 89," *Nuclear Data Sheets*, vol. 114, no. 1, pp. 1–208, 2013, doi: 10.1016/j.nds.2013.01.001.

[8] J. S. Fritz and J. J. Topping, "Chromatographic separation of vanadium, tungsten and molybdenum with a liquid anion-exchanger," *Talanta*, vol. 18, no. 9, pp. 865–872, 1971, doi: 10.1016/0039-9140(71)80143-1.

[9] S. U. Ganiev, T. Artykbae, and G. A. Tsyganov, "Kinetics and Dissolution Products of Molybdenum and Tungsten in Hydrogen-Peroxide," *Zhurnal Neorganicheskoi Khimii*, vol. 18, no. 3, pp. 709–711, 1973.

[10] K. Smith and J. R. Dean, "Investigation into the Spontaneous Dissolution of Tungsten Using Acid Media," vol. 118, no. November, pp. 1445–1447, 1993, doi: 10.1039/AN9931801445.

[11] K. N. Kmak, J. D. Despotopulos, and N. D. Scielzo, "Development of Chemical Procedures for Isotope Harvesting: Separation of Trace Hafnium from Tungsten," *Solvent Extraction and Ion Exchange*, vol. 40, no. 7, pp. 718–734, 2022, doi: 10.1080/07366299.2022.2079502.

[12] J. S. Fritz and L. H. Dahmer, "Cation Exchange Separation of Molybdenum, Tungsten, Niobium, and Tantalum from Other Metal Ions," *Anal Chem*, vol. 37, no. 10, pp. 1272–1274, 1965, doi: 10.1021/ac60229a026.

[13] L. H. Dahmer, "Chromatographic separations of niobium , tantalum , molybdenum , and tungsten," 1966.

[14] F. W. E. Strelow, R. Rethemeyer, and C. J. C. Bothma, “Ion Exchange Selectivity Scales for Cations in Nitric Acid and Sulfuric Acid Media with a Sulfonated Polystyrene Resin,” *Anal Chem*, vol. 37, no. 1, pp. 106–111, 1965, doi: 10.1021/ac60220a027.

[15] J. Korkisch, *Handbook of Ion Exchange Resins: Their Application to Inorganic Analytical Chemistry Volume VI*. Boca Raton / London / Tokyo: CRC Press, 2017. doi: 10.1201/9781315140520.

[16] J. A. Shusterman *et al.*, “Aqueous harvesting of Zr 88 at a radioactive-ion-beam facility for cross-section measurements,” *Phys Rev C*, vol. 103, no. 2, pp. 1–12, 2021, doi: 10.1103/PhysRevC.103.024614.

[17] S. A. Kandil, B. Scholten, Z. A. Saleh, A. M. Youssef, S. M. Qaim, and H. H. Coenen, “A comparative study on the separation of radiozirconium via ion-exchange and solvent extraction techniques, with particular reference to the production of 88Zr and 89Zr in proton induced reactions on yttrium,” *J Radioanal Nucl Chem*, vol. 274, no. 1, pp. 45–52, Oct. 2007, doi: 10.1007/s10967-006-6892-2.

[18] M. J. O’Hara, N. J. Murray, J. C. Carter, and S. S. Morrison, “Optimized anion exchange column isolation of zirconium-89 (89Zr) from yttrium cyclotron target: Method development and implementation on an automated fluidic platform,” *J Chromatogr A*, vol. 1545, pp. 48–58, 2018, doi: 10.1016/j.chroma.2018.02.053.

[19] S. Lahiri, B. Mukhopadhyay, and N. R. Das, “Simultaneous production of 89Zr and 90,91m,92mNb in α- particle activated yttrium and their subsequent separation by HDEHP,” *Applied Radiation and Isotopes*, vol. 48, no. 7, pp. 883–886, 1997, doi: 10.1016/S0969-8043(96)00338-7.

[20] Y. Sasaki, Y. Sugo, Y. Kitatsuji, A. Kirishima, T. Kimura, and G. R. Choppin, “Complexation and back extraction of various metals by water-soluble diglycolamide,” *Analytical Sciences*, vol. 23, no. 6, pp. 727–731, 2007, doi: 10.2116/analsci.23.727.

[21] Y. Sasaki, Z. X. Zhu, Y. Sugo, and T. Kimura, “Extraction of various metal ions from nitric acid to n-dodecanen by diglycolamide (DGA) compounds,” *J Nucl Sci Technol*, vol. 44, no. 3, pp. 405–409, 2007, doi: 10.1080/18811248.2007.9711301.

[22] S. Satija *et al.*, “Harvesting 88Zr from heavy-ion beam irradiated tungsten at the National Superconducting Cyclotron Laboratory,” *Applied Radiation and Isotopes*, vol. 197, p. 110831, 2023, doi: https://doi.org/10.1016/j.apradiso.2023.110831.

# CHAPTER 3: $^{172}$Hf HARVESTING FROM TUNGSTEN 'HEAVY-MET' ALLOY BEAM-BLOCKER

Despite their relevance for many applications, the radioisotope $^{172}$Hf and its daughter $^{172}$Lu are not readily available. One way to obtain this is from the decommissioned beam-blocker (described briefly in the Introduction chapter) obtained from NSCL. Generally, amongst all the solid components of an accelerator, a beam dump will accumulate a wide variety of long-lived isotopes and can be potentially challenging to chemically separate as will be seen in this Chapter.

## 3.1 Introduction

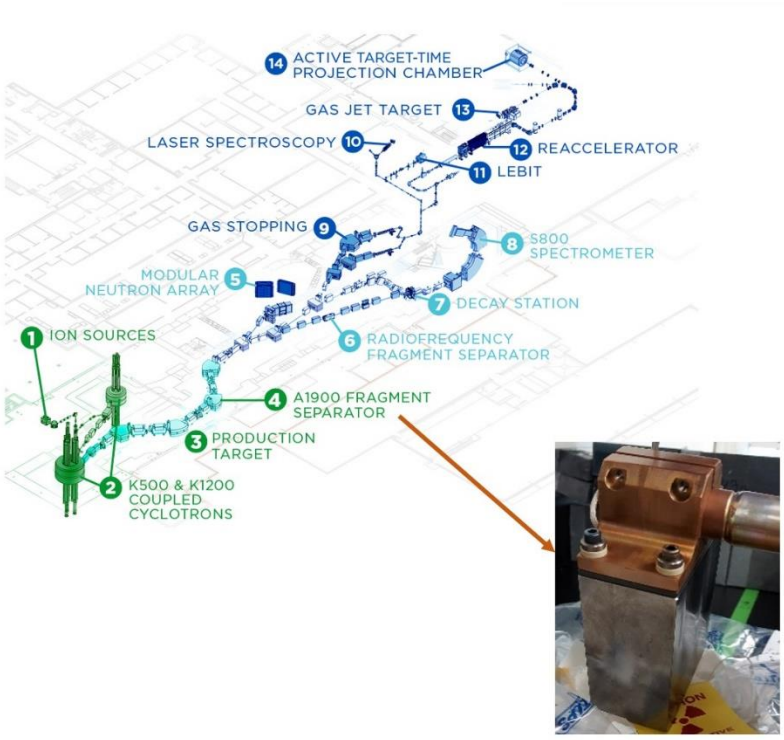


**Figure 3.1**: A schematic depicting the location of the tungsten 'heavy-met' alloy beam-blocker at the decommissioned facility, NSCL, is shown. It was located after the first large dipole magnet of the A1900 separator and was used to intercept the unused primary beam. Here, the beam-blocker is still bound to its fixture, and the beam-spot is also visible on the front side [9].

The beam-blocker had been irradiated over the course of about twenty years and now has substantial quantities of useful radionuclides such as $^{7}$Be, $^{22}$Na, $^{42}$Ar, $^{46}$Sc, $^{54}$Mn, $^{56,57,60}$Co, $^{68}$Ga, $^{68}$Ge, $^{88}$Y, $^{88}$Zr, $^{101,102,102m}$Rh, $^{110m}$Ag, $^{109}$Cd, $^{125}$Sb, $^{133}$Ba, $^{143,144}$Pm, $^{145}$Sm, $^{148,151}$Gd, $^{172,173}$Lu, $^{172,175}$Hf, $^{182}$Ta, $^{184,184m}$Re, and $^{181}$W embedded in it. This list is not exhaustive and reasons are provided in section 3.3. This beam-blocker was later replaced with a water-filled beam blocker for harvesting byproduct radioisotopes in some experiments and its position before being decommissioned is shown in **Figure 3.1**.

Of particular interest in the beam-blocker is $^{172}$Hf ($t_{1/2}$ = 1.87 y, $E_\gamma$ = 125.8 keV ($I_\gamma$ = 11.3%), 23.9 keV ($I_\gamma$ = 20.3%)) which undergoes electron capture and generates $^{172}$Lu ($t_{1/2}$ = 6.7 d, $E_\gamma$ = 1093.6 keV ($I_\gamma$ = 63.0%), 181.5 keV ($I_\gamma$ = 20.6%), 900.7 keV ($I_\gamma$ = 29.8%)) [1]. The half-life of the daughter $^{172}$Lu here is also adequate, lasting weeks of investigation making it suitable for a variety of purposes. Apart from being a radiotracer which could be used for compound labelling and biodistribution studies, $^{172}$Lu also has suitable properties for being a PAC probe due to the 91-1094 keV γγ-cascade in the $^{172}$Yb daughter [2], [3]. This PAC probe finds application in wide Band-Gap Semiconductors [4]. It is also acknowledged that there is a major limitation in availability and production of radioisotopes with appropriate properties for PAC which makes purifying of $^{172}$Lu a worthwhile endeavor [5], [6]. Efforts are also underway to harvest the radiolanthanides and entrapped radioactive gases from the beam-blocker.

In this chapter, a general chemical procedure for recovering $^{172}$Hf from the NSCL/FRIB beam-blocker is described. A significant amount (approximately 500 g) of tungsten alloy was dissolved in hydrogen peroxide in batches (notably without the use of hydrofluoric acid), followed by precipitation-based debulking of tungsten and then purification on LN resin to isolate hafnium. In order to obtain the pure $^{172}$Lu samples necessary for applications, a

$^{172}$Hf/$^{172}$Lu generator system was developed. The generated $^{172}$Lu was used for PAC measurements, and after several milkings, the generator as remade on another LN resin. Decommissioning of the components such as this from NSCL has made it possible to harvest isotopes and opens up numerous possibilities for research and applications. The methods developed here will also have applicability to any future efforts to extract byproducts from the tungsten targets at other facilities (described in detail in Chapter 6).

## 3.2 Experimental

### 3.2.1 Materials

#### 3.2.1.1 Reagents

Before processing the beam-blocker, a tungsten foil (99.95%, 0.05- mm thick, Alfa Aesar), and a scrap piece of heavy-met alloy obtained from NSCL, were used for methodology development.

The dissolution and chemical processing tests for the beam-blocker was performed with the following reagents: hydrogen peroxide (29-31%, Sigma Aldrich), hydrochloric acid (HCl, Optima Grade, 32.0-35.0%, Fisher Chemical and 99.99% Trace metals basis, Sigma-Aldrich), nitric acid ($HNO_3$, 65%, Suprapur, Sigma-Aldrich), oxalic acid ($C_2H_2O_4$, ACS Reagent, J.T. Baker), sulfuric acid ($H_2SO_4$, ACS reagent, 95.0–98.0%, Sigma Aldrich and OmniTrace, 93–98%, EMD Millipore), acetonitrile (MeCN, Sigma-Aldrich, ACS Reagent >= 99.5%), tartaric acid ($C_4H_6O_6$, Sigma Aldrich, ACS Reagent >= 99.5%), sodium hydroxide (NaOH, Sigma Aldrich, ACS reagent >= 97%), and MilliQ water (obtained from the Thermo Scientific MicroPure Ultrapure Water System, 18.2 MΩ cm). Transition metal mix 1 comprising of V, Cr, Mn, Fe, Co, Ni, Cu, Zn, Ag and Cd (2%, w/w $HNO_3$, 100 mg/L each, Sigma-Aldrich), transition metal mix 2 comprising of Ti, Zr, Hf, Nb, Ta, Mo, W and Re (2%, w/w $HNO_3$, 1% w/w HF, 100

mg/L each, Sigma-Aldrich), Lu ICP standard (1000 μg/mL, in 2% $HNO_3$, Assurance), Y ICP standard (10,000 ppm, in 5% $HNO_3$, GFS Chemicals), Na ICP standard (1000 μg/mL, in 2% $HNO_3$, Assurance), Rh ICP standard (1000 μg/mL, in 2% $HNO_3$, Assurance), Be ICP Standard (1000 ppm, <5% $HNO_3$, GFS Chemicals) were used in methodology development experiments with stable elements.

3.2.1.2 Column construction with ion-exchange and extraction chromatography resins

The experiments were conducted using the following resins: LN-extraction chromatographic resin (2 mL Cartridges, particle size 50-100 μm, Eichrom LN-R50-S), QMA strong anion exchanger resin (Sep-Pak Accell Plus QMA Plus Light Cartridge, Part no. WAT023525, Lot no. 034639256A).

3.2.1.3 Instruments

The drill bits used for drilling the tungsten beam-blocker were obtained from McMaster-Carr (Part number 8871A28). The separations were performed with a peristaltic pump (Ismatec® Reglo Peristaltic Pump with independent channel control) operated with pump tubing of 1.65-mm internal diameter, and with a syringe pump (New Era Pump Systems, NE-1000 SyringeONE one channel programmable syringe pump). During the separation method development, the identification and quantification of stable elements was performed with a 5900 Agilent ICP-OES together with the Agilent ICP Expert software. The radionuclides were detected and quantified with the HPGe Canberra Broad Energy BEGe γ-ray Detector (BE2020). Phosphor imaging of the tungsten foils was conducted with an Amersham Typhoon™ Biomolecular Imager (GE Healthcare).

3.2.2 Experimental setup

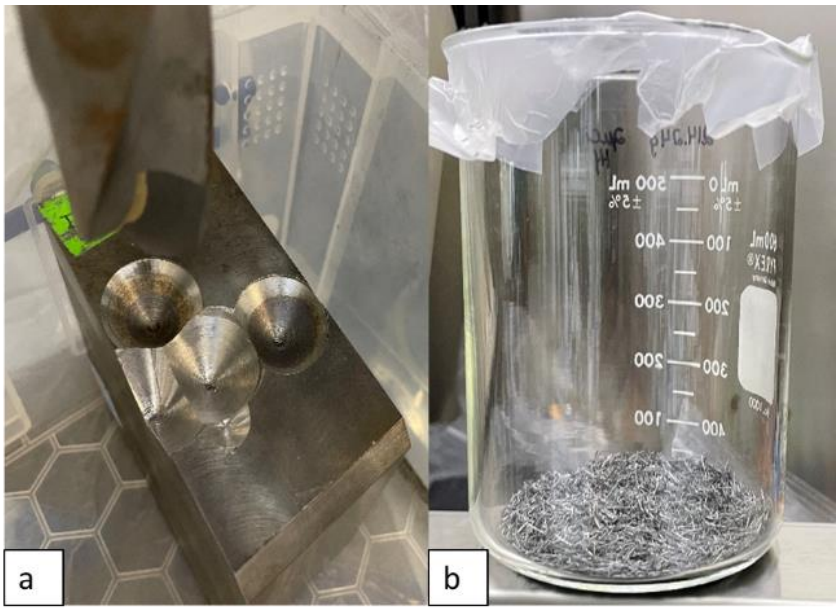


**Figure 3.2:** (a) The drilled holes in the most radioactive face of the tungsten beam-blocker using a carbide tipped steel bit and drill press is shown (b) Tungsten shavings resulting from the drilling process is shown.

Once NSCL was decommissioned, the beam-blocker was transferred to chemistry laboratory, and autoradiography was performed to identify the most radioactive face. The most radioactive face was then drilled out using a drill press with carbide tipped steel bits. The drill press was located inside of a fume hood with filtered ventilation, and enclosed in a large plastic bag during machining (to prevent dust migration). Drilling was done on the beam-spot and adjacent areas in batches and ~500 g tungsten shavings were collected for the extraction of radioisotopes. **Figure 3.2 (a)** shows the drilled beam-blocker where the drilling was done in batches. **Figure 3.2 (b)** shows the tungsten shavings collected after the drilling process.

3.2.3 Experimental quantification of radioisotopes through γ spectroscopy

Initially, the beam-blocker was measured as a whole using the HPGe Detector after using autoradiography to identify the most radioactive face and the spectra analysis was done using the

Canberra Genie 2000 software (Mirion Technologies). All energy spectra were analyzed by identifying the characteristic γ-ray emissions of the radionuclides embedded in the beam-blocker, performing background subtraction, and calculating activities based on the net photopeak areas. A list of radionuclides detected along with their half-lives and characteristic gamma lines are given in section 3.3. The average dead time was less than 5% for all the measurements. The energy and efficiency calibrations were performed with a $^{152}$Eu source (1 μCi, Eckert & Ziegler) with the activity evenly distributed in 10 mL of epoxy in a sealed 15 mL falcon tube at 15, 25, 50, 100, 150 and 180 cm from the face of the HPGe detector. To maintain a consistent geometry with the calibration, all resulting fractions were positioned in a fixed acrylic holder at the above-mentioned distances from the HPGe detector and collected and measured in 15 mL falcon tubes. Counting of material that did not fit the geometry specifications is described in further sections.

3.2.4 Separation chemistry development: Dissolution of the tungsten beam-blocker and radiochemical separation with resins

3.2.4.1 Dissolution of the tungsten beam-blocker

Initial dissolution testing was done with a piece of scrap heavy-met alloy obtained from NSCL. That same alloy was used to fabricate the beam blocker. The dissolution of the beam-blocker shavings was attempted in batches, and the procedure described here is representative of all dissolutions attempts. Approximately 0.25 g of the shavings were weighed into a 100 mL beaker and 5.0 mL of 10% $H_2O_2$ (v/v) was added. The reaction began in about a minute and the reaction vessel was placed into an ice-bath to curtail the vigorous reaction and bubbling. A total of 35 mL of 30% $H_2O_2$ was then added to the beaker 2.5 mL at the time. At this point, the addition of more peroxide did not result in vigorous bubbling; however, some grey dust size particles were still observed at the bottom of the beaker. Using peroxide strips, the concentration

of peroxide in the solution was determined and the beaker was left on heating at 65 °C, and then left overnight at room temperature. $H_2O_2$ concentration was once again determined using peroxide strips. The solution was again heated at 70 °C and was left for several hours to decrease the peroxide concentration. The dissolved solution is shown in **Figure 3.3 (a)**. At this stage, an aliquot was withdrawn from this dissolved solution and radionuclides were identified and quantified by gamma spectroscopy. The procedure was repeated with varying amount of shavings.

While most of the shavings dissolved in the first attempt, some undissolved dust (shown in **Figure 3.3 (b)**) was left behind. Dissolution was attempted in a controlled manner similarly in an ice-bath with approximately 290 mg of this dust by first adding 5 mL of 10% $H_2O_2$ followed by a total of 16 mL of 30% $H_2O_2$ (1 mL at the time with 10-15 min breaks in between additions). At this point, the beaker was removed from the ice bath and placed on the hot plate at 60 °C for 1.5 hours. Another 24 mL 30% $H_2O_2$ (2 mL at a time with breaks in between addition) was added and left overnight. Most of the dust was dissolved and addition of another 9 mL 30% $H_2O_2$ the following day and heating up the solution to 50 °C (2 mL at a time with breaks in between addition) dissolved the dust entirely. The peroxide test was also performed using strips and temperature was increased to allow the peroxide concentration to reduce.

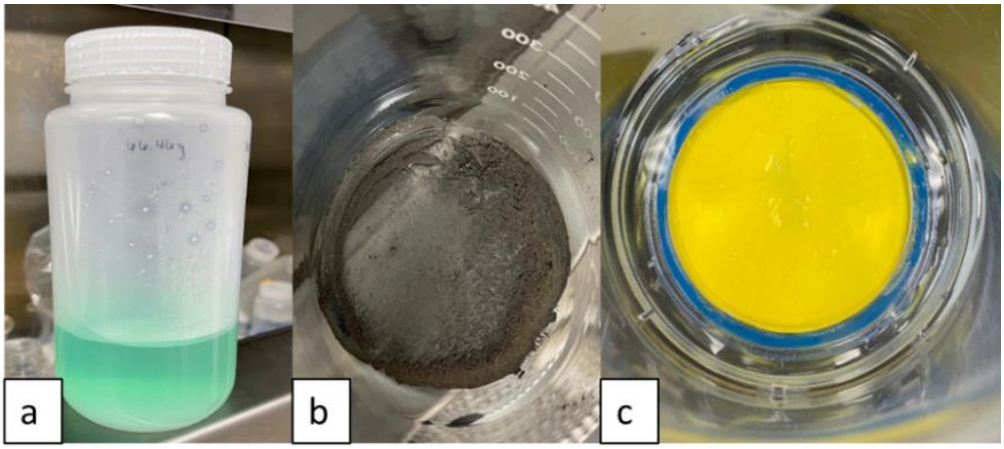


**Figure 3.3:** (a) The beam-blocker dissolved in 30% $H_2O_2$ is shown (b) the left-over tungsten beam-blocker shavings after the first round of dissolution is shown and it was dissolved separately (c) the tungstic acid precipitate after the de-bulking of tungsten with 7 M HCl is shown.

3.2.4.2 Precipitation reactions with the dissolved solution

In one instance, 5.2 mL of the dissolved solution was taken at a time and 10.1 mL of concentrated HCl was added. This was set up in the shaking incubator for 16 hours at 300 rpm at 60 °C. 50 mL tube with the solution was taken and centrifuged for 5 minutes at 4000 rpm following which the supernatant was decanted, passed through millex filters. The remaining precipitate was washed with 1 mL 7 M HCl in two rounds and combined with the supernatant from previous decantation. This process was repeated several times with varying amounts of dissolved solutions, and the supernatants were combined.

In instances when the dissolved solution volume was high, the solution volume was reduced in a rotary evaporator in batches prior to the tungsten precipitation step. Next, high molarity HCl (10.6 M HCl) was added to bring up the final molarity to 7 M HCl to induce precipitation. It was set up in the shaking incubator in the same manner described above. After settling and centrifugation, the supernatant was filtered with a 500 mL vacuum filtration flask

(0.22 µm PES membrane), as shown in **Figure 3.3 (c)** and the filtrand was washed with approximately 10 mL 7 M HCl.

3.2.4.3 Separation with LN resin and $^{172}$Hf/$^{172}$Lu generator

Following the process outlined in section 3.2.4.2, several batches of 7 M HCl supernatant were obtained and assayed with gamma spectrometry. These supernatant volumes were combined, and load solutions were prepared in 7 M HCl for loading on LN resin column. Separations were carried out using both the peristaltic pump and the syringe pump and the peristaltic pump was calibrated before each separation to ensure a constant flow rate.

As an example, a load solution (that was previously supernatant) of 28 mL was prepared for loading on the 2 mL LN cartridge preconditioned with 10 mL water followed by 10 mL 7 M HCl at a flow rate of 0.25 mL/min. Using the syringe pump, the prepared load solution was then loaded on the resin at a flow rate of 0.25 mL/min. 0.5 mL and 1 mL fraction volumes were collected of the load solution and analyzed on the HPGe for radionuclides that eluted with the load solution. 10 mL of 7 M HCl rinse solution was passed through the column to ensure a complete removal of radionuclides.$^{172}$Hf was left adsorbed onto the resin for the $^{172}$Lu daughter to grow in.

Elution cycles: The $^{172}$Lu daughter was eluted with 7 M HCl when required and 0.5 mL elute fractions were collected at a flow rate of 0.25 mL/min and analyzed on HPGe for breakthrough. The column was stored in 1 M HCl until the next elution cycle was performed.

3.2.4.4 Regeneration of $^{172}$Hf/$^{172}$Lu generator

The first step towards the regenerating of the above LN resin generator included eluting the adsorbed $^{172}$Hf with 12 mL 0.5 M Oxalic acid. This was done at a flow rate of 0.25 mL/min and 2 fractions were collected for HPGe analysis. Once the $^{172}$Hf was eluted from the column,

QMA resin was chosen for the hafnium-oxalic acid cleanup. The QMA resin was conditioned with 10 mL acetonitrile (flow rate of 1 mL/min), followed by 10 mL water (flow rate of 1 mL/min) and 10 mL 0.5 M Oxalic acid (flow rate of 0.25 mL/min) sequentially. This was followed by passing the 12 mL load solution at 0.25 mL/min. 10 mL MilliQ water was then passed through the cartridge to ensure complete washing of oxalic acid at 0.25 mL/min. $^{172}$Hf was then eluted from the cartridge with 10 mL of 1 M HCl (2 fractions total) followed by rinsing with 5 mL 2 M HCl at 0.25 mL/min. The fractions were monitored with HPGe throughout.

3.2.4.5 Establishment of new LN-resin generator

Once $^{172}$Hf was eluted from QMA resin, it was acidified to 7 M HCl for further loading and LN resin was chosen again for the new generator setup. It was also conditioned in a similar manner described in section 2.4.3. The load solution of $^{172}$Hf in 7 M HCl was then passed through the LN resin at 0.25 mL/min. Once $^{172}$Lu was allowed to grow in, the generator was eluted with 7 M HCl, 0.5 mL per fraction for $^{172}$Lu when required and the column was stored in 1 M HCl until the next elution was required. A schematic of the entire process is shown in **Figure 3.4**.

3.2.5 Quantification of stable elements with ICP-OES

Samples were measured using ICP-OES at different stages of the chemical processing by extracting an aliquot, diluting in 2% $HNO_3$, quantifying and analyzing with Agilent ICP software. Single and multi-elements standards in various dilutions (0.01 ppm - 1 ppm) were used to establish the calibration curves for the sample analysis. The emission lines which had the highest intensity for the different elements were chosen for analysis and the separation efficiency was determined as a percentage of the loaded amount for different elements.

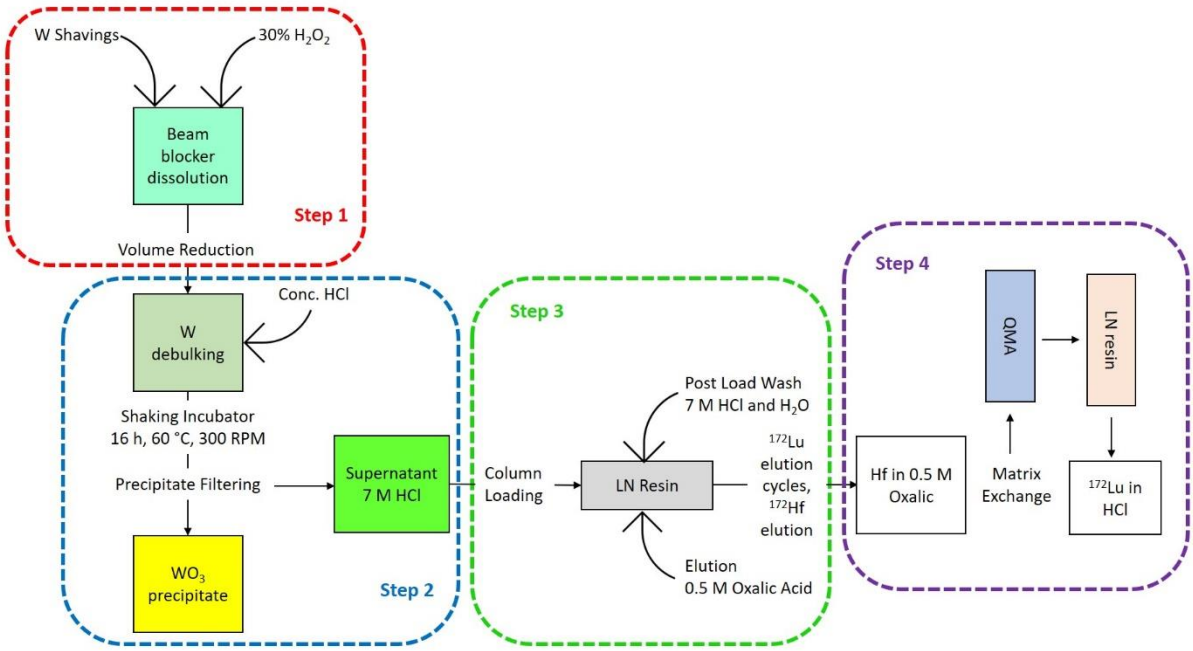


**Figure 3.4:** A schematic of the entire process of processing the tungsten beam-blocker from debulking, precipitation, separation on resin, and generator set-up is shown.

## 3.3 Results and discussion

### 3.3.1 Identification of radionuclides in the tungsten beam-blocker

The available $^{172}$Hf was contained throughout the beam blocker with highest concentrations near the beamstrike that was approximately 5 cm$^2$ aerially, and a few mm deep. While all faces of the beam-blocker were surveyed initially through γ spectroscopy and autoradiography, only the most active face, with the beam-spot was found to have enough $^{172}$Hf to warrant chemical processing. Examples of isotopes embedded in the other faces not displaying the beam-spot include the cobalt isotopes.

Not much can be commented on how these radioisotopes were produced since there is limited information on which beams were stopped in the beam blocker over its many years of service. Several radioisotopes were identified that were likely produced due to interactions between fast secondary protons and neutrons with W, Cu, and Ni (e.g. $^{172}$Hf), and others were

found that were likely implanted during heavy-ion irradiation (e.g. $^{110m}$Ag). The complete list of radioisotopes that could be identified is given in **Table 3.1**.

The pure alpha emitter $^{148}$Gd could only be detected with liquid scintillation counting after cursory separations were performed to isolate $^{151}$Gd (method not presented here). Similarly, radionuclides with small gamma branches were only identifiable after the bulk of the gamma-emitting background was removed in chemical separations. As more separations are performed in the future, additional radionuclides may be found.

Table 3.1: List of radionuclides found in the tungsten beam-blocker measured through repeated gamma spectroscopy at different stages of chemical processing [1].

| **Radionuclide** | **$T_{1/2}$** | **Gamma rays (keV)** | **Radionuclide** | **$T_{1/2}$** | **Gamma rays (keV)** | **Radionu-clide** | **$T_{1/2}$** | **Gamma rays (keV)** |
|---|---|---|---|---|---|---|---|---|
| $^{172}$Hf | 1.87 y | 23.9 (20.3 %), 125.8 (11.3 %) | $^{184}$Re | 35.4 d | 903.2 (38.1 %), 792 (37.7 %) | $^{145}$Sm | 340 d | 61.2 (12.1 %) |
| $^{172}$Lu | 6.7 d | 1093.6 (63 %), 900.7 (29.8 %), 181.5 (20.6 %) | $^{184m}$Re | 169 d | 104.7 (13.6 %) | $^{181}$W | 121.2 d | 6.24 (1.0 %) |
| $^{173}$Lu | 1.7 y | 272.1 (21.2 %), 78.6 (11.9 %) | $^{54}$Mn | 312.2 d | 834.8 (99.9 %) | $^{143}$Pm | 265 d | 741.9 (38.5 %) |
| $^{175}$Hf | 70 d | 343.4 (84 %) | $^{182}$Ta | 114.7 d | 67.7 (42.9 %), 1121.2 (35.2 %) | $^{101}$Rh | 3.3 y | 198.0 (73 %), 127.2 (68 %) |
| $^{7}$Be | 53.2 d | 477.6 (10.44 %) | $^{133}$Ba | 10.5 y | 356 (62.0 %), 80.9 (32.9 %) | $^{109}$Cd | 461.9 d | 88.0 (3.6 %) |
| $^{22}$Na | 2.6 y | 1274.5 (99.9 %) | $^{68}$Ga | 67.7 m | 1077 (3.22 %) | $^{125}$Sb | 2.8 y | 427.8 (29.6 %), 600.5 (17.65 %) |
| $^{56}$Co | 77.2 d | 846.77 (99.9 %), 1238.28 (66.46 %) | $^{68}$Ge | 270.9 d | - | $^{144}$Pm | 363 d | 696.4 (99.5 %), 618.01 (98 %) |

Table 3.1 (cont'd)

| | | | | | | | | |
|---|---|---|---|---|---|---|---|---|
| $^{57}$Co | 271.7 d | 122.1 (85.6 %), 136.5 (10.7 %) | $^{46}$Sc | 83.7 d | 889.27 (99.98 %), 1120.54 (99.98 %) | $^{42}$K | 12.3 h | 1524.6 (18.08 %) |
| $^{110m}$Ag | 249.8 d | 657.7 (95.6 %), 884.6 (75 %) | $^{102}$Rh | 207.3 d | 475 (46 %), 628 (4.5 %) | | | |
| $^{60}$Co | 1925.3 d | 1173.2 (99.85 %), 1332.5 (99.9 %) | $^{102m}$Rh | 3.7 y | 475 (95 %), 631.3 (56 %) | | | |
| $^{88}$Zr | 83.4 d | 392.8 (97.3 %) | $^{148}$Gd | 71.1 y | - | | | |
| $^{88}$Y | 106.6 d | 898 (93.7 %), 1836 (99.2 %) | $^{151}$Gd | 123.9 d | 243.2 (5.6 %), 153.6 (6.2 %) | | | |

3.3.2 Dissolution of the tungsten beam-blocker

As the activity was contained in the face of the beam blocker identified by autoradiography, the chemical processing of $^{172}$Hf from the entire beam blocker mass was not necessary. However, even with partial dissolution of the beam blocker, a considerable amount of the tungsten alloy mass had to be chemically processed.

The dissolution of the shavings was done in batches using an optimized volume of 125.5 mL 30% $H_2O_2$ per gram of the tungsten beam-blocker shavings, and the prime advantage of the dissolution described in section 3.2.4.1 is the non-requirement of HF. Using peroxide strips, the concentration of peroxide during the dissolution stage in the solution was determined to be >50 ppm.

The rate of bubbling was a good indication of how the reaction was proceeding during the dissolution of shavings. Moderate to little bubbling was a good indication to add more peroxide. Since the reaction was vigorous, caution was observed throughout, and dissolution was performed in batches. $H_2O_2$ concentration was determined again using peroxide strips towards

the near end of the dissolution process and determined to be around 10 ppm. Finally, at the end of dissolution, peroxide concentration dropped to 2 ppm and later to <1 ppm. The solution once dissolved was determined to be 0.9% Cu, 3.9% Ni and 97.2% W which was verified through ICP-OES. Approximately 77.1% of the tungsten shavings were dissolved in the first attempt (**Figure 3.3 (a)**) and 22.9% stayed as the black residue (**Figure 3.3 (b)**) which was dissolved separately. This was also determined using ICP-OES.

3.3.3 De-bulking of tungsten (precipitation) and separation process

A precipitation of the bulk tungsten matrix while keeping the radioactive species in solution represents a viable alternative to the ion exchange based separation. In several pre-experiments, a precipitation of tungsten as yellow tungsten trioxide (its hydrated form is tungstic acid) in solutions of >3M HCl has been observed [7]. By performing such a precipitation step, the desired radionuclides are transferred into an HCl matrix and there is a considerably better availability of distribution coefficient data for HCl media. Additionally, large amounts of tungsten could cause interferences with the elution of other species from the ion exchange column, hence precipitation was chosen.

The precipitation of bulk tungsten with 7 M HCl results in tungstic acid $H_2WO_4$ and tungsten dichloride dioxide, or tungstyl chloride $WO_2Cl_2$ (speciation was not determined in this work), shown in **Figure 3.3 (c)**. The HCl molarity was optimized to be 7 M HCl for the precipitation process and 99.7% tungsten was successfully de-bulked with 22(1)% Cu and 11(1)% Ni also being co-precipitated. De-bulking of tungsten was also necessary because it was observed that the separation efficiency of the proceeding step drops as the mass of tungsten is increased. As a note, the yellow precipitate was readily dissolvable in NaOH solutions, so it should be possible to recover co-precipitated radioisotopes, if needed in the future.

For the separation of $^{172}$Hf from the remainder tungsten and other radionuclides after precipitation, LN resin was used. Di(2-ethylhexyl)phosphoric acid (HDEHP) based resin is widely used for adsorbing hafnium and allowing trivalent lutetium to elute out [8]. With 7 M HCl $^{172}$Hf, Ge, Zr was held up in the column, while Lu, Gd, Pm, Co isotopes and stable W, Cu, Ni were washed down the column. The radiolanthanides eluted from the load fraction can be further processed and chemically separated. $^{172}$Hf stayed on the column and the gamma lines of 125.8 and 23.9 KeV of $^{172}$Hf are not present in the eluted fractions from the LN resin (see **Figure 3.6**), thus indicating a successful separation from other radionuclides. Approximately (80 ± 2)% $^{172}$Hf could be eluted with 0.5 M Oxalic acid.

The $^{172}$Hf/$^{172}$Lu generator was eluted with 7 M HCl and used for PAC experiments and (104 ± 2)% $^{172}$Lu could be eluted from the generator within 4 mL. The entire separation scheme is shown in **Figure 3.5** with the aim of tracking hafnium. **Figure 3.6** shows the gamma spectrum of the load fractions to show absence of hafnium and **Figure 3.7** shows the presence of hafnium on the column. An elution profile of the eluted $^{172}$Lu from the regenerated generator is shown in **Figure 3.9** and gamma spectra is shown in **Figure 3.8**.

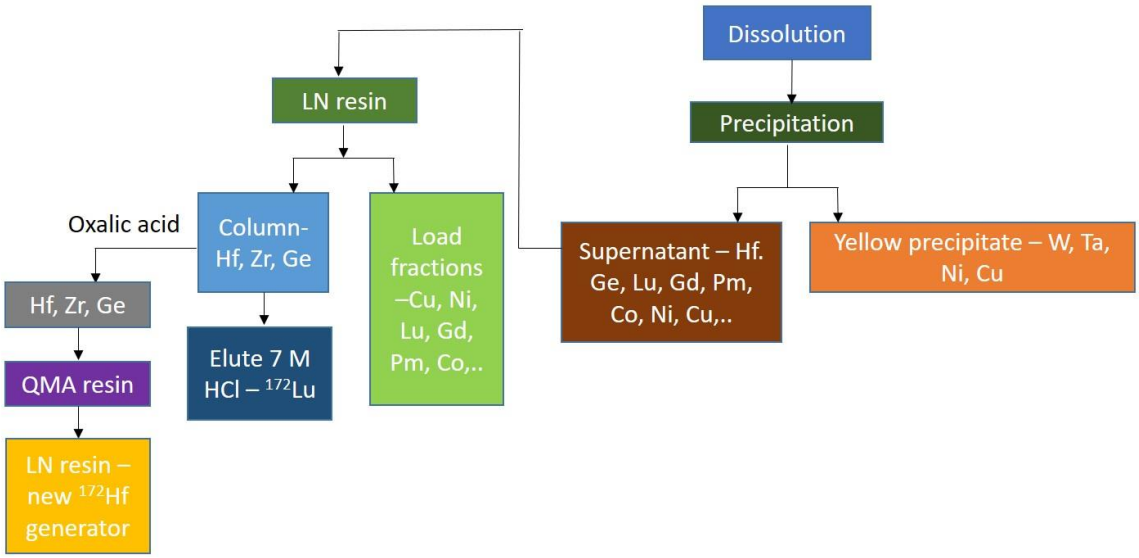


**Figure 3.5:** A schematic is shown with the radioisotopes separating at different stages. The primary aim was to track $^{172}$Hf.

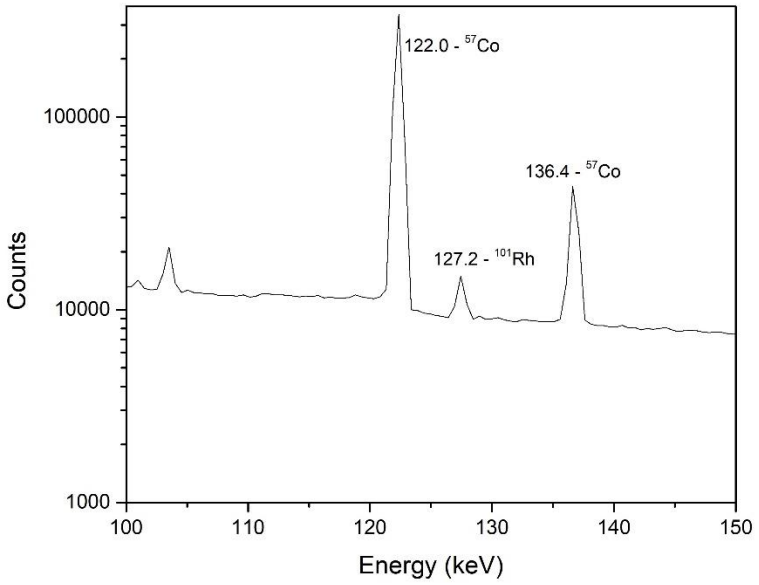


**Figure 3.6:** A gamma spectrum of the load solution passing through the column indicating the absence of the $^{172}$Hf peak.

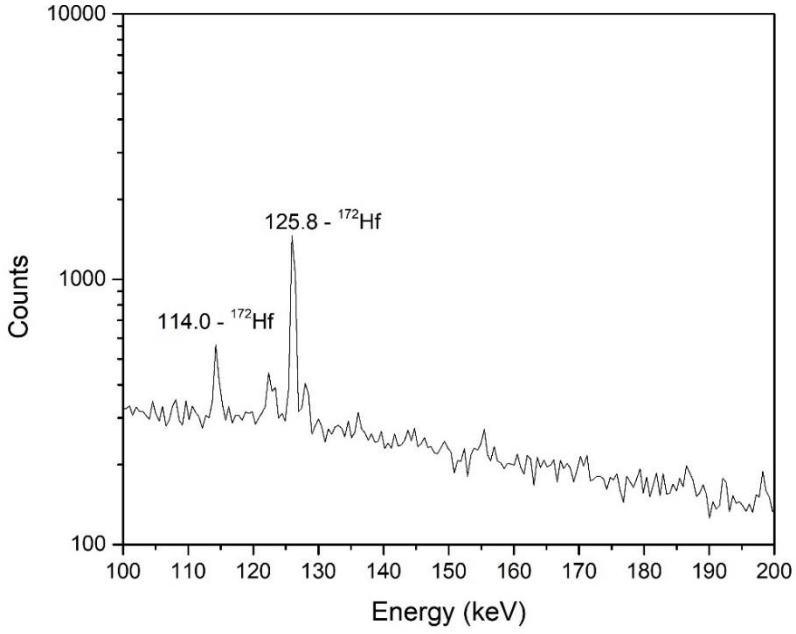


**Figure 3.7:** A gamma spectrum of the generator column indicating the presence of the $^{172}$Hf peak is shown.

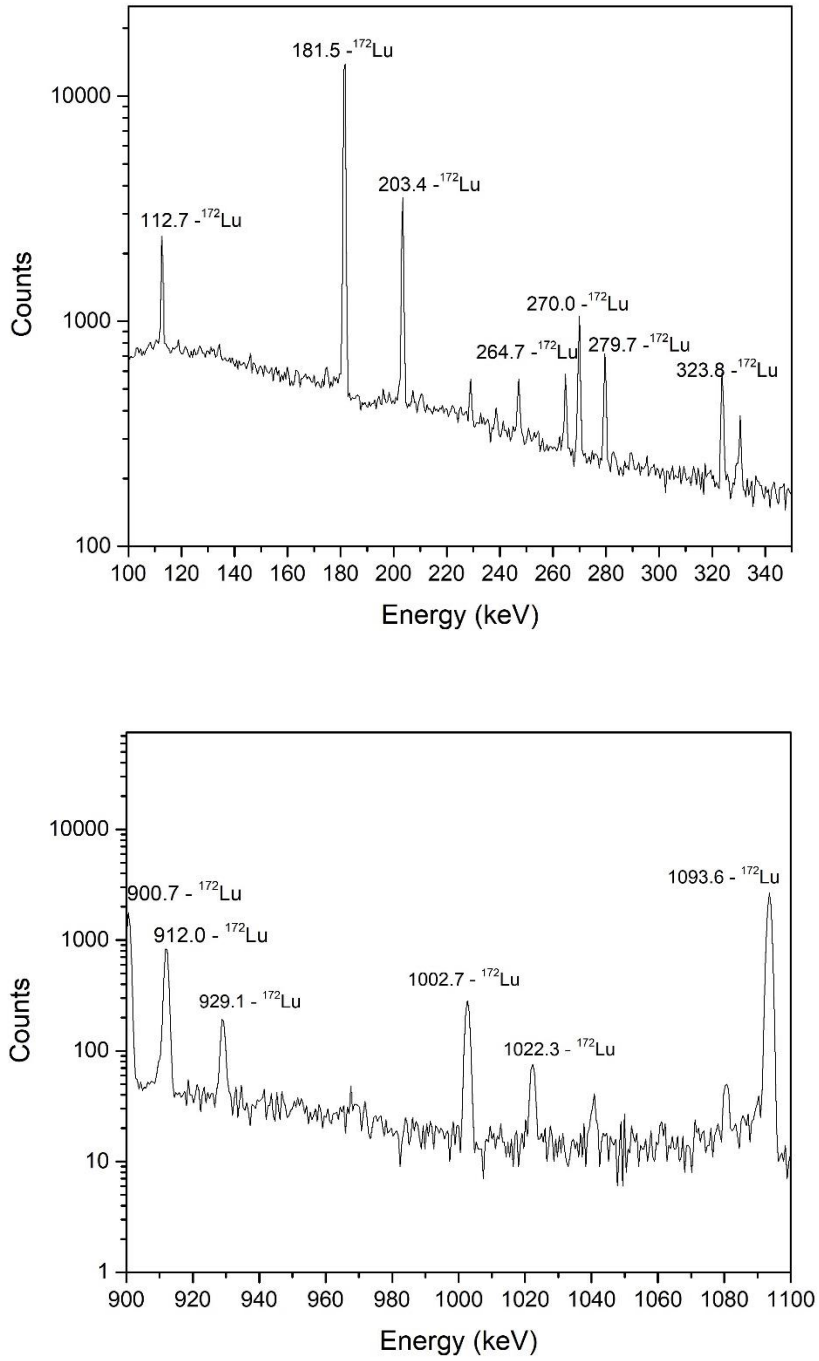


**Figure 3.8:** Gamma spectra, 100-350 keV (top) and 900-1100 keV (bottom) of a 0.5 mL fraction eluted from the regenerated $^{172}$Hf/$^{172}$Lu generator showing the presence of $^{172}$Lu peaks, and absence of $^{172}$Hf peak.

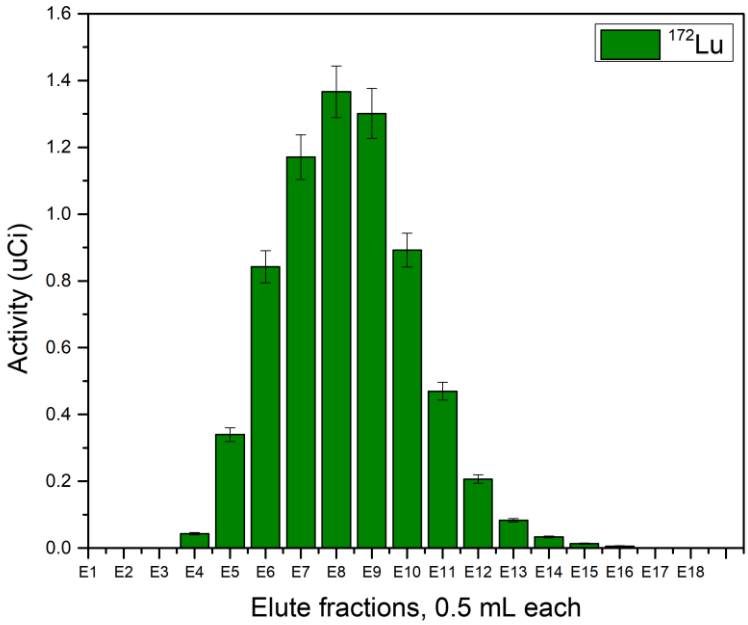


**Figure 3.9:** An elution profile of the eluted daughter $^{172}$Lu with 7 M HCl from the generator.

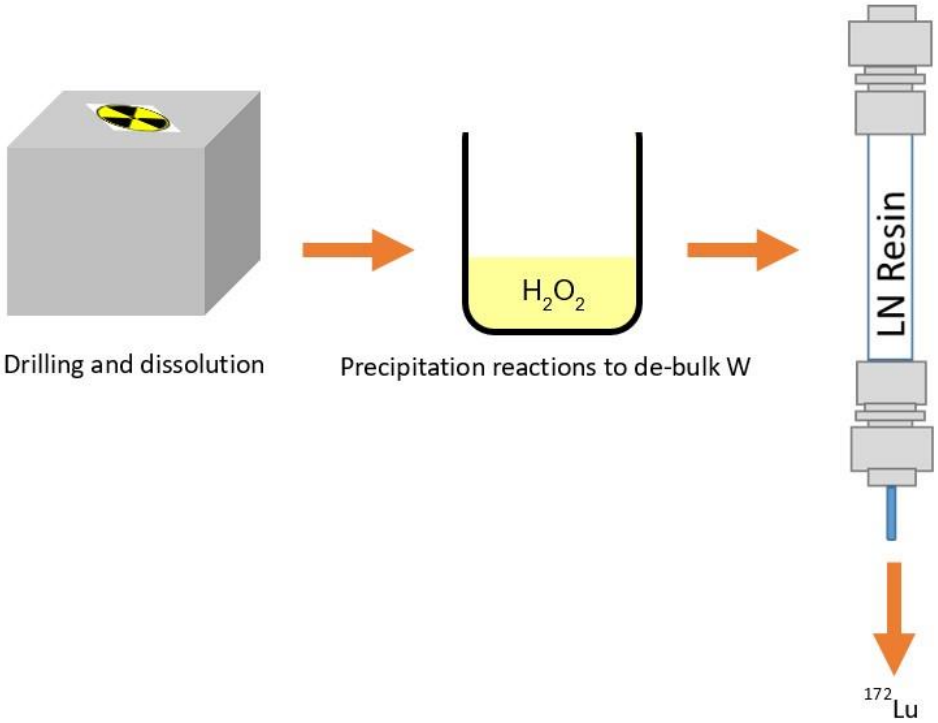


**Figure 3.10:** A schematic summarizing the process followed in this chapter.

## 3.4 Conclusion

Since tungsten and tungsten alloys (e.g. ‘heavymet’ W 95%, Cu 1.5%, and Ni 3.5%) will be routinely used to stop beams at FRIB and other facilities, performing this experiment was important to establish methods for recovering implanted and induced radionuclides, such as $^{172}$Hf from those materials. A schematic is given in **Figure 3.10** of the process that was detailed in this chapter. The generator that was set up in this chapter will be compared to those set up in the next chapter and comparison will be drawn between harvesting through isotope harvesting and production through a conventional technique.

## REFERENCES


[1] "National Nuclear Data Center." Accessed: Mar. 22, 2024. [Online]. Available: https://www.nndc.bnl.gov/nudat3/

[2] R. L. Rasera and A. Li-Scholz, "Perturbed-Angular-Correlation Study of Electric-Quadrupole Interactions in 172Yb in Thulium Metal and Oxide Lattices," *Phys Rev B*, vol. 1, no. 5, pp. 1995–2006, Mar. 1970, doi: 10.1103/PhysRevB.1.1995.

[3] A. Lerf and T. Butz, "Nuclear quadrupole interactions in compounds studied by time differential perturbed angular correlations/distributions," *Hyperfine Interact*, vol. 36, no. 3, pp. 275–370, 1987, doi: 10.1007/BF02395636.

[4] R. Valentini and R. Vianden, "Angular correlation studies on 172Lu(172Yb) in GaN and measurements at low temperatures," *Hyperfine Interact*, vol. 197, no. 1, pp. 149–153, 2010, doi: 10.1007/s10751-010-0229-9.

[5] S. Chakraborty, S. Pallada, J. T. Pedersen, A. Jancso, J. G. Correia, and L. Hemmingsen, "Nanosecond Dynamics at Protein Metal Sites: An Application of Perturbed Angular Correlation (PAC) of γ-Rays Spectroscopy," *Acc Chem Res*, vol. 50, no. 9, pp. 2225–2232, Sep. 2017, doi: 10.1021/acs.accounts.7b00219.

[6] L. Hemmingsen, K. N. Sas, and E. Danielsen, "Biological applications of perturbed angular correlations of γ-ray spectroscopy," *Chem Rev*, vol. 104, no. 9, pp. 4027–4061, Sep. 2004, doi: 10.1021/cr030030v.

[7] F. W. E. Strelow, "Distribution coefficients and cation-exchange behaviour of 45 elements with a macroporous resin in hydrochloric acid/methanol mixtures," *Anal Chim Acta*, vol. 160, no. C, pp. 31–45, 1984, doi: 10.1016/S0003-2670(00)84506-7.

[8] P. Horwitz and D. Mcalister, "Eichrom's LN Series of Resins: Characterization and Novel Applications," 2008.

[9] "Virtual tour." Accessed: Mar. 22, 2024. [Online]. Available: https://nscl.msu.edu/public/virtual-tour.html

# APPENDIX

THEORY OF TECHNIQUES UTILIZED IN CHAPTER 3

Perturbed Angular Correlation Spectroscopy (PAC)

PAC is a technique providing insights into the chemical environment surrounding a target metal ion by probing its nuclear spin interaction with an electric field gradient [5], [6]. For this technique to be effective, it necessitates the presence of cascade gamma rays emitted by the probe nucleus and a lifetime of the intermediate level exceeding 1 nanosecond, a criterion that $^{172}$Lu fulfills. The nuclear level diagram illustrating the characteristics of $^{172}$Lu is depicted in **Figure 1.5** in Chapter 1. The $^{172}$Lu eluted samples were transferred to FRIB and placed between 14 $LaBr_3$ scintillation detectors that use 1.5 x 1.5 inch $LaBr_3$(Ce) crystals, arranged in a circular array, operating at room temperature and the purpose was to measure the correlation of γ-rays of $^{172}$Lu.

# CHAPTER 4: $^{172}$Hf HARVESTING FROM LUTETIUM FOIL TARGET AT THE BROOKHAVEN LINEAR ISOTOPE PRODUCER

This chapter details the conventional method of producing $^{172}$Hf at the BLIP by the proton irradiation of natural lutetium metal foil through the $^{175}$Lu(p,4n)$^{172}$Hf nuclear reaction pathway. The production was carried out to obtain pure $^{172}$Lu (PAC probe) generated from the extracted parent, $^{172}$Hf. $^{172}$Lu can also be used a surrogate for the more popular $^{177}$Lu theragnostic agent to test chemistry and the PAC technique has the potential to provide insights into radiolabeling, pharmacokinetics, in new Lu-based pharmaceuticals.

Following irradiation, the lutetium foil was dissolved in HCl and subsequent separation of $^{172}$Hf radioisotope from bulk lutetium and other lutetium isotopes was achieved using various columns loaded with LN resin, ZR resin, as well as in-house synthesized hydroxamate and methyl-substituted hydroxamate resins. The efficacy of these different $^{172}$Hf/$^{172}$Lu resin-based generator systems was assessed to monitor $^{172}$Hf breakthrough. Subsequently, all four generators were consolidated into a single higher activity generator (130 μCi) using ZR resin, which exhibited similar performance characteristics to the original ZR resin generator. This is detailed in this chapter and a comparison is also drawn with the $^{172}$Hf/$^{172}$Lu generator set up from Chapter 3.

The experimental methodologies described in Chapter 3 and 4 have advanced the development of methodologies and our understanding for producing high-purity $^{172}$Lu, which is essential for PAC and radiolabeling studies.

## 4.1 Introduction

The pioneering FDA-approved radiopharmaceutical, Lutathera® [$^{177}$Lu]Lu-DOTATATE, for radioligand therapy (RLT), has gathered significant attention in cancer treatment, indicating a

growing interest in $^{177}$Lu-based radiopharmaceuticals [1]. Research facilities around the world aiming to innovate new $^{177}$Lu-based therapeutics find value in the ability to conduct lutetium radiolabeling tests independently of reactor irradiation schedules. An effective substitute for exploring lutetium chemistry is $^{172}$Lu ($t_{1/2}$ = 6.7 days), which can be generated in high purity from its long-lived parent, $^{172}$Hf ($t_{1/2}$ = 1.87 years) [2].

Amongst the possible routes to obtain $^{172}$Lu, some options for its production are: (I) irradiation of Yb with protons or deuterons such as $^{nat}$Yb(p,xn)$^{172}$Lu, $^{172}$Yb(p,n)$^{172}$Lu, $^{nat}$Yb(d,xn)$^{172}$Lu and $^{172}$Yb(d,2n)$^{172}$Lu [3], [4], (II) $^{169}$Tm(α,n)$^{172}$Lu reaction [5] (III), $^{172}$Hf/$^{172}$Lu radionuclide generators [6], [7], and (IV) $^{170}$Er($^{7}$Li,5n)$^{172}$Lu reaction [8]. For the purpose of comparison with the $^{172}$Hf/$^{172}$Lu generator set up detailed in Chapter 3, proton irradiation of natural lutetium foil was chosen as shown in **Figure 4.1**.

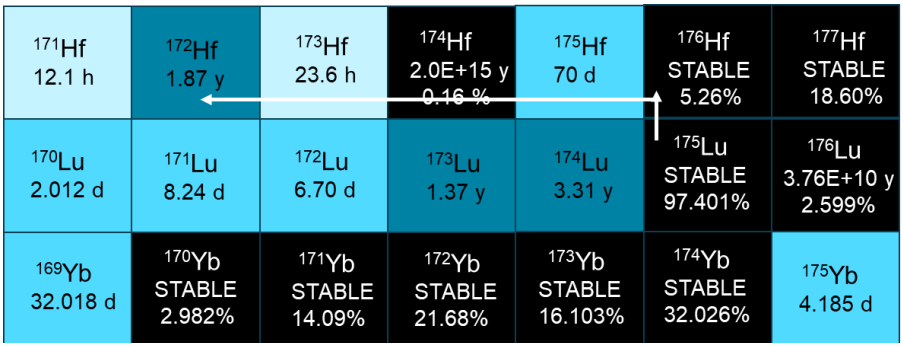


**Figure 4.1**: Schematic of a section of the chart of the nuclides demonstrating the $^{175}$Lu(p,4n)$^{172}$Hf reaction when a natural lutetium foil is irradiated for the production of $^{172}$Hf.

While extensive literature exists on the radiopharmaceutical applications of $^{177}$Lu, there are not studies focusing on the development of $^{172}$Hf/$^{172}$Lu generator setups, which is the primary focus of this chapter [7], [9], [10], [11]. Specifically, there is a lack of column-based generators, despite the investigation of numerous promising substrates for analogous separations like $^{44}$Ti/$^{44}$Sc and $^{89}$Zr/$^{nat}$Y, which are widely employed in radiopharmaceutical production [11].

The four resins used in this study include ZR resin, in-house synthesized hydroxamate resin, methyl-substituted hydroxamate resin, and LN resin [12], [13], [14], [15]. Dirks et al. shows that ZR resin, having the hydroxamate functionality, exhibits less selectivity for lutetium in the presence of HCl, thus enabling the separation of hafnium from lutetium [12]. The hafnium can subsequently be eluted from the columns by complexing it with oxalic acid, behaving similarly to its chemical analogue zirconium [16]. Similarly for LN resin, which is based on di-(2-ethylhexyl)phosphoric acid (HDEHP), also shows selectivity for hafnium over lutetium in high molarity hydrochloric acid solutions [17]. The methodologies developed for chemical separation of hafnium and lutetium in this chapter also hold significant relevance in isotope geochemistry separations, given that Hf-Lu serves as an important alternative chronometer to Sm-Nd [18], [19], [20], [21], [22].

Once the generators were set up, a comparative analysis was conducted with the four resins, considering various parameters such as elution volumes, elution patterns, and the occurrence of $^{172}$Hf breakthrough. Following this, the generators were regenerated into a single higher activity generator to enable the cyclic elution of higher activity of $^{172}$Lu. The eluted high purity $^{172}$Lu was used for PAC spectroscopy measuring the lifetimes of excited states and the angular correlations of $\gamma$ rays emitted in cascade using the $LaBr_3$(Ce) detector array at FRIB and radiolabeling small peptides (results not presented here).

## 4.2 Experimental

### 4.2.1 Materials

#### 4.2.1.1 Reagents

The lutetium foils (99%, 0.25 mm thick, Goodfellow) were cleaned with ethanol (ACS Reagent, 99.5%, Sigma Aldrich) in preparation for the irradiation. The dissolution of the

lutetium foils and the chemical processing post-irradiation was performed with the following reagents: hydrochloric acid (HCl, Optima Grade, 32.0-35.0%, Fisher Chemical and 99.99% Trace metals basis, Sigma-Aldrich), nitric acid ($HNO_3$, 65%, Suprapur, Sigma-Aldrich), oxalic acid ($C_2H_2O_4$, Analytical Reagent, Mallinckrodt), oxalic acid dihydrate (ACS Reagent, J.T.Baker) acetonitrile (MeCN, Sigma-Aldrich, ACS Reagent >= 99.5%) and MilliQ water (Deionized Milli-Q water, 18.20 MΩ, Millipore and Thermo Scientific MicroPure Ultrapure Water System, 18.20 MΩ cm). Hafnium ICP Standard (1000 µg/mL, in 2% HCl, Assurance), lutetium ICP Standard (1000 µg/mL, in 2% $HNO_3$, Assurance), and lutetium (III) chloride hexahydrate (>99.99% trace metal basis, Sigma Aldrich) were used in methodology development experiments with stable elements.

Synthesis of the covalently bonded hydroxamate and methyl-substituted hydroxamate resins was performed with the following reagents: Accell$^{TM}$ PLUS CM resin (Waters, Lot: 006501071), 2,3,5,6-Tetrafluorophenol (97%, Alfa Aesar, Lot: 10233607), 1-Ethyl-3-(3′-dimethylaminopropyl)carbodiimide (EDAC) hydrochloride (98%, Millipore Sigma, Lot: 3996375), hydroxylamine hydrochloride (ReagentPlus$^{R}$, 99%, Sigma-Aldrich, SourceMKCS8067), N Methylhydroxylamine hydrochloride (98%, Sigma-Aldrich, Source:STBJ7422), Acetonitrile (ACS Reagent, ≥99.5%, Sigma-Aldrich, source:SHBN8541), methyl alcohol (ACS Reagent, ≥99.8%, Sigma-Aldrich, source:MKCPO477).

4.2.1.2 Column construction with Extraction Chromatographic Resins

The experiments conducted at Brookhaven lab included using the following resins and columns - LN-extraction chromatographic resin (Di-(2-ethylhexyl)phosphoric acid, particle size 100-150 µm, Eichrom) was slurry packed in columns and employed for the separations. The columns used for them were Glass chromatography columns (Bio-Rad, 1.0 x 5 cm, Econo-Column

Chromatography Columns). Parts from Low Pressure Fittings Kit obtained from Bio-Rad were used to connect tubing (Silicone tubing, 0.8 mm ID, Bio-Rad) to the column. A piece of glass wool was inserted on the top end of the columns to hold the resin in place. The QMA cartridge used was obtained from Waters Corp (Sep-Pak Accell Plus QMA Plus Light Cartridge, 130 mg Sorbent per Cartridge, 37 - 55 μm).

The experiments conducted at MSU included the use of ZR-extraction chromatographic resin (2 mL Cartridges, particle size 50-100 μm, Eichrom ZR-R10-S), LN-extraction chromatographic resin (2 mL Cartridges, particle size 50-100 μm, Eichrom LN-R50-S), QMA strong anion exchanger resin (Sep-Pak Accell Plus QMA Plus Light Cartridge, Part no. WAT023525, Lot no. 034639256A). In-house synthesized hydroxamate and methyl-substituted hydroxamate resin was slurry packed in columns and employed for the separations. The column was constructed from rigid polycarbonate tubing (3/8″ OD, 1/4″ ID, McMaster-Carr, PN:9176T1) and chemical-resistant push-to-connect fittings (Straight Reducer, for 3/8″ x 1/4″ Tube OD). Two pieces of glass wool were inserted on each end of the column to hold the resin in place.

4.2.1.3 Instruments

At Brookhaven Lab, the stable and radiochemical separations were performed with a peristaltic pump (Bio-Rad) operated with tubing of 0.8 mm internal diameter. During the separation method development, the identification and quantification of stable lutetium and hafnium was performed with a Perkin Elmer Optima 7300 Inductively coupled plasma-optical emission spectrometer (ICP-OES) together with the Syngistix software. The radionuclides were detected and quantified with an Ortec HPGe γ-ray Detector. At MSU, the separations were performed with a syringe pump (New Era Pump Systems, NE-1000 SyringeONE one channel

programmable syringe pump) and the radionuclides were detected and quantified with an HPGe Canberra Broad Energy BEGe γ-ray Detector (BE2020).

4.2.2 Experimental setup

4.2.2.1 Target design and irradiation

**Figure 4.2:** Natural lutetium foil enclosed between aluminum target holder and held in place by screws is shown.

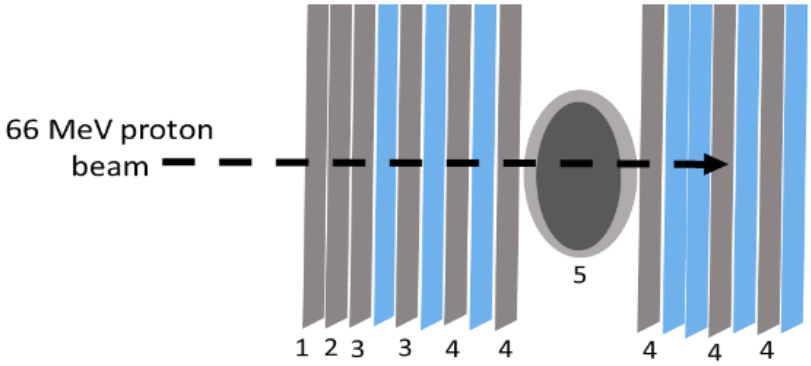


**Figure 4.3:** A schematic of the target assembly at BLIP is shown. Lutetium foil labeled 5, sandwiched between several components of beryllium window labeled 1, AlBeMet window labeled 2, water gaps in blue, stainless steel window labeled 3, and aluminum window labeled 4, in the beamline is shown.

The natural lutetium foil (97.4% $^{175}$Lu and 2.6% $^{176}$Lu), with weights of 1.5836 g (target 1) and 1.4707 g (target 2), approximately 0.254 mm thick and 28.5 mm in diameter, were inserted into a screw-bolted aluminum target holder crafted at BNL, following ethanol cleaning, as depicted in **Figure 4.2** [23]. Two proton irradiations were conducted at the BLIP using a focused beam with incident energies of 66 MeV (21.05 hours, 0.48 μA) and 117 MeV (23.99

hours, 2.82 μA). The attenuation of the beam in the natural lutetium foil target and other beamline components was estimated using the SRIM (Stopping and Range of Ions in Matter) compilation [24]. For these two irradiations, the other components included the beam passing through the following components in that order: Be window (beryllium), AlBeMet window (AlBeMet), beamline window (stainless steel), water gap, BOX front window (stainless steel), water gap, aluminum degrader (Aluminum), water gap, bolted holder window (Aluminum), Lutetium foil (Lutetium), Bolted holder back (Aluminum), water pocket, water gap, aluminum degrader (Aluminum), water gap, aluminum degrader (Aluminum), and water gap. A schematic representation is provided in **Figure 4.3**. Al, Cu, and Ni foils served as monitor foils for the second target.

4.2.3 Theoretical production yield of radioisotopes with FLUKA

The excitation functions and the stopping characteristics of the particle beam in the target material need to be considered when the beam energy and target thickness for an irradiation needs to be determined. For this work, the theoretical activities for each isotope were obtained by simulating the target array (above-mentioned components of beamline windows, water cell, degraders, and target foil) in the Monte Carlo particle transport code FLUKA (**Figure B.1**.). The calculations were performed using the average beam intensity and irradiation duration matching the two irradiation scenarios using the default FLUKA parameters for activation and recommended for secondary particle generation and transport. Comparison was made for the activities that were calculated and to those determined in this work. The target array and the energy propagation calculations for 117 and 66 MeV beam have also been shown in the section 4.3.1.

4.2.4 Experimental production yield of radioisotopes through γ spectroscopy

Following the irradiation, the targets underwent measurement at MSU and Brookhaven lab using an HPGe Detector, with spectra analysis conducted using the Canberra Genie 2000 software (Mirion Technologies) at MSU and the GammaVision-32 software, version 6.01 at Brookhaven lab. Both these software packages facilitated the analysis of energy spectra, including identification of characteristic γ-ray emissions of the different radioisotopes, background subtraction, and activity calculations based on net photopeak areas. **Table 4.1** and **Table 1** in Appendix presents the gamma lines utilized for activity assessment across the separations. Energy and efficiency calibrations of HPGe detector were carried out using a mixed gamma solution prepared from NIST traceable calibration standard (Eckert and Ziegler Analytics, GA, USA), positioned 10-15 cm from the detector at Brookhaven Lab to ensure accurate quantification. For precise quantification, aliquots of each collected fraction from the radiochemical separations were extracted, diluted with MilliQ water in 3 mL Eppendorf screw-cap conical centrifuge tubes, and analyzed with γ-ray spectroscopy. During all the measurements, the average dead time remained below 3%. At MSU, the energy and efficiency calibrations were done with a $^{152}$Eu source (1 μCi, Eckert & Ziegler Analytics) distributed evenly in 10 mL of epoxy within a sealed 15 mL Falcon tube at distances of 15, 25, 50, 100, and 180 cm from the face of the HPGe detector. In this case, the average dead time during measurements was kept below 5%. To maintain consistency in geometry with calibration, all resulting fractions from separations were collected and measured in 15 mL Falcon tubes, positioned in a fixed acrylic holder at the specified distances from the HPGe detector, as with previous experiments in previous chapters. Both targets underwent a decay period of several weeks to allow for the decay of shorter-lived species before initiating chemical processing.

### 4.2.5 Separation chemistry development

#### 4.2.5.1 Dissolution of irradiated targets and radiochemical separation with resins

The initial disassembly of the first lutetium target involved removing the screws in a hot cell, after which the lutetium foil was dissolved in a fume hood incrementally in 20 mL 1 M HCl and 20 mL 2 M HCl, added in 5 mL batches. While most of the foil dissolved upon treatment with HCl, residual black residue was observed, needing filtration of the solution. Scaling up the solution to a total volume of 50 mL with 7 M HCl prepared it for loading onto resin. At this stage, an aliquot was extracted from the target solution to quantify the quantities of hafnium and lutetium isotopes via gamma spectroscopy. Concentrated HCl was introduced to the remaining black residue in an attempt to dissolve it, employing heating to elevate the temperature to around 250°C.

For the second lutetium foil, dissolution was done with 12 mL 7 M HCl in 2 mL increments dropwise, followed by further dilution with an additional 21 mL 7 M HCl, with the solution placed in an ice bath. Subsequently, this solution was divided to create load solutions for the various resins. A total of five separations were conducted, one with the initial target and four with the subsequent one, enabling a comparative analysis of the separation processes.

#### 4.2.5.2 In-house resin synthesis

In-house covalently bonded hydroxamate resin was synthesized through functionalization of the commercially available Accell$^{TM}$ Plus CM resin. Unsubstituted hydroxamate resin was synthesized using procedure described by J. P. Holland et. al. and the methyl substituted hydroxamate resin was synthesized following procedures described by L. Gajecki et. al. [12], [14].

4.2.5.3 Separation with LN resin and $^{172}Hf/^{172}Lu$ generator

To process the first target with lower activity, approximately 900 mg of Eichrom LN resin was packed into a column as a slurry and conditioned with 2 BV of 7 M HCl after being rinsed with 30 mL of MilliQ water at a flow rate of 0.5 mL/min. Subsequently, 50 mL 7 M HCl, dissolved above, was loaded onto the column at the same flow rate using a peristaltic pump. The eluate, comprising approximately 10 mL fractions of the load solution containing stable lutetium and lutetium isotopes, was collected and quantified using HPGe. Following the load solution, the column was rinsed with 7 M HCl (approximately 30 mL) to recover any remaining stable lutetium and lutetium isotopes, with 10 mL fractions collected for analysis using HPGe and ICP-OES. The matrix on the column was then changed to 1 M HCl. The adsorption of $^{172}Hf/^{175}Hf$ onto the resin allowed for the growth of the $^{172}Lu$ daughter and whenever the elution of the generator was necessary, 6-10 mL 7 M HCl was used for eluting $^{172}Lu$.

For the processing of the second target with higher activity using LN resin, a load solution consisting of 20 mL 7 M HCl was prepared and loaded onto a 2 mL LN cartridge. The resin was previously conditioned with 10 mL water followed by 10 mL 7 M HCl at a flow rate of 0.25 mL/min. The prepared load solution was then loaded onto the resin at the same flow rate using a syringe pump. Four fractions, each containing 5 mL of the load solution, were collected and measured on HPGe for lutetium isotopes. Subsequently, the column was washed with a minimum of 20 mL 7 M HCl to recover any residual stable lutetium and lutetium isotopes. The matrix on the column was then changed to 1 M HCl. The adsorption of $^{172}Hf/^{175}Hf$ onto the resin allowed for the in-growth of the $^{172}Lu$ daughter. Elution cycles for the LN resin involved the use of 10 mL 7 M HCl for nine cycles to analyze for $^{172}Hf$ breakthrough, with 2 mL eluate fractions collected at a flow rate of 0.25 mL/min.

4.2.5.4 Separation with ZR resin and $^{172}$Hf/$^{172}$Lu generator

To process a fraction of the second target (of higher activity), a load solution comprising 20 mL 7 M HCl was prepared for loading onto a 2 mL ZR resin cartridge. Prior to loading, the cartridge underwent preconditioning with 10 mL of water followed by 10 mL 7 M HCl, both carried out at a flow rate of 0.25 mL/min. The prepared solution was then loaded onto the resin at the same flow rate using a syringe pump. Following this, four fractions, each containing 5 mL of the load solution, were collected and measured on HPGe for the presence of lutetium isotopes. The column was then washed with 25 mL of 7 M HCl to recover any residual stable lutetium and lutetium isotopes. As with the previous resins, the matrix of the resin was changed to 1 M HCl and the daughter $^{172}$Lu was allowed to grow in from the adsorption of $^{172}$Hf/$^{175}$Hf onto the resin. Regarding the elution cycles, the $^{172}$Lu daughter was eluted cyclically using 10 mL of 0.1 M HCl to analyze for breakthrough of $^{172}$Hf. Within each cycle, 2 mL eluate fractions were collected at a flow rate of 0.25 mL/min.

4.2.5.5 Separation with in-house synthesized hydroxamate resin and $^{172}$Hf/$^{172}$Lu generator

Around 682 mg of hydroxamate resin, synthesized in-house, was packed into a column (9 mm outer diameter, 6 mm inner diameter, and a length of 15 cm). Following this, the resin was rinsed with 10 mL MilliQ water and conditioned with 10 mL of 7 M HCl. Subsequently, the 14 mL 7 M HCl load solution was passed over the pre-conditioned hydroxamate resin-packed column which is when the majority of lutetium and lutetium isotopes passed through the column and collected in 3.5 mL fractions. To ensure the removal of any remaining lutetium, a rinse step with 14 mL 7 M HCl, distributed in 3.5 mL fractions, was done. This was followed by changing the matrix to 1 M HCl. $^{172}$Hf/$^{175}$Hf adsorbed onto the resin and was followed by the in-growth of

the $^{172}$Lu daughter. Throughout the conditioning and separation processes, the flow rate remained constant at 0.25 mL/min.

Regarding elution cycles, the $^{172}$Lu daughter was eluted cyclically using 10 mL of 0.1 M HCl for nine cycles to check for breakthrough of $^{172}$Hf. Within each cycle, 2 mL eluate fractions were collected at a flow rate of 0.25 mL/min and subsequently analyzed on the HPGe detector.

4.2.5.6 Separation with in-house synthesized methyl-substituted hydroxamate resin and $^{172}$Hf/$^{172}$Lu generator

Approximately 680 mg of methyl-substituted hydroxamate resin, synthesized in-house, was utilized for slurry packing into a column with the same dimensions as the previous one. The rinsing and preconditioning was also done in the same way as the hydroxamate resin at the same constant flow rate 0.25 mL/min.

The loading step was also the same as the hydroxamate and $^{172}$Hf/$^{175}$Hf was left adsorbed onto the resin which allowed for the in-growth of the $^{172}$Lu daughter after changing the matrix of the column to 1 M HCl. Similar to the hydroxamate resin, the $^{172}$Lu daughter underwent cyclic elution with 10 mL of 0.1 M HCl for nine cycles to check for breakthrough of $^{172}$Hf. Within each cycle, 2 mL eluate fractions were collected at a flow rate of 0.25 mL/min and subsequently analyzed with the HPGe detector.

4.2.5.7 Regeneration of $^{172}$Hf/$^{172}$Lu generators using QMA resin

To initiate the regeneration of the generators, the initial step involved stripping hafnium from the various resins. In all established generator setups, hafnium was stripped by elution with 10 mL of 0.5 M Oxalic acid at a flow rate of 0.3 mL/min, with fractions being collected for subsequent analysis using the HPGe detector (result in **Figure B.2** for target 1).

Following the elution of $^{172}Hf/^{175}Hf$, fractions from the four generators were combined, resulting in a total volume of 40 mL. For the hafnium-oxalic acid cleanup process, QMA resin was selected. Two QMA resin cartridges underwent conditioning with 6 mL acetonitrile, followed by 10 mL water and 10 mL 0.5 M Oxalic acid at a flow rate of 1 mL/min. Following that, the 20 mL load solution was passed through each of the two QMA columns at a flow rate of 0.25 mL/min. To ensure the complete removal of oxalic acid, 25 mL of MilliQ water was then passed through the cartridge at 0.25 mL/min. The hafnium retained on the cartridge was subsequently eluted with 10 mL of 1 M HCl at a flow rate of 0.25 mL/min.

4.2.5.8 Establishment of new higher activity ZR-resin generator

After the elution of hafnium from the QMA resin using 1 M HCl, ZR resin was utilized for the establishment of a new generator setup. This resin underwent conditioning with 10 mL of MilliQ water, followed by 10 mL of 1 M HCl, with a flow rate of 1 mL/min for the initial 5 mL and 0.25 mL/min for the subsequent 5 mL of 1 M HCl. The load solution containing $^{172}Hf$ in 1 M HCl, previously eluted from the QMA resin, was then passed through the resin at a flow rate of 0.25 mL/min. When necessary, the generator was eluted with 0.1 M HCl for the extraction of $^{172}Lu$.

4.2.6 Quantification of stable elements with ICP-OES

For the purpose of measuring using ICP-OES, aliquots were withdrawn from each fraction collected during the inactive separations and two dilutions of identical concentrations were prepared for each fraction by diluting them in 2% $HNO_3$. These diluted samples were then quantified and analyzed using Agilent ICP software.

The separation efficiency was determined as a percentage of the loaded amount for lutetium. Calibration curves for sample analysis were established using single-element lutetium

standards at various dilutions ranging from 0.01-1 ppm. The emission lines exhibiting the highest intensity for lutetium were selected for analysis; as shown in the Appendix for the specific wavelengths chosen.

### 4.3 Results and discussion

4.3.1 Radionuclide identification and quantification

The SRIM simulation package was utilized to perform the energy propagation calculations as the proton beam traversed through various components including aluminum, beryllium, stainless steel, AlBeMet alloy, and a water gap within the target array. This is demonstrated in **Figure 4.4** and **Figure 4.5**.

| | | | | thickness | | | | | |
|---|---|---|---|---|---|---|---|---|---|
| layer number | Layer | Material | density | inches | mm | Ei | Eout | E deposited, MeV | Total power, W |
| 1 | Be window | Berillium | 1.85 | 0.012 | 0.305 | 66.00 | 65.54 | 0.46 | 25.09 |
| 2 | AlBeMet window | AlBeMet | 2.10 | 0.012 | 0.305 | 65.54 | 65.01 | 0.53 | 28.67 |
| 3 | Beamline window | stainless steel | 7.99 | 0.031 | 0.787 | 65.01 | 60.57 | 4.44 | 242.13 |
| 4 | water gap | water | 1.00 | 0.106 | 2.692 | 60.57 | 57.62 | 2.95 | 160.65 |
| 5 | BOX front window | stainless steel | 7.99 | 0.508 | 12.903 | 57.62 | 54.48 | 3.14 | 171.23 |
| 6 | water gap | water | 1.00 | 0.100 | 2.54 | 54.48 | 51.44 | 3.04 | 165.51 |
| 7 | Aluminum degrader | Aluminum | 7.99 | 0.056 | 1.42 | 51.44 | 47.72 | 3.71 | 202.28 |
| 8 | water gap | water | 1.00 | 0.200 | 5.08 | 47.72 | 40.74 | 6.98 | 380.43 |
| 9 | Bolted target window | Aluminum | 2.70 | 0.020 | 0.508 | 40.74 | 39.17 | 1.57 | 85.38 |
| 10 | Lutetium foil | Lu | 9.70 | 0.010 | 0.254 | 39.17 | 37.34 | 1.84 | 100.08 |
| 11 | Bolted target back wind | Aluminum | 2.70 | 0.170 | 4.32 | 37.34 | 32.55 | 4.79 | 260.68 |
| 12 | Water pocket | water | 1.00 | 0.298 | 7.57 | 32.55 | 20.84 | 11.71 | 637.93 |
| 13 | water gap | water | 1.00 | 0.100 | 2.54 | 20.84 | 16.56 | 4.28 | 233.06 |
| 14 | Aluminum degrader | Aluminum | 2.70 | 1.736 | 44.10 | 16.56 | stop | 16.56 | 902.32 |
| 15 | water gap | water | 1.00 | 0.100 | 2.54 | 0.00 | 0.00 | 0.00 | 0.00 |
| 16 | Aluminum degrader | Aluminum | 2.70 | 0.056 | 1.42 | 0.00 | 0.00 | 0.00 | 0.00 |
| 17 | water gap | water | 1.00 | 0.000 | 0 | 0.00 | 0.00 | 0.00 | 0.00 |

**Figure 4.4:** Irradiation of Lu foil with an energy of 66 MeV at BLIP (SRIM package was used for the proton beam traversing through several components in the target array and energy propagation calculations are shown). Image provided by Dr. Dmitri Medvedev.

| Layer Number | Layer | Material | Density | Thickness | | MeV | | Energy deposited |
|---|---|---|---|---|---|---|---|---|
| | | | | inch | mm | Ei | Eout | |
| layer number | Layer | Material | density | inches | mm | Ei | Eout | dE, MeV | Power, W |
| 1 | Be window | Berillium | 1.85 | 0.012 | 0.305 | 117.00 | 116.70 | 0.30 | 0.89 |
| 2 | AlBeMet window | AlBeMet | 2.10 | 0.012 | 0.305 | 116.70 | 116.36 | 0.34 | 1.02 |
| 3 | Beamline window | stainless steel | 7.99 | 0.031 | 0.787 | 116.36 | 113.51 | 2.86 | 8.57 |
| 4 | water gap | water | 1.00 | 0.106 | 2.692 | 113.51 | 111.70 | 1.81 | 5.42 |
| 5 | BOX front window | stainless steel | 7.99 | 0.020 | 0.508 | 111.70 | 109.79 | 1.91 | 5.73 |
| 6 | water gap | water | 1.00 | 0.200 | 5.08 | 109.79 | 106.26 | 3.53 | 10.59 |
| 7 | Aluminum degrader | Aluminum | 2.70 | 0.670 | 17.02 | 106.26 | 78.70 | 27.55 | 82.66 |
| 8 | water gap | water | 1.00 | 0.200 | 5.08 | 78.70 | 74.13 | 4.58 | 13.73 |
| 9 | Aluminum degrader | Aluminum | 2.70 | 0.524 | 13.31 | 74.13 | 44.08 | 30.05 | 90.15 |
| 10 | water gap | water | 1.00 | 0.200 | 5.08 | 44.08 | 36.57 | 7.50 | 22.51 |
| 11 | Bolted target window | Aluminum | 2.70 | 0.020 | 0.508 | 36.57 | 34.86 | 1.71 | 5.13 |
| 12 | Lutetium foil | Lu | 9.70 | 0.010 | 0.254 | 34.86 | 32.86 | 2.01 | 6.02 |
| 13 | Copper foil | Cu | 8.96 | 0.002 | 0.051 | 32.86 | 32.36 | 0.50 | 1.50 |
| 14 | Aluminum foil | Al | 2.70 | 0.002 | 0.051 | 32.36 | 32.17 | 0.19 | 0.56 |
| 15 | Nickel foil | Ni | 8.91 | 0.002 | 0.051 | 32.17 | 31.63 | 0.54 | 1.61 |
| 16 | Bolted target back window | Aluminum | 1.00 | 0.164 | 4.166 | 31.63 | 26.07 | 5.56 | 16.69 |
| 17 | Water pocket | water | 1.00 | 0.298 | 7.57 | 31.63 | 31.26 | 0.38 | 1.13 |
| 18 | water gap | water | 1.00 | 0.100 | 2.54 | 31.26 | 28.91 | 2.35 | 7.04 |
| 19 | Aluminum degrader | Aluminum | 2.70 | 0.420 | 10.67 | 28.91 | 27.68 | 28.91 | 86.72 |
| 20 | water gap | water | 1.00 | 0.200 | 5.08 | 0.00 | 0.00 | 0.00 | 0.00 |

**Figure 4.5:** Irradiation of Lu foil with an energy of 117 MeV at BLIP (SRIM package was used for the proton beam traversing through several components in the target array and energy propagation calculations are shown). Image provided by Dr. Dmitri Medvedev.

For the first target, the proton beam enters the lutetium foil target with an initial energy of 22.5 MeV after passing through the preceding components. Upon exiting the foil, the beam energy was measured at 18.7 MeV. The discrepancy with the SRIM simulation is due to the fact that one of the water layers was actually 4.5 mm larger than the design documentation states. This propagates into a large difference in beam energy. Monitor foils for the second irradiation were used to correct for this. This correction resulted in a better and closer energy impinging on the second target where the specific energy of the proton beam upon entering is 35.2 MeV and exiting the lutetium foil target is 32.5 MeV.

To investigate the co-production of radioisotopes resulting from proton irradiation of natural lutetium foil at energies of 66 MeV and 117 MeV, γ-spectroscopy was employed which established the presence of various isotopes including $^{171, 172, 173,175}$Hf, as well as $^{171, 172, 173, 174,}$

$^{177}$Lu, and $^{169}$Yb, identifiable by their characteristic gamma lines. **Figure 4.6** shows a gamma spectrum of the second target prior to any attempted chemical separation. Additionally, no activity was detected on the aluminum target body or screws, suggesting that the proton beam was well centered onto the lutetium foil.

The total activity of $^{172}$Hf in the first and second lutetium foil targets, decay corrected to the end of irradiation, was determined to be 0.39 ± 0.02 MBq and 230 ± 13 μCi (8.51 ± 0.48 MBq). This finding is compared with the theoretical yield of 13.2 MBq for the second target, as indicated in **Table 4.1**. Additionally, through the same γ-spectroscopic measurements, the activity of $^{172}$Lu for the second target, decay corrected to the end of irradiation, was measured at 731 ± 269 μCi (27.0 ± 9.9 MBq).

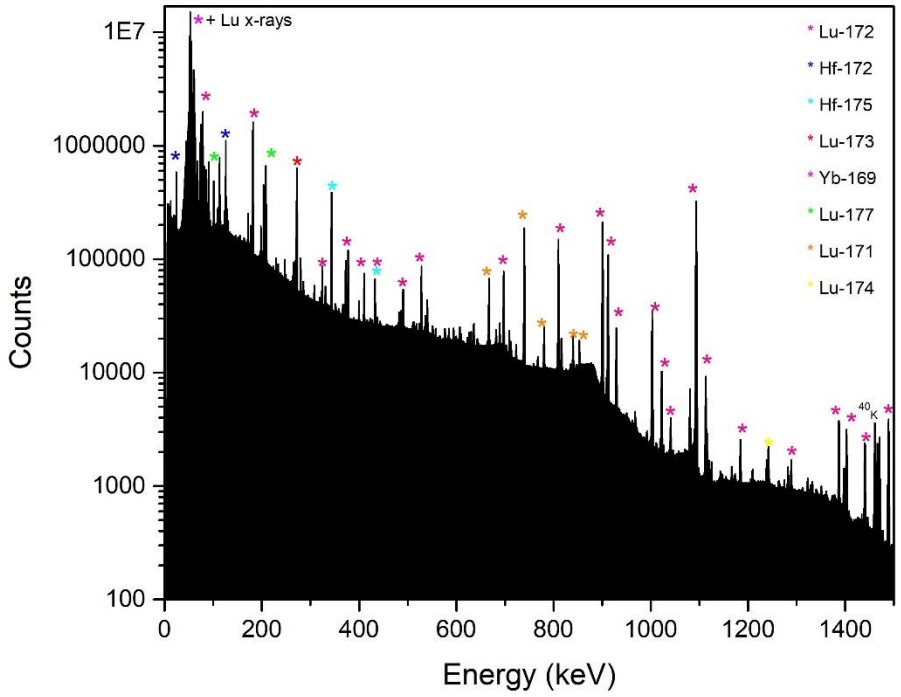


**Figure 4.6**: A gamma spectrum of the second target before chemical separation was attempted is shown.

Table 4.1: The production of different radioisotopes and their theoretical and experimental activity (decay corrected to EOB) is shown resulting from the proton irradiation of natural lutetium foil. The shorter-lived radionuclides are not shown here and given in Table B.1 [2].

| **Radioisotope** | **Half-life** | **Gamma lines (Intensity)** | **Target 2 Experimental activity in μCi (MBq)** | **Target 2 Theoretical activity in μCi (MBq)** |
|---|---|---|---|---|
| $^{172}$Hf | 1.87 y | 125.8 keV (11.3 %), 23.9 keV (20.3 %), 67.4 keV (5.3 %) | 230 ± 13 (8.5 ± 0.5) | 357 ± 0.5 (13.2 ± 0.02) |
| $^{175}$Hf | 70 d | 343.4 keV (84.0 %) | 49.5 ± 1.6 (1.8 ± 0.05) | 88.6 ± 0.9 (3.3 ± 0.03) |
| $^{171}$Lu | 8.2 d | 739.8 keV (48.7 %), 667.4 keV (11.2 %) | 143.5 ± 17.2 (5.3 ± 0.6) | 162.3 ± 12.8 (6.0 ± 0.5) |
| $^{172}$Lu | 6.7 d | 1093.6 keV (63.0 %), 181.5 keV (20.6 %), 900.7 keV (29.8 %) | 731 ± 269 (27.0 ± 9.9) | 285.6 ± 28.7 (10.6 ± 1.1) |
| $^{173}$Lu | 1.37 y | 272.1 keV (21.2 %), 78.6 keV (11.9 %) | 198.8 ± 7.0 (7.4 ± 0.3) | 93.4 ± 0.3 (3.5 ± 0.01) |
| $^{174g}$Lu | 3.31 y | 1241.8 keV (5.1 %), 76.4 keV (5.9 %) | 16.3 ± 12.4 (0.6 ± 0.5) | 27.1 ± 0.5 (1.0 ± 0.01) |
| $^{169}$Yb | 32.0 d | 197.9 keV (35.9 %), 177.2 keV (22.3 %), 63.1 keV (43.6 %) | 17.8 ± 0.6 (0.7 ± 0.02) | 29.3 ± 0.8 (1.1 ± 0.02) |

4.3.2 Dissolution, radiochemical separation, and $^{172}$Hf/$^{172}$Lu generator setups

During the dissolution of the lutetium foil with HCl for both the first and second targets, an observation consistent with the work in Holland et al., when working with irradiated yttrium foils, was noted: the majority of the lutetium foil dissolved, yet a residual trace of black precipitate remained despite repeated attempts at dissolution [12]. This precipitate is presumed to be an insoluble form of lutetium oxide, and it was discovered to contain minimal $^{172}$Hf activity, approximately (~2 μCi).

At the time of the radiochemical separations, which occurred several weeks after EOB for both the first and second targets, the short-lived radioisotopes $^{173}$Hf and $^{171}$Hf had already

decayed, leaving behind $^{172}$Hf, $^{175}$Hf, $^{172}$Lu, $^{173}$Lu, $^{174}$Lu, $^{177}$Lu, and $^{169}$Yb as the radioactive species at the stage of radiochemical separation. For the second target, due to the high activity levels of the collected lutetium fractions, ICP-OES analysis was omitted, and only HPGe was used to track lutetium radioisotopes (and consequently stable lutetium).

4.3.2.1 LN resin separation and $^{172}$Hf/$^{172}$Lu setup

The separation of hafnium from stable lutetium and lutetium isotopes in both the first and second targets utilized di(2-ethylhexyl)orthophosphoric acid (HDEHP) extractant-based LN resin, known for its efficacy with di, tri, and tetravalent metals. In the case of the first target, while stable lutetium and lutetium isotopes passed through the column with the 7 M HCl load solution, hafnium isotopes $^{172}$Hf and $^{175}$Hf were adsorbed onto the resin. Approximately (94.4 ± 2.0)% of stable lutetium was eluted with the load fractions and quantified using ICP-OES. Additional rinsing with 7 M HCl ensured complete removal, resulting in approximately (5.6 ± 0.3)% lutetium elution. Gamma spectrometry was employed to monitor the separation, confirming the absence of hafnium isotopes in the eluate. The $^{172}$Lu daughter was allowed to grow on the column, and the generator was eluted with 7 M HCl when necessary. Despite the low $^{172}$Hf activity, it remained valuable as a research tool, even with minimal total activity for the generator. The gamma spectra for separation with the first target is shown in **Figure 4.7**.

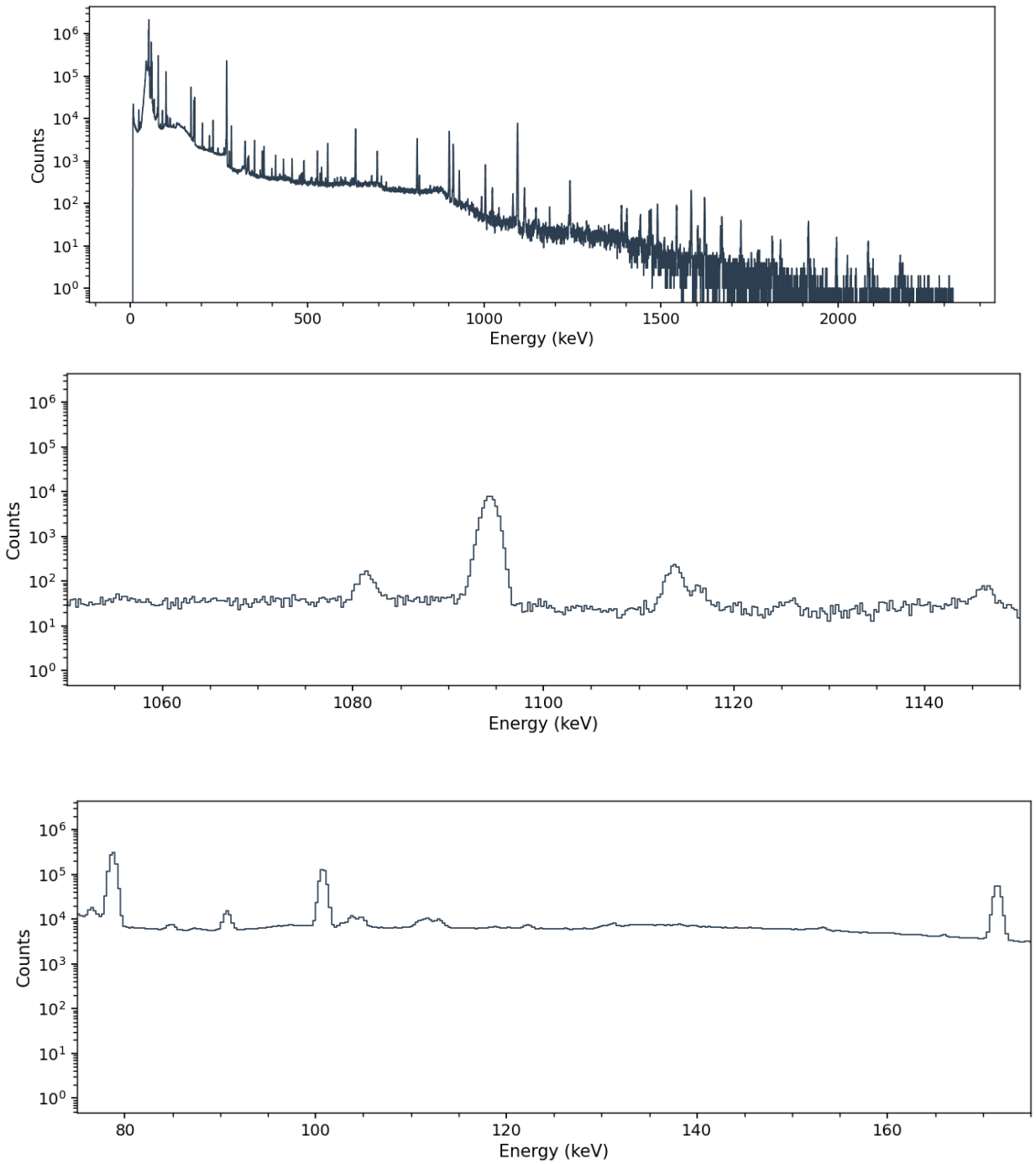


**Figure 4.7:** For the first target, the first spectrum is that obtained from a load solution (7 M HCl) fraction, which is representative of other load solution fractions. The next two spectra are the zoomed-in versions of this main spectrum indicating the presence of the 1093.6 keV peak for $^{172}$Lu and the absence of the 125.8 keV peak for $^{172}$Hf. This indicates a successful separation.

For the second target, which had higher activity, $^{173}$Lu and $^{172}$Lu were utilized to monitor stable lutetium on the HPGe. Approximately (87.3 ± 1.6)% $^{173}$Lu and (90.5 ± 1.7)% $^{172}$Lu were eluted with the load fractions. Further rinsing with 7 M HCl ensured complete removal, resulting in approximately (10.0 ± 0.5)% $^{173}$Lu and (11.6 ± 0.5)% $^{172}$Lu elution. Gamma spectrometry confirmed successful separation, with no hafnium isotopes detected in the eluate. **Figure 4.8 (a)** illustrates the gamma spectrum of the load fractions, demonstrating the absence of hafnium peaks. **Figure 4.8 (b)** depicts the remaining $^{172}$Hf/$^{172}$Lu generator column after the collection of load and wash fractions.

For the elution cycles, **Figure 4.9** displays the gamma spectrum of the LN $^{172}$Hf/$^{172}$Lu generator just before the start of elution for cycle 1, revealing no $^{173}$Lu peak, indicating the absence of stable lutetium remaining on the column. Approximately (85.0 ± 1.0)% of the $^{172}$Lu was captured within three fractions consisting of 2 mL 7 M HCl each, consistently across each cycle, with no observed hafnium breakthrough. **Figure 4.10** illustrates the elution profile for the LN resin generator for cycle 2 and cycle 8 of elution.

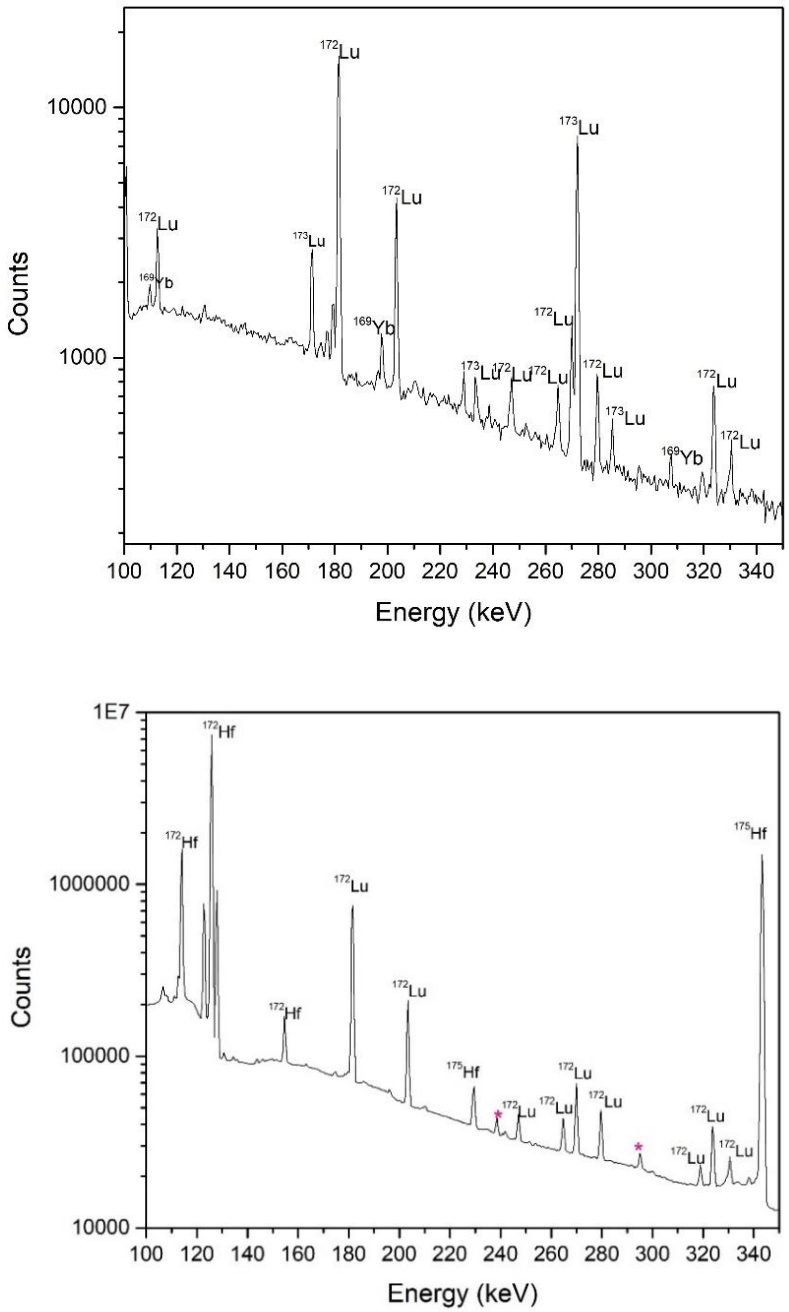


**Figure 4.8:** (a) A gamma spectrum of the load fraction showing the absence of hafnium peaks after separation was attempted with the LN resin for the second target (b) A gamma spectrum of the LN resin column once the separation is carried out and lutetium is allowed to grow in from the hafnium.

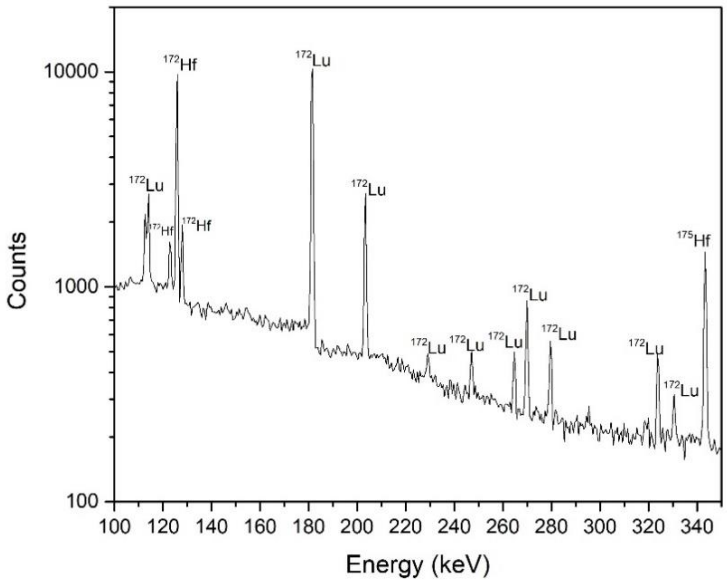


**Figure 4.9:** A gamma spectrum of the $^{172}$Hf/$^{172}$Lu generator just before starting elution for cycle 1 demonstrating no $^{173}$Lu peak (at 272 keV).

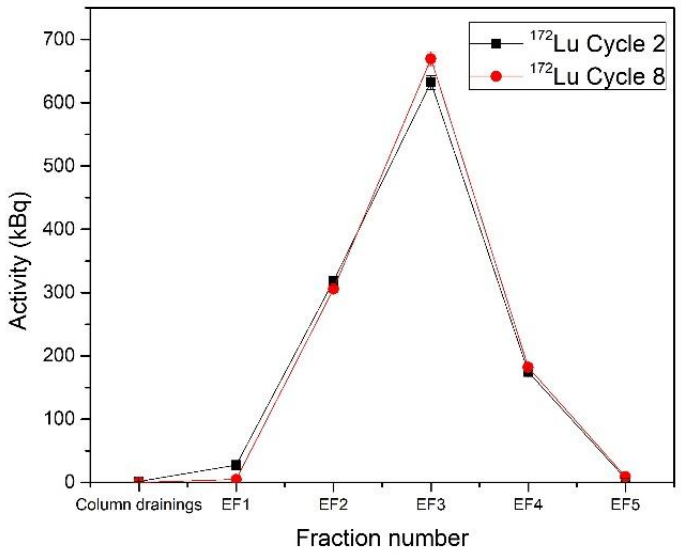


**Figure 4.10:** Elution profile for different cycles of $^{172}$Lu for LN resin is shown.

4.3.2.2 ZR resin separation and $^{172}Hf/^{172}Lu$ setup

The ZR resin, based on hydroxamate extractant, exhibits selectivity for hafnium over lutetium. As a result, approximately (98.0 ± 1.8)% of $^{173}Lu$ and (89.3 ± 4.0)% of $^{172}Lu$ were eluted with the 7 M HCl load fractions and quantified using HPGe detector. To ensure complete removal of stable lutetium and lutetium isotopes, additional rinsing with 7 M HCl was performed, resulting in approximately (7.6 ± 0.4)% $^{173}Lu$ and (8.2 ± 0.4)% $^{172}Lu$ elution. Gamma spectrometry was employed throughout to monitor the separation, confirming the absence of hafnium isotopes in both the load and rinse fractions. At the end of the separation, the matrix was changed to 1 M HCl, and the $^{172}Lu$ daughter was allowed to grow in on the ZR resin column. The generator was eluted with 0.1 M HCl as needed. **Figure 4.11 (a)** illustrates the gamma spectrum of the load fractions from the ZR resin separation, demonstrating the absence of hafnium peaks and indicating successful separation. **Figure 4.11 (b)** depicts the remaining $^{172}Hf/^{172}Lu$ generator column after the collection of load and wash fractions.

Regarding the elution cycles, **Figure 4.12** displays the gamma spectrum of the ZR $^{172}Hf/^{172}Lu$ generator just before the start of elution for cycle 1, revealing no $^{173}Lu$ peak at 272 keV, indicating the absence of stable lutetium remaining on the column. Approximately (95.0 ± 2.2)% of the $^{172}Lu$ was captured within the first fraction consisting of 2 - 4 mL of 0.1 M HCl consistently across each cycle, with no observed hafnium breakthrough until cycle 6. **Figure 4.13** illustrates the elution profile for the ZR resin generator for cycle 2 and cycle 6, which marked the breakthrough cycle.

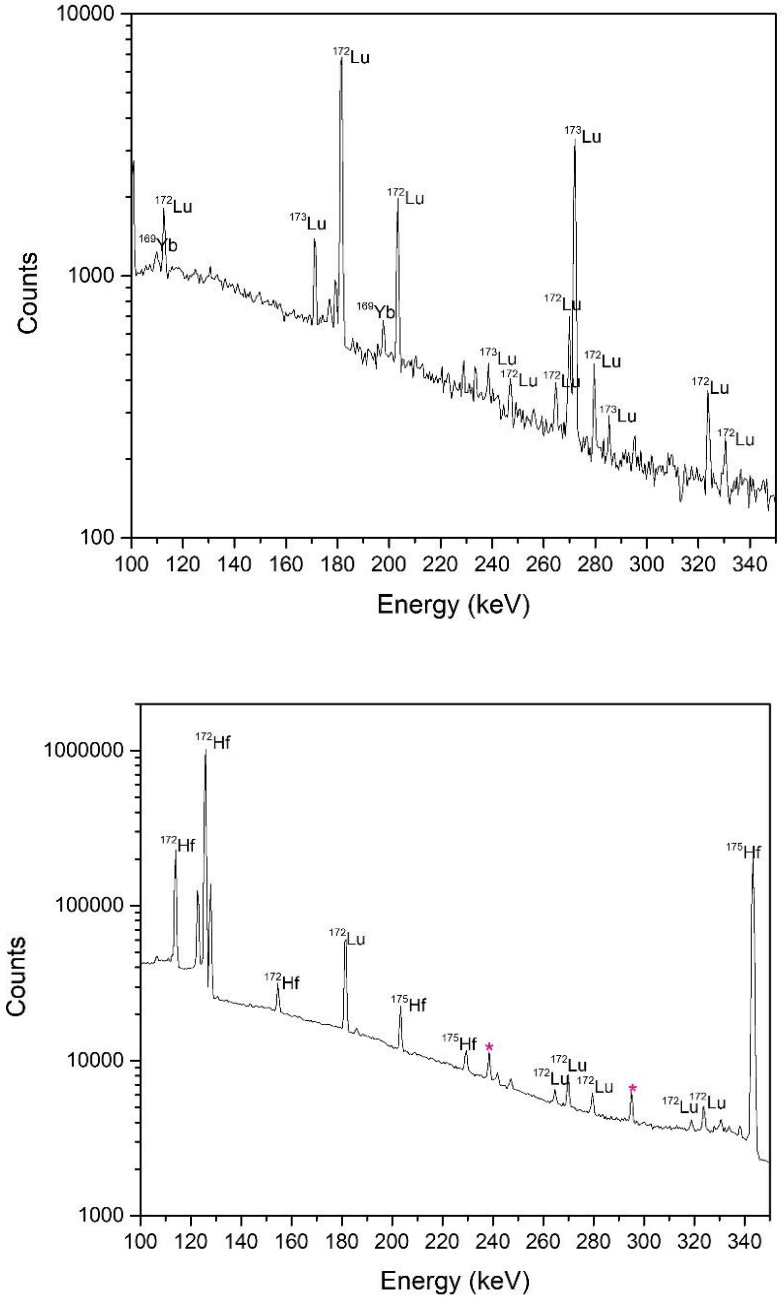


**Figure 4.11:** (a) A gamma spectrum of the load fraction showing the absence of hafnium peaks after separation was attempted with the ZR resin for the second target (b) A gamma spectrum of the ZR resin column once the separation is carried out and lutetium is allowed to grow in from the hafnium.

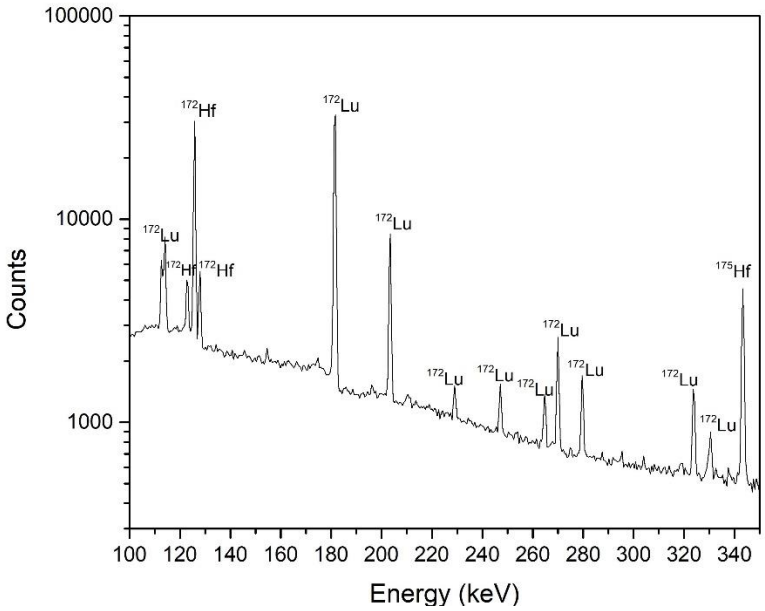


**Figure 4.12:** A gamma spectrum of the ZR $^{172}$Hf/$^{172}$Lu generator just before starting elution for cycle 1 demonstrating no $^{173}$Lu peak (at 272 keV).

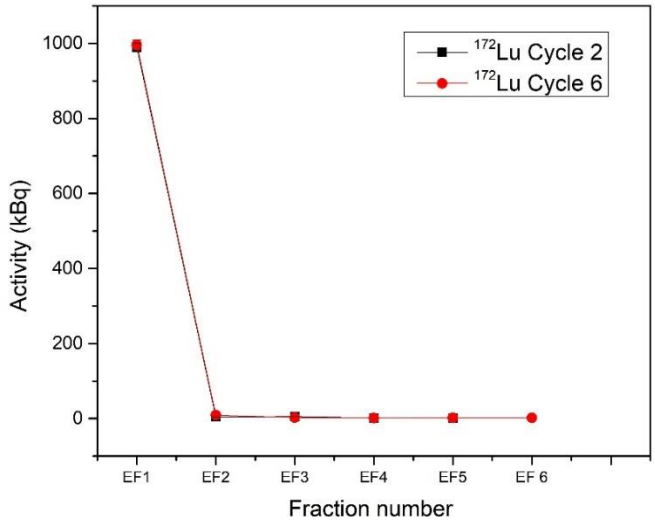


**Figure 4.13:** Elution profile for different cycles of $^{172}$Lu for ZR resin is shown.

4.3.2.3 In-house synthesized hydroxamate resin and methyl-substituted hydroxamate resin separation and $^{172}Hf/^{172}Lu$ setup

The two in-house synthesized hydroxamates underwent identical processing procedures. Upon elution with 7 M HCl, (40.9 ± 1.3)% $^{173}Lu$ and (49.8 ± 1.2)% $^{172}Lu$ were eluted from the hydroxamate resin, while (41.0 ± 1.0)% $^{173}Lu$ and (50.7 ± 0.8)% $^{172}Lu$ were eluted from the methyl-substituted hydroxamate resin. Additional rinsing with 7 M HCl was carried out to ensure the complete removal of stable lutetium and its isotopes, resulting in (53.3 ± 1.7)% $^{173}Lu$ and (52.4 ± 1.4)% $^{172}Lu$ elution from the hydroxamate resin, and (31.5 ± 1.3)% $^{173}Lu$ and (38.6 ± 1.0)% $^{172}Lu$ elution from the methyl-substituted hydroxamate resin.

Throughout the separation process, gamma spectrometry was employed to monitor the separation, indicating the absence of hafnium isotopes in both the load and rinse fractions. The elution matrix was switched to 1 M HCl towards the end of the separation, and $^{172}Lu$ daughter was allowed to grow in on the hydroxamate resin columns. The generator was then eluted with 0.1 M HCl in successive elution cycles. **Figure 4.14 (a)** shows the gamma spectrum of the load fractions from the hydroxamate resin separation, the absence of hafnium peaks shows a successful separation. **Figure 4.17 (a)** shows the same for the methyl-substituted hydroxamate resin. **Figure 4.14 (b)** shows the $^{172}Hf/^{172}Lu$ hydroxamate generator that was eluted with 0.1 M HCl. **Figure 4.17 (b)** shows the methyl-substituted $^{172}Hf/^{172}Lu$ hydroxamate generator that was eluted with 0.1 M HCl.

**Figure 4.15** shows the gamma spectrum of the hydroxamate $^{172}Hf/^{172}Lu$ generator just before starting elution for cycle 1 demonstrating no $^{173}Lu$ peak (at 272 keV), indicating that no stable lutetium remains on the column. **Figure 4.18** shows the same for methyl-substituted hydroxamate generator. Additionally, the elution cycles were done, with (88.0 ± 2.1)% $^{172}Lu$

elution within the first two fractions for the hydroxamate resin in cycle 2. The elution profiles for subsequent cycles were consistent, with no observed hafnium breakthrough. Similar results were obtained for the methyl-substituted hydroxamate resin with (93.2 ± 1.3)% $^{172}$Lu elution for cycle

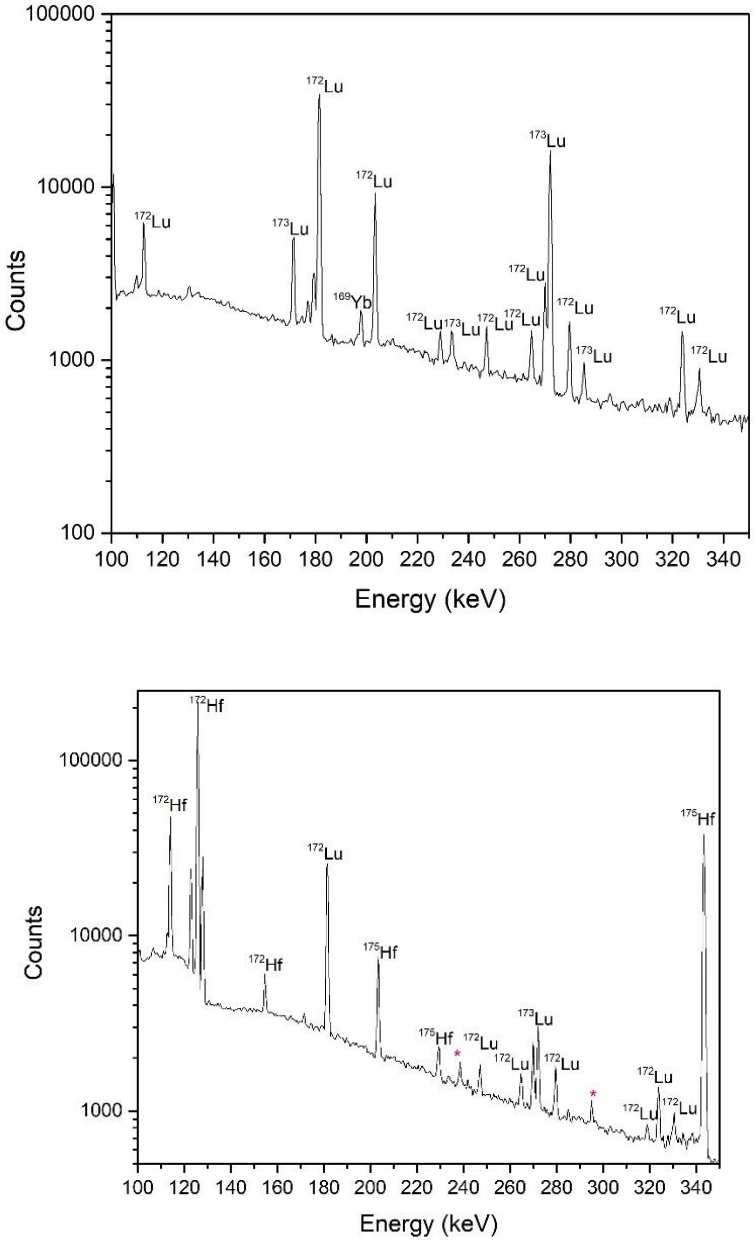


**Figure 4.14:** (a) A gamma spectrum of the load fraction showing the absence of hafnium peaks after separation was attempted with the hydroxamate resin for the second target (b) A gamma spectrum of the hydroxamate resin column once the separation is carried out and lutetium is allowed to grow in from the hafnium.

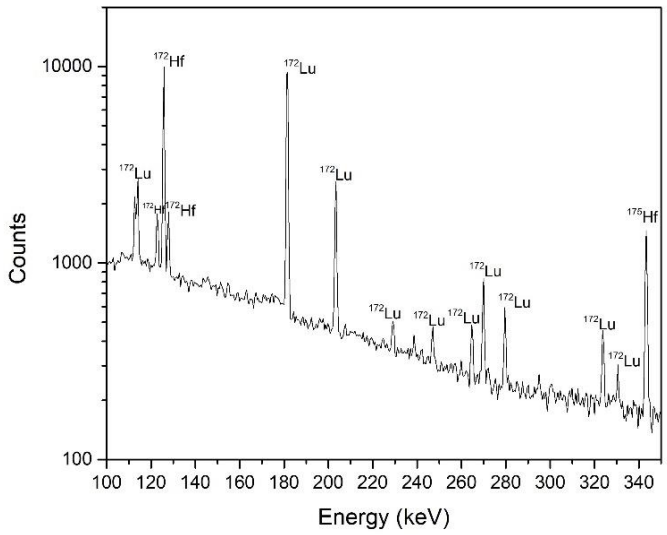


**Figure 4.15:** A gamma spectrum of the hydroxamate $^{172}$Hf/$^{172}$Lu generator before beginning elution during cycle 1 demonstrating no $^{173}$Lu peak (at 272 keV).

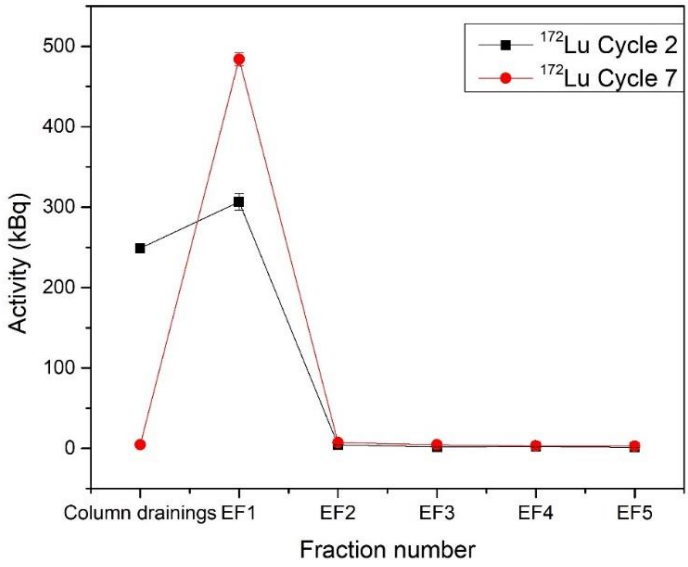


**Figure 4.16:** Elution profile for different cycles of $^{172}$Lu for hydroxamate resin is shown.

**Figure 4.16** shows the elution profile for the hydroxamate resin generator for cycles 2 and 7, and **Figure 4.19** shows the elution profile for the methyl-substituted hydroxamate resin

generator for cycles 2 and 8. **Figure 4.20** summarizes the radiochemical separation scheme for the four resins.

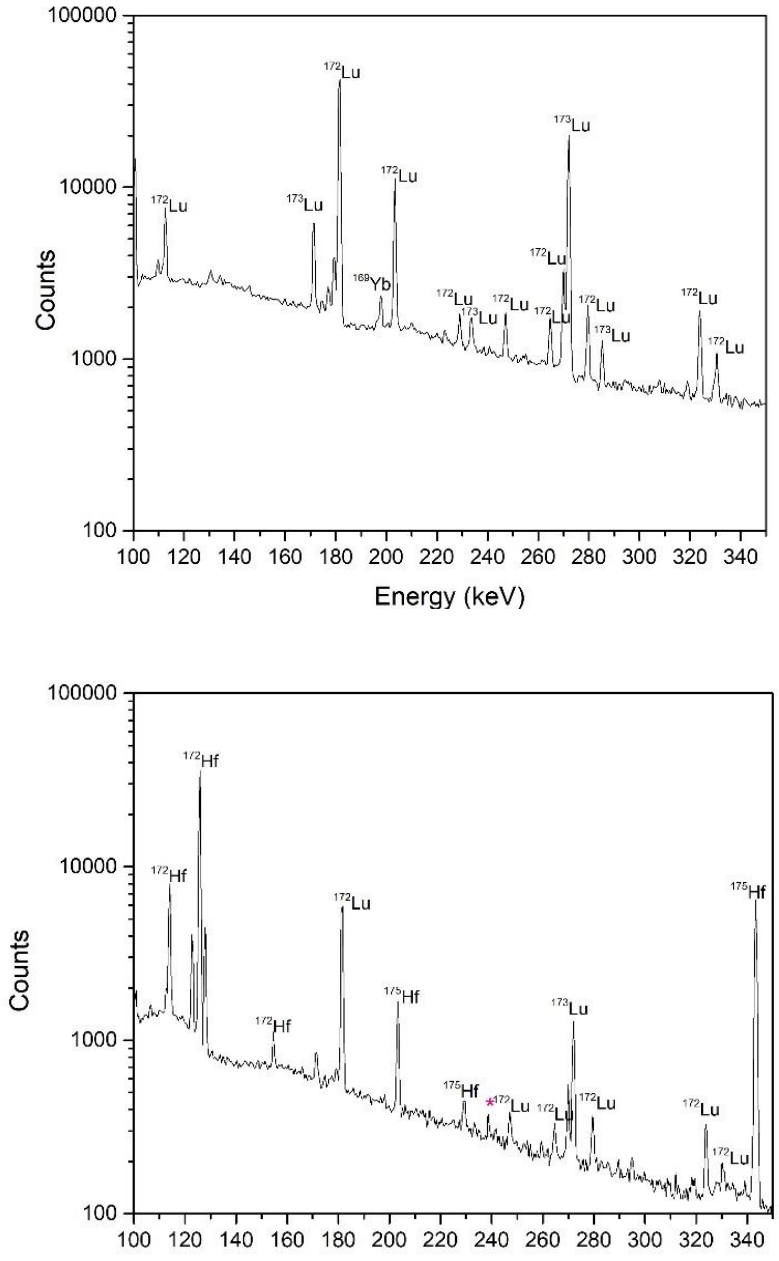


**Figure 4.17:** (a) A gamma spectrum of the load fraction showing the absence of hafnium peaks after separation was attempted with the methyl-substituted hydroxamate resin for the second target (b) A gamma spectrum of the methyl-substituted hydroxamate resin column once the separation is carried out and lutetium is allowed to grow in from the hafnium.

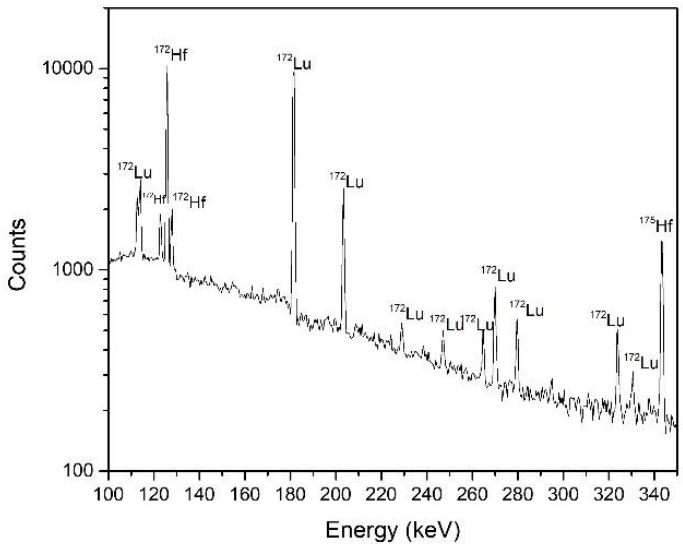


**Figure 4.18:** A gamma spectrum of the methyl-substituted hydroxamate $^{172}$Hf/$^{172}$Lu generator before beginning elution during cycle 1 demonstrating no $^{173}$Lu peak (at 272 keV).

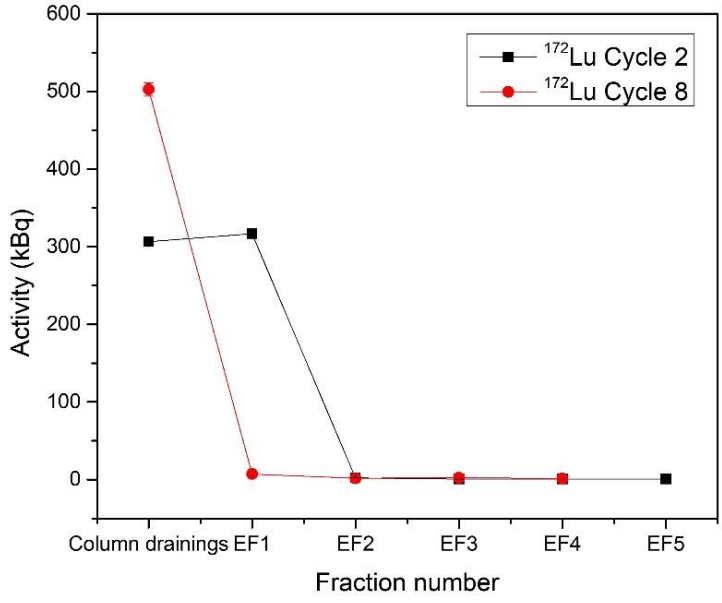


**Figure 4.19:** Elution profile for cycles 2 and 8 of $^{172}$Lu for methyl-substituted hydroxamate resin is shown.

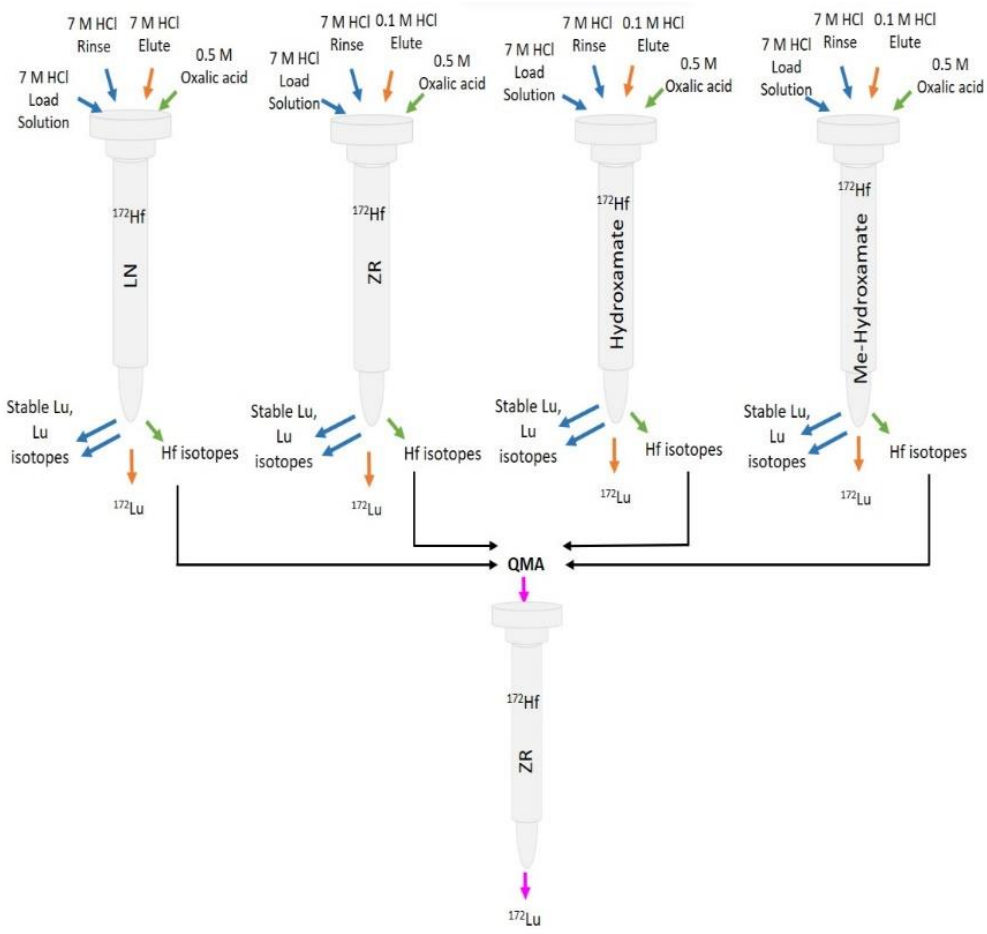


**Figure 4.20:** A schematic showing the sequence (from left to right) of the radiochemical separation on LN resin, ZR resin, hydroxamate, and methyl-substituted resin packed column.

4.3.2.5 - Comparison, and regeneration of $^{172}$Hf/$^{172}$Lu generators using ZR resin

For all the generators set up above the $^{172}$Lu eluted activity is more than sufficient to carry out PAC experiments which typically need only a few hundred kBq for a study and to test radiolabeling parameters for development of new tracers. One disadvantage of LN resin in this regard is the elution of $^{172}$Lu in higher molarity HCl which requires an added step of dilution or evaporation and reconstitution in lower molarity HCl to use it for an application like radiolabeling. Some comparative features are listed in **Table 4.2**.

After passing the Hf-oxalic acid solution through QMA resin, and obtaining the Hf in HCl matrix, ZR resin was selected out of the four generators to be made into a short-term, high activity generator. Unlike LN resin having to use high molarity HCl to elute $^{172}$Lu, ZR resin eluted $^{172}$Lu in 0.1 M HCl, which is a more preferable matrix to perform radiolabeling studies without having to dilute to a lower molarity or evaporate to dryness to be reconstituted in another matrix. Compared to the two in-house hydroxamate based synthesized resins, the ZR resin was selected as a 2 mL cartridge that can be readily purchased making preparations of a generator routine. Following construction of the high activity generator, the elution volume was reduced to 2.1 mL 0.1 M HCl as a majority of the $^{172}$Lu is eluted in the first fraction as shown for the hydroxamate based resins. Specific activity was performed using a modified method from Holland et. al following the concentration of $^{172}$Lu using an Agilent Bond Elute 1 mL SCX column with a modified method from Domnanich et al. [12], [25]. The specific activity was determined to range from 19 to 51 μCi/nmol. **Figure 4.21** shows the elution profile for cycle 1 for the higher activity ZR $^{172}$Hf/$^{172}$Lu generator.

Table 4.2: A comparison is drawn between the different resins with respect to volume for elution and $^{172}$Hf breakthrough.

| **Feature** | **LN resin** | **ZR resin** | **hydroxamate resin** | **methyl-substituted hydroxamate resin** |
|---|---|---|---|---|
| Volume for eluting generators | Broad elution profile, 6 - 8 mL | First 2 - 4 mL | First 2-4 mL | First 2-4 mL |
| $^{172}$Hf breakthrough | No breakthrough | Cycle 6 of eluting | No breakthrough | No breakthrough |

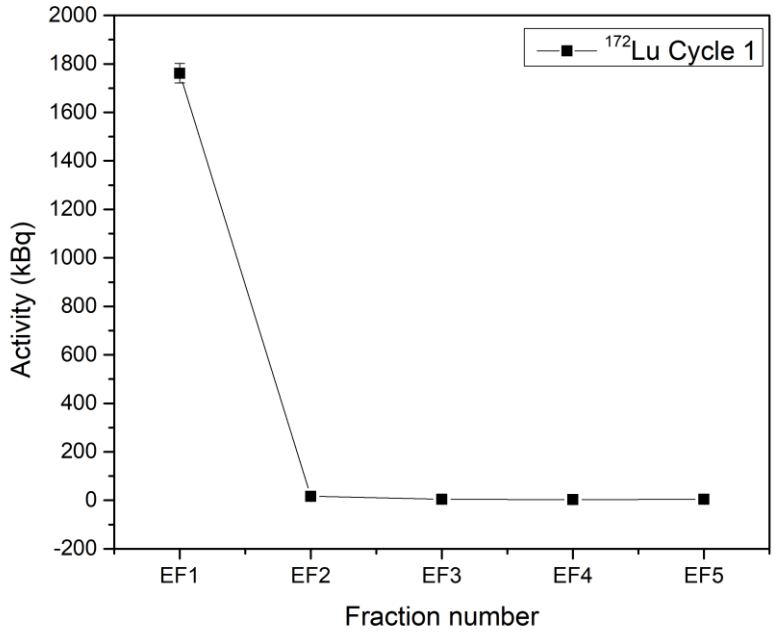


**Figure 4.21:** An elution profile for different cycles of $^{172}$Lu for the higher activity ZR resin is shown.

4.3.2.6 Comparison of these generators with those in Chapter 3

The generators set up in this work exhibit high radiochemical purity as compared to the generator set up from the beam-blocker. The generators set up from the beam-blocker work are

good for PAC studies, but, the generators set up here are good for radiolabeling studies as well, and also provide higher $^{172}$Lu activity in one elution. Nevertheless, the generators from the isotope harvesting technique met the requirements where high purity was not needed.

### 4.4 Conclusion

In this work, radiochemical methodologies were established for the extraction of $^{172}$Hf from stable lutetium and lutetium isotopes in the hydrochloric acid media and four generator systems with commercially available LN, ZR, and in-house synthesized hydroxamate and methyl-substituted hydroxamate were studied. In all cases, the ease of separation, elution, and the long shelf-life of the $^{172}$Hf/$^{172}$Lu generator systems makes it ideal for experiments where pure lutetium isotope is needed and procuring $^{177}$Lu is not always feasible. Generators were compared on parameters like volume for elution and $^{172}$Hf breakthrough. This endeavor of obtaining pure $^{172}$Lu finds abundant applicability in PAC studies, radiolabeling and in Hf-Lu isotope geochemistry studies.

## REFERENCES


[1] J. Strosberg *et al.*, "Phase 3 Trial of 177Lu-Dotatate for Midgut Neuroendocrine Tumors," *New England Journal of Medicine*, vol. 376, no. 2, pp. 125–135, Jan. 2017, doi: 10.1056/nejmoa1607427.

[2] "National Nuclear Data Center." Accessed: Mar. 22, 2024. [Online]. Available: https://www.nndc.bnl.gov/nudat3/

[3] A. Hermanne, S. Takacs, M. B. Goldberg, E. Lavie, Y. N. Shubin, and S. Kovalev, "Deuteron-induced reactions on Yb: Measured cross sections and rationale for production pathways of carrier-free, medically relevant radionuclides," *Nucl Instrum Methods Phys Res B*, vol. 247, no. 2, pp. 223–231, Jun. 2006, doi: 10.1016/j.nimb.2006.03.008.

[4] F. Tárkányi *et al.*, "Activation cross sections of proton induced nuclear reactions on ytterbium up to 70 MeV," *Nucl Instrum Methods Phys Res B*, vol. 267, no. 17, pp. 2789–2801, Sep. 2009, doi: 10.1016/j.nimb.2009.05.075.

[5] S. Santos, S. De Barros, and J. C. Suita, "Cross sections and thermonuclear reaction rates for 181Ta(a,n)185Re, 169Tm(a,n)172Lu, 191Ir(a,n)194Au and 197Au(a,n)200Tl," *J. Phys. G: Nucl. Part. Phys*, vol. 26, pp. 301–308, 2000.

[6] S. K. Das, A. G. C. Nair, R. K. Chatterjee, R. Guin, and S. K. Saha, "The performance of a new 172Hf-172Lu generator," *Applied Radiation and Isotopes*, vol. 47, no. 7, pp. 643–644, 1996, doi: https://doi.org/10.1016/0969-8043(96)00025-5.

[7] P. M. Grant, G. E. Montero, A. M. Newman, and H. A. O'Brien, "First use of millicurie levels of172Hf−172Lu in the industrial sector," *J Radioanal Nucl Chem*, vol. 96, no. 6, pp. 629–633, 1985, doi: 10.1007/BF02165043.

[8] T. Venkova *et al.*, "Pseudo-spin band in the odd-odd nucleus 172Lu," *Eur Phys J A Hadron Nucl*, vol. 18, no. 1, pp. 1–4, 2003, doi: 10.1140/epja/i2003-10024-4.

[9] R. J. Daniels, P. M. Grant, and H. A. O'Brien, "The production, recovery, and purification of 172Hf for utilization in nuclear medicine as the generator of 172Lu," *Int J Nucl Med Biol*, vol. 5, no. 1, pp. 11–17, 1978, doi: 10.1016/0047-0740(78)90085-2.

[10] P. M. Grant, R. J. Daniels, W. J. Daniels, G. E. Bentley, and H. A. O' Brien, "The generator production of 172Lu from 172Hf for limited nuclear medicine research," 1983.

[11] J. A. Dadakhanov *et al.*, "172Hf → 172Lu Radionuclide Generator Based on a Reverse-Tandem Separation Scheme," *Radiochemistry*, vol. 60, no. 4, pp. 415–426, Jul. 2018, doi: 10.1134/S1066362218040112.

[12] J. P. Holland, Y. Sheh, and J. S. Lewis, "Standardized methods for the production of high specific-activity zirconium-89," *Nucl Med Biol*, vol. 36, no. 7, pp. 729–739, Oct. 2009, doi: 10.1016/j.nucmedbio.2009.05.007.

[13] W. E. Meijs *et al.*, “Production of highly pure no-carrier added 89Zr for the labelling of antibodies with a positron emitter,” *Applied Radiation and Isotopes*, vol. 45, no. 12, pp. 1143–1147, 1994, doi: https://doi.org/10.1016/0969-8043(94)90029-9.

[14] L. Gajecki, C. M. Marino, C. S. Cutler, and V. A. Sanders, “Evaluation of hydroxamate-based resins towards a more clinically viable 44Ti/44Sc radionuclide generator,” *Applied Radiation and Isotopes*, vol. 192, Feb. 2023, doi: 10.1016/j.apradiso.2022.110588.

[15] I. Verel, G. W. M. Visser, R. Boellaard, M. S. Walsum, G. B. Snow, and G. A. M. S. van Dongen, “89Zr Immuno-PET: Comprehensive Procedures for the Production of 89Zr-Labeled Monoclonal Antibodies,” *Journal of Nuclear Medicine*, vol. 44, no. 8, p. 1271, Aug. 2003, [Online]. Available: http://jnm.snmjournals.org/content/44/8/1271.abstract

[16] “ZR resin.” Accessed: Mar. 22, 2024. [Online]. Available: https://www.triskem-international.com/scripts/files/61eef0f5e9fa69.45400285/PS_ZR-Resin_EN_210908.pdf

[17] P. Horwitz and D. Mcalister, “Eichrom’s LN Series of Resins: Characterization and Novel Applications,” 2008.

[18] Y. heng Yang, H. fu Zhang, Z. yin Chu, L. wen Xie, and F. yuan Wu, “Combined chemical separation of Lu, Hf, Rb, Sr, Sm and Nd from a single rock digest and precise and accurate isotope determinations of Lu-Hf, Rb-Sr and Sm-Nd isotope systems using Multi-Collector ICP-MS and TIMS,” *Int J Mass Spectrom*, vol. 290, no. 2–3, pp. 120–126, Feb. 2010, doi: 10.1016/j.ijms.2009.12.011.

[19] I. C. Kleinhanns, K. Kreissig, B. S. Kamber, T. Meisel, T. F. Nägler, and J. D. Kramerst, “Combined chemical separation of Lu, Hf, Sm, Nd, and REEs from a single rock digest: Precise and accurate isotope determinations of Lu-Hf and Sm-Nd using multicollector-ICPMS,” *Anal Chem*, vol. 74, no. 1, pp. 67–73, Jan. 2002, doi: 10.1021/ac010705z.

[20] M. Bizzarro, J. A. Baker, and D. Ulfbeck, “A new digestion and chemical separation technique for rapid and highly reproducible determination of Lu/Hf and Hf isotope ratios in geological materials by mc-ICP-MS,” *Geostandards Newsletter*, vol. 27, no. 2, pp. 133–145, Jul. 2003, doi: 10.1111/j.1751-908X.2003.tb00641.x.

[21] J. N. Connelly, “Improved dissolution and chemical separation methods for Lu-Hf garnet chronometry,” *Geochemistry, Geophysics, Geosystems*, vol. 7, no. 4, Apr. 2006, doi: 10.1029/2005GC001082.

[22] B. Le Fèvre and C. Pin, “A straightforward separation scheme for concomitant Lu-Hf and Sm-Nd isotope ratio and isotope dilution analysis,” *Anal Chim Acta*, vol. 543, no. 1–2, pp. 209–221, Jul. 2005, doi: 10.1016/j.aca.2005.04.044.

[23] D. G. Medvedev, L. F. Mausner, G. A. Greene, and A. L. Hanson, “Activation of natural Hf and Ta in relation to the production of 177Lu,” *Applied Radiation and Isotopes*, vol. 66, no. 10, pp. 1300–1306, 2008, doi: https://doi.org/10.1016/j.apradiso.2008.02.090.

[24] J. F. Ziegler, M. D. Ziegler, and J. P. Biersack, “SRIM - The stopping and range of ions in matter (2010),” *Nucl Instrum Methods Phys Res B*, vol. 268, no. 11–12, pp. 1818–1823, Jun. 2010, doi: 10.1016/j.nimb.2010.02.091.

[25] K. A. Domnanich *et al.*, “Production and separation of 43Sc for radiopharmaceutical purposes,” *EJNMMI Radiopharm Chem*, vol. 2, no. 1, p. 14, 2017, doi: 10.1186/s41181-017-0033-9.

# APPENDIX

## $^{172}$Hf PRODUCTION AND $^{172}$Hf/$^{172}$Lu CHEMISTRY DEVELOPMENT

### ICP-OES measurement wavelengths for lutetium and hafnium

For the ICP-OES analysis, the emission lines which had the highest intensity for Lu (261.542, 291.139 nm), and Hf (232.247, 277.336, 264.141 nm) were chosen for analysis.

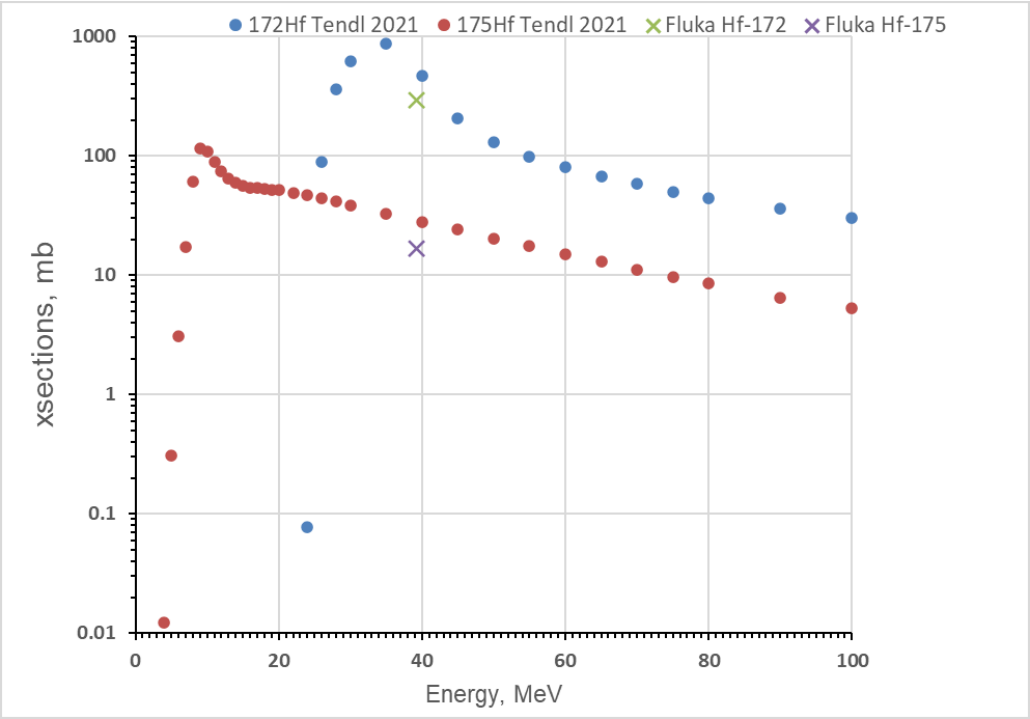


**Figure B.1**: A comparison is shown here between data from TALYS-2019 from Tendl library and FLUKA code values for the production of $^{172}$Hf and $^{175}$Hf when lutetium foil is irradiated with protons. Image provided by Dr. Dmitri Medvedev. FLUKA data generated by Dr. Dohyun Kim.

### Separation chemistry development with stable elements

To develop a procedure for the separation of hafnium from stable lutetium and other radioisotopes, hafnium and lutetium solutions in the HCl medium were prepared using commercially available Hf and Lu ICP-OES standards and from dissolution of Lutetium (III) chloride hexahydrate. The methodology was developed to separate hafnium tracer from 1.5 g

stable lutetium in the hydrochloric acid medium to mimic the radioactive conditions, and loading 50 - 60 mL of 7 M HCl on the LN resin. Separations were performed with the peristaltic pump after calibrating the flow rate and 10 - 13 mL fractions were collected. Aliquots from each fraction was withdrawn and appropriate dilutions in 2% $HNO_3$ were prepared for measurement with ICP-OES. Standards in various dilutions (0.01 ppm - 10 ppm) were used to establish the calibration curves for the sample analysis. The separation efficiency was determined as expressing the total eluted amount in all fractions as a percentage of the loaded amount for each element.

Table B.1: The gamma lines used for tracking the radionuclides not mentioned in the main text [2].

| Radioisotope | Half-life | Gamma lines (Intensity) |
|---|---|---|
| $^{173}$Hf | 23.6 h | 123.7 keV (83.0 %), 296.9 keV (33.9 %), 139.6 keV (12.7 %) |
| $^{174m}$Lu | 142 d | 67.058 keV (7.25), 44.6 keV (12.4 %) |
| $^{177}$Lu | 6.6 d | 208.4 keV (10.4 %), 112.9 keV (6.23 %) |

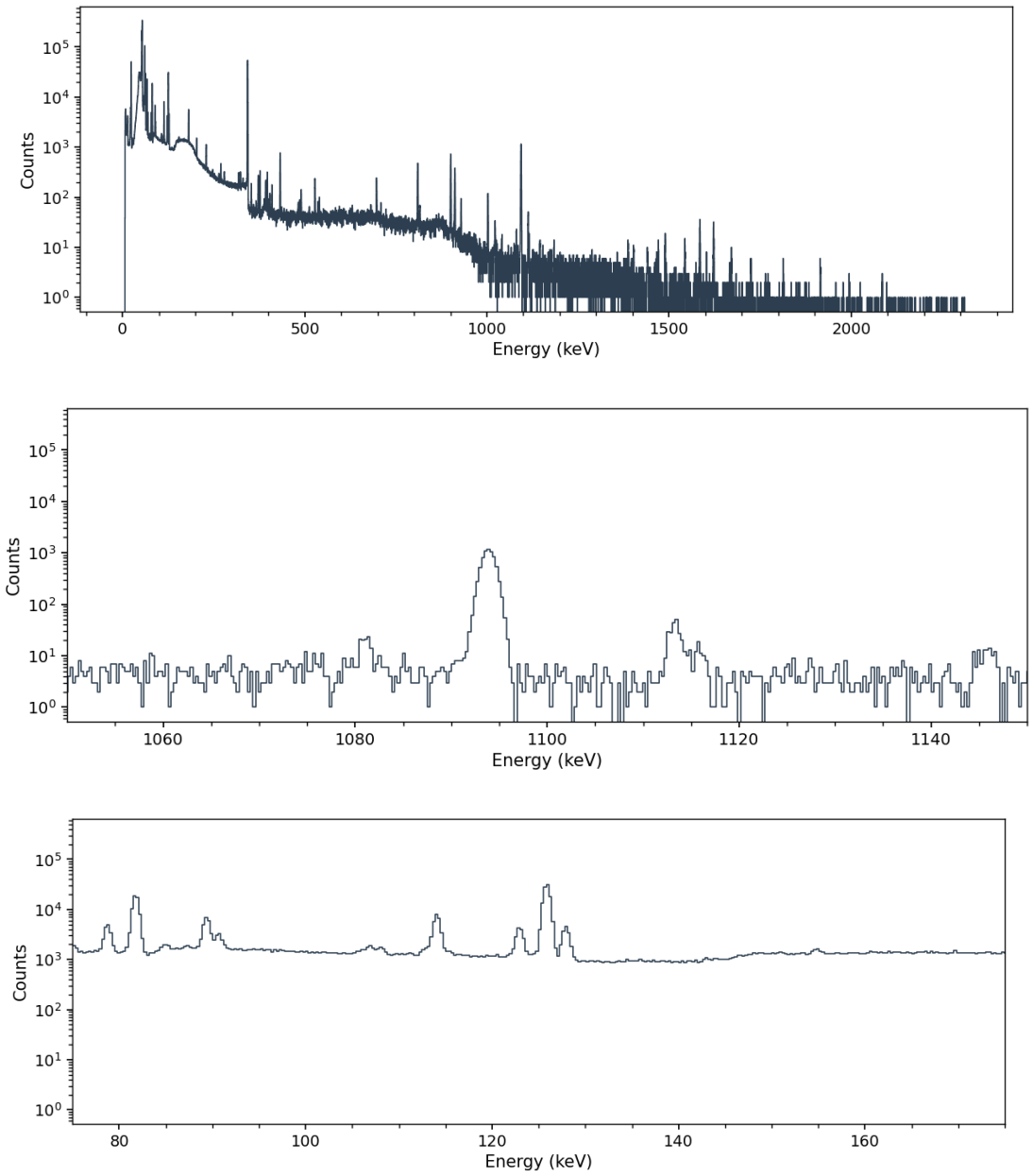


**Figure B.2**: For the first target, the first spectrum is obtained from the elute fraction of 0.5 M Oxalic acid. The next two spectra are the zoomed-in versions of this main spectrum indicating the presence of the 1093.63 keV peak for $^{172}$Lu generated from $^{172}$Hf and the presence of the 125.812 keV peak for the elution of $^{172}$Hf.

# CHAPTER 5: $^{7}$Be HARVESTING: PRODUCTION AND SEPARATION FROM BORON AND BEAM DELIVERY

The cosmogenic radionuclide $^{7}$Be was produced by the irradiation of natural boron and ($^{10}$B) enriched boron pellet targets. Following this, the targets underwent dissolution in nitric acid, after which $^{7}$Be was separated from bulk boron via the macroporous cation-exchange chromatographic resin AG-MP 50. Six such separations were carried out from 7 irradiations and an average recovery rate of (99.4 ± 3.7)% was achieved. Source preparation was then carried out form the isolated $^{7}$Be before being introduced into an ion source at NSCL/FRIB called the Batch-Mode Ion Source. The resulting $^{7}$Be beam was then delivered to end users at the NSCL, maintaining an average delivery rate of 5 x $10^{5}$ particles per second.

## 5.1 Introduction

Numerous proposed experiments conducted in radioactive ion beam facilities necessitate the utilization of radioactive source materials, such as the cosmogenic radionuclide $^{7}$Be. This proton-rich isotope of beryllium possesses a half-life of 53.2 days and emits a distinct gamma-ray with 477.6035(20) keV and an intensity of 10.44(4)% [1]. One notable application of this involves researchers needing $^{7}$Be for investigating the impact of weakly-bound nuclei structures on nuclear fusion reaction outcomes. Additionally, $^{7}$Be beams are of interest in astrophysics to solve the ‘cosmological lithium problem’. The abundance of $^{7}$Be at the time of its production and its subsequent decay rate influence the amount of $^{7}$Li that is ultimately produced during Big Bang Nucleosynthesis (BBN). Therefore, understanding the processes related to $^{7}$Be and its interactions with other nuclei is important for accurately predicting the abundance of $^{7}$Li and addressing the cosmological lithium problem [2].

In order to provide the $^{7}$Be beam to experimenters, a source of $^{7}$Be was required that could be inserted into an offline ion source, at the NSCL/FRIB called the Batch-Mode Ion Source (BMIS) [3]. The ion source facilitates the stand-alone operation of the ReAccelerator (ReA) as well as stopped-beam instrumentation at the NSCL/FRIB [4].

The BMIS consists of a sample oven connected to a VD5 ion source which is the Versatile Arc Discharge Ion Source (VADIS) based on electron impact ionization [5]. In the oven, samples of stable isotopes and radioisotopes with relatively long half-lives can be placed [3], [6]. The samples are then heated and atomized in the oven and effuse into the plasma ion-source, where they get ionized, accelerated and delivered as beams to various user end-stations [3], [6]. The temperature of the oven is adjusted in accordance with the volatility of the introduced compounds. In the BMIS operation, nitrogen trifluoride ($NF_3$) is often used as a reaction gas to create fluorides for lower temperature release of non-volatile substances and to decrease their surface adsorption like for beryllium. **Figure 5.1** shows the location of BMIS in the NSCL building and the BMIS module.

The production of the $^{7}$Be radioisotope commonly involves several methods, including proton irradiation of a lithium target ($^{7}$Li(p,n)$^{7}$Be), followed by chemical separation techniques to isolate $^{7}$Be, as outlined by [7], [8], [9], [10]. Additionally, alternative methods such as photonuclear reactions and sequential charged particle reactions induced by neutron bombardment have been employed for $^{7}$Be production [11], [12]. However, for the specific purpose of generating source material for extracting a radioactive beam, the preferred approach was the production of $^{7}$Be via proton bombardment of a boron target through the $^{10}$B(p,α)$^{7}$Be

nuclear reaction [10], [13]. This method is favored as it eliminates the introduction of $^{7}$Li, which could serve as an isobaric impurity contaminating the delivered beam [13].

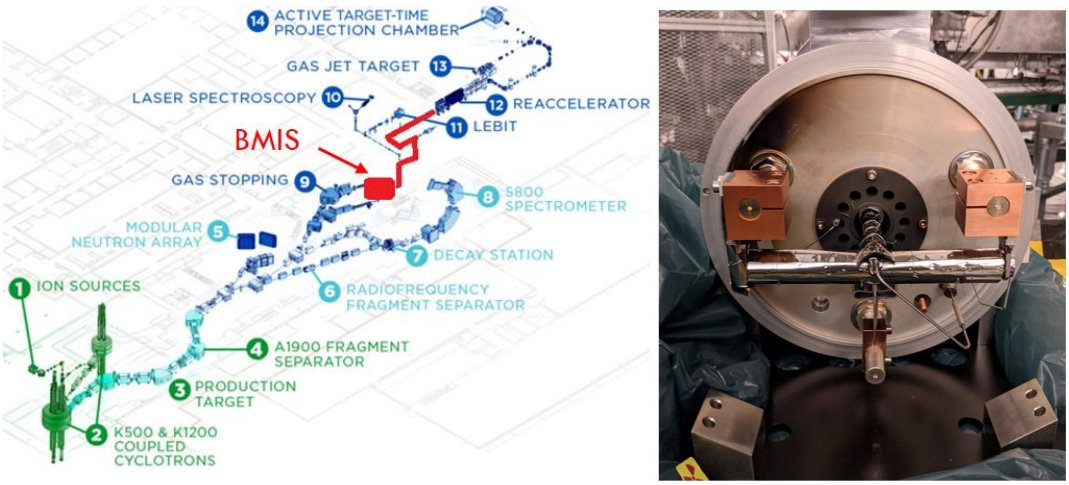


**Figure 5.1**: (Left) A schematic of the NSCL building is shown with the BMIS area highlighted [36] (Right) The BMIS is shown where the oven is the cylinder in the middle [6].

Both the $^{7}$Be isotope and the $^{10}$B(p,α)$^{7}$Be reaction pathway have found application in diverse fields, spanning environmental radiochemistry, nuclear astrophysics encompassing cross-section analyses, plasma physics, boron-related reactions in fusion reactors, and materials science [8], [12], [14], [15], [16], [17], [18], [19], [20], [21], [22], [23], [24], [25], [26], [27]. Despite the extensive investigation into nuclear reactions, there is a noticeable dearth of references addressing the chemical separation of $^{7}$Be from irradiated boron. One potential approach to purify $^{7}$Be from boron involves cation-exchange chromatography in nitric acid media, leveraging favorable distribution coefficients [28]. Consequently, a separation method based on cation-exchange resin was devised for the present study.

This study details the proton irradiation of natural boron (consisting of both $^{11}$B and $^{10}$B isotopes) and $^{10}$B-enriched pellet targets, followed by a chemical separation technique to isolate $^{7}$Be from the boron targets using the macroporous cation-exchange AG-MP 50 resin. Conducted at the radiochemistry facility of the University of Alabama at Birmingham (UAB), this method

purified $^{7}$Be, which was subsequently transferred to MSU. At MSU, appropriate source samples were prepared and transferred into the BMIS. Successful extraction and delivery of $^{7}$Be beams to end users were achieved. Additionally, the study provides insights into the overall yields of production, separation, and BMIS source performance.

## 5.2 Experimental

### 5.2.1 Cyclotron production of $^{7}$Be at UAB

Materials: For the preparation of the boron pellet targets, the materials obtained were natural amorphous boron powder (19.9% $^{10}$B and 80.1% $^{11}$B) from Sigma Aldrich (15580, ≥ 95% boron amorphous powder) and $^{10}$B enriched boron powder from Cambridge Isotopes Laboratories, Inc. ($^{10}$B, 98% chemical purity). The "coin" target holder and proton energy degrader were made of tantalum (tantalum sheet, 3 mm thickness, 3N8 purity, KND6098, ESPI metals) and were cleaned with acetone (Optima$^{TM}$, A929SK-4, Fisher Chemical). The chemical processing was performed with nitric acid ($HNO_3$, 65%, Suprapur) and hydrochloric acid (HCl, 37 wt. % in $H_2O$, 99.99% Trace metals basis, Sigma-Aldrich). MilliQ water (Thermo Scientific MicroPure Ultrapure Water System, 18.2 MΩ cm) was used to prepare all solutions. Other reagents used during the method development stage include Beryllium ICP Standard (1000 ppm, <5% $HNO_3$, GFS Chemicals), Boron ICP Standard (1000 ppm, <5% $HNO_3$, GFS Chemicals), metallic boron foil (3 mm thick, hot pressed, 99.6%, GoodFellow Cambridge Limited), and nitric acid ($HNO_3$, ACS Plus, 15.8 M, Fisher Chemical).

Instruments: The $^{7}$Be was detected and quantified with a Canberra S5000 High-Purity Germanium Detector and the analysis of spectra was performed with Canberra Genie 2000 software. At UAB, an inductively coupled plasma mass spectrometer (ICP-MS) (Agilent Technologies 7800 ICP-MS) and Agilent software, ICP-MS MassHunter v4, was used for

quantifying the amount of stable boron in the collected fractions from the radiochemical separations. For source preparation efforts at MSU Chemistry laboratory, $^{7}$Be was detected and quantified with an HPGe Canberra BEGe γ-ray Detector (BE2020). The determination of boron and beryllium during the separation methodology development at MSU was performed with an Agilent inductively coupled plasma-optical emission spectrometer (Agilent 5900 SVDV ICP-OES) and analyzed with Agilent ICP software.

5.2.1.1 Target Preparation

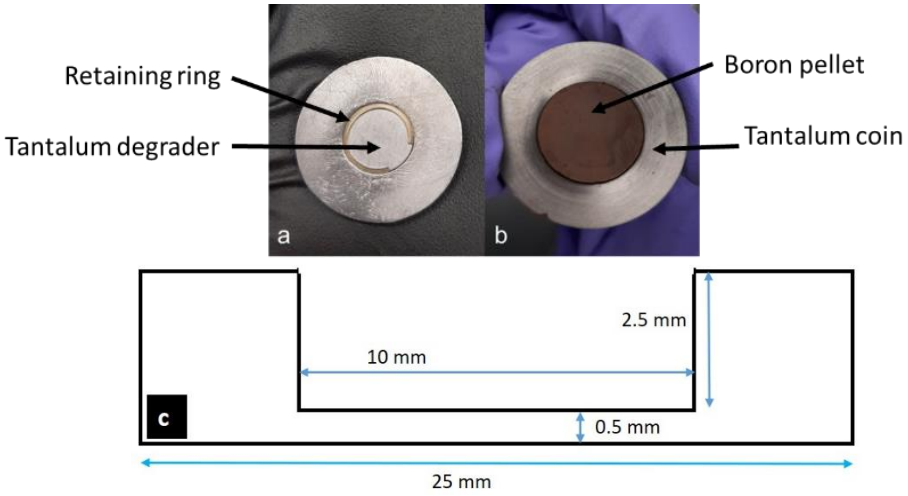


**Figure 5.2**: Closed view of the tantalum coin with enclosed boron pellet having the tantalum degrader and retaining ring at the top is shown in (a) and (b) shows the open view of the coin containing the pressed boron pellet (c) schematic of Type 2 targets in shown.

Two categories of targets, referred to as Type 1 and Type 2, were designed for the irradiation process. Type 1 targets comprised approximately 100-102 mg of natural amorphous boron powder, that has an average particle size of less than 1.0 micron. This boron powder was compacted into 1-mm-thick circular pellets with a 10-mm diameter using a hydraulic press (model 3664, Carver, Inc.) and a 10-mm die (FTIR Evacuable Pellet Die, GS03100, Specac). The press applied incremental force, ranging from 1 to 5 tons, with each ton maintained for one minute before reaching 5 tons, which was then sustained for 5 minutes. These pellets were then

placed within the 1.5-mm-deep indentation of a 2-mm-deep tantalum coin (as illustrated in **Figure 5.2 (b)**). A tantalum foil, 0.25-mm thick and cut to a 10-mm diameter using a punch and die set (Precision Brand Products), was placed atop the boron pellet. Functioning as a degrader, the tantalum foil was secured in position by a single-turn spiral internal retaining ring (3/8" OD in 18-8 Stainless steel, McMaster-Carr) inserted around its circumference (as depicted in **Figure 5.2 (a)**). The tantalum coin itself, with a thickness of 0.5 mm, served as the backing material for the target after subtracting the divot's depth from the coin's total thickness. In total, three Type 1 targets were prepared.

Type 2 targets were prepared using 199-204 mg of $^{10}$B-enriched powder, which was compacted into a 1.8-mm-thick circular pellet with a 10-mm diameter. This pellet was then inserted into the 2.5-mm-deep indentation of a 3-mm-deep tantalum coin. The tantalum degrader and the thickness of the tantalum backing remained consistent with those of the Type 1 targets. A total of four Type 2 targets were fabricated and a schematic is shown in **Figure 5.2 (c)**. The tantalum coins utilized for both Type 1 and Type 2 targets underwent machining processes at UAB.

5.2.1.2 Irradiation at UAB

The pressed Type 1 and 2 targets underwent irradiation at the TR-24 Cyclotron, located within the UAB Cyclotron Facility. The proton beam extracted for irradiation had an energy of 17.5 MeV. In total, seven irradiation sessions were conducted, with three involving Type 1 targets and four involving Type 2 targets.

These targets were inserted into the coin holder of the solid cyclotron target station at UAB [29]. The front side of the target underwent helium cooling, while the back side was water-cooled. Irradiation durations ranged from 30 minutes to 7 hours, with beam currents varying

between 5 and 10 μA. Subsequently, the bombarded targets were left within the target station for a minimum of 4 hours to allow for the decay of the co-produced $^{11}C$, which has a half-life of 20.36 minutes.

5.2.1.3 Experimental production yield of $^{7}Be$

Following the bombardment process, the dissolved irradiated targets were analyzed using an HPGe Detector and assessed using the Canberra Genie 2000 software to quantify $^{7}Be$. This involved detecting and integrating peaks based on the distinctive γ-ray emission, conducting background subtraction, and calculating activity based on the net peak area. Energy and efficiency calibrations were made utilizing a 1 mL mixed nuclide source (manufactured by Eckert & Ziegler) enclosed in a sealed 1.5 mL micro centrifuge vial, positioned at distances of 5 and 25 mm away from the detector face. To ensure precise quantification, samples from each collected fraction of the radiochemical separations were pipetted into 1.5 mL Eppendorf screw-cap conical centrifuge tubes, diluted with MilliQ water to reach a volume of 1 mL, and subjected to γ-ray spectroscopy. The distance from the detector face was selected based on the sample's activity to maintain a dead time below 5% for all measurements.

5.2.2 Separation of $^{7}$Be from boron pellet targets

5.2.2.2 Dissolution of target

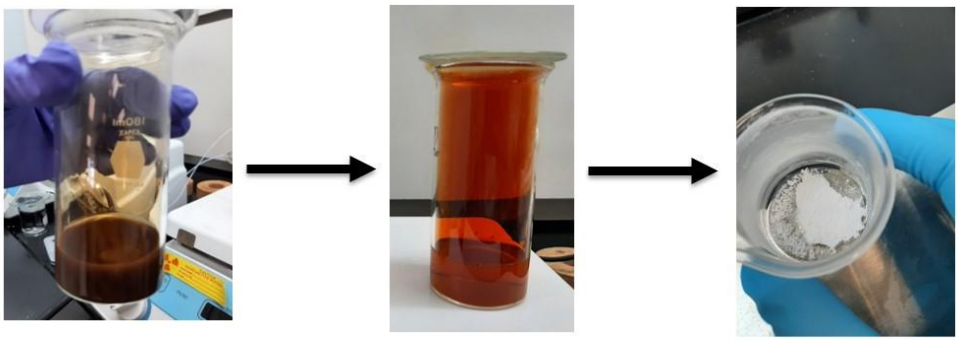

**Figure 5.3:** The stepwise dissolution process of the boron pellet targets is shown leading to pure boric acid powder in the end.

All target dissolutions were conducted within a fume hood. The disassembly of the target involved the removal of the retaining ring and the tantalum degrader. Subsequently, the boron pellets were carefully extracted from the divot using a spatula and transferred into a beaker containing 40-60 mL of concentrated $HNO_3$ (Suprapur). If a significant amount of boron powder remained adhered to the tantalum coin, the coin itself was immersed in the nitric acid solution and removed once the powder had completely dissolved. The solution was then heated to 100°C for a duration of 10 to 12 hours until the boron pellet dissolved entirely. Upon dissolution, the nitric acid solution was allowed to evaporate at 120°C, resulting in the formation of white boric acid powder residue (**Figure 5.3**). This residue was subsequently reconstituted in 0.1 M $HNO_3$ to achieve a concentration of 1 mg of boron per mL, serving as the loading solution for the separation process. An aliquot was withdrawn from this target solution, and the activity of $^{7}$Be was determined through gamma spectroscopy.

5.2.2.1 Development of the separation methodology with stable elements

To refine the separation procedure, various conditions were tested with stable elements, involving the dissolution of boron powder ranging from 10.8 - 538 mg in 10-75 mL of

concentrated $HNO_3$, heated to 100°C. Complete evaporation at 120°C resulted in boric acid formation, which was then dissolved in 0.1 M $HNO_3$. Following the addition of 1 mg of Be tracer, the separation of boron and beryllium was carried out in 0.1 M $HNO_3$ using an AG MP-50 column, slurry packed with 1.5 - 2.5 grams of resin.

Before separation, the column underwent pre-conditioning with 20 mL MilliQ water, followed by sequential washes with 20 mL 2 M $HNO_3$ and 20 mL 0.1 M $HNO_3$, all at a flow rate of 1 mL/min. Once the 0.1 M $HNO_3$ load solution passed through the column at 0.8 mL/min, the column was rinsed with 1 M $HNO_3$, and Be was eluted using 4 M $HNO_3$ at a constant flow rate of 0.8 mL/min.

To evaluate separation efficiency, aliquots of each eluted fraction were withdrawn and diluted in 3% (v/v) $HNO_3$ to volumes of 5-10 mL. The quantities of stable boron and beryllium were determined by ICP-OES using calibration curves generated from standard solutions containing Be and B in the concentration range of 0.1 - 50 ppm. The percentage of eluted boron and beryllium was calculated by dividing the amount of eluted element by the initial amount present in the loading solution for all cold separations. This optimized separation methodology effectively removed bulk boron and was employed to process the irradiated targets.

5.2.2.3 Radiochemical separation

The radiochemical separations were conducted employing a peristaltic pump (Ismatec® Reglo Peristaltic Pump with independent channel control, utilizing pump tubing with a 1.65-millimeter internal diameter). Before each separation, the pump underwent calibration to ensure a consistent flow rate. The columns were assembled by slurry-packing the cation-exchange resin AG MP-50 (100−200 mesh, in $H^+$ form, BioRad) into transparent polycarbonate tubes measuring approximately 15 cm in length (with a 3/8″ outer diameter and 1/4″ inner diameter, obtained

from McMaster-Carr, PN:9176T1). Glass wool inserts were placed at both ends of the columns. Push-to-connect fittings consisting a poly(butylene terephthalate) (PBT) body (Pneumatic NITRA Union Reducer, 3/8″ to 1/4″) were used to link one end of the column to the loading solution and the other end to a peristaltic pump using clear Tygon tubing.

For each separation, a fresh column was prepared, resulting in a total of six columns (with an outer diameter of 9 mm, inner diameter of 6 mm, and length ranging from 15-18 cm), each containing 2.5 g AG MP-50 resin. Pre-conditioning of the columns involved passing 25 mL MilliQ water, followed by 20 mL 2 M $HNO_3$, and then 20 mL 0.1 M $HNO_3$ sequentially, at a flow rate of 1 mL/min.

The 0.1 M $HNO_3$ load solutions containing boric acid and $^{7}Be$ were passed through the columns at a flow rate of 0.8 mL/min, with fractions collected. Residual boron was washed from the column using 10 mL 0.1 M $HNO_3$ and collected in subsequent fractions. Further rinsing was achieved through sequential use of 6 mL 1 M $HNO_3$. Finally, $^{7}Be$ was eluted in 3-4 fractions, each containing 8-9 mL 4 M $HNO_3$. A final rinse with 10-13 mL MilliQ water was performed to reduce acidity and ensure suitable storage conditions for the equipment.

This entire procedure was repeated six times for seven irradiated boron targets. In one instance, two targets containing 203.5 mg and 200.5 mg of boron powder, respectively, were

combined to assess the reproducibility of the separation method by scaling up the boron quantity. The separation methodology utilizing AG MP-50 resin in this study is illustrated in **Figure 5.4**.

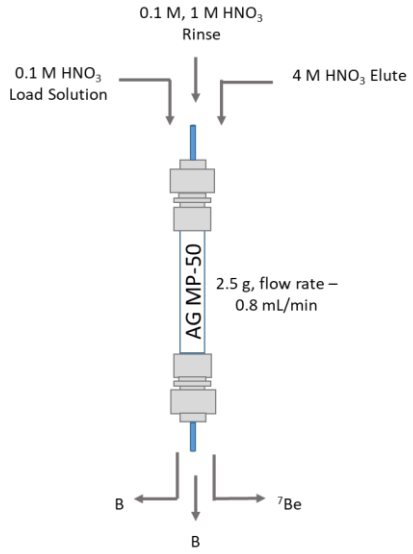


**Figure 5.4**: A schematic of the entire separation process for boron and beryllium on AG-MP 50 is shown.

5.2.2.4 Quantification with ICP-MS

At the end of the separation process for the combined target, 5 and 7, ICP-MS samples were prepared for measurement at UAB for quantification of $^{10}B$ and $^{11}B$. Due to the high levels of radioactivity of $^{7}Be$, the elute fractions were not analysed. Multi-element standards in 2% $HNO_3$ was used to create a calibration curve of 50, 100, 200, 500, 800 and 1000 ppb for both $^{10}B$ and $^{11}B$. All ICP-MS samples were made in triplicates. For the load fractions, two different dilutions for ICP-MS sample were prepared in 2 % $HNO_3$: 1:1200 and 1:1400 dilution. For the rinse fractions and water fraction, a 1:2 and 1:4 dilutions were made in 2 % $HNO_3$.

### 5.2.3 $^{7}$Be in BMIS

#### 5.2.3.1 Source preparation

A total of four source samples containing $^{7}$Be activities were prepared. From the separations conducted using Type 1 targets, the fraction of 4 M $HNO_3$ displaying the highest $^{7}$Be activity was identified and utilized for two separate source sample preparation endeavors. From the separations using Type 2 targets, the fractions containing $^{7}$Be within the 4 M $HNO_3$ were combined, subjected to evaporation until dryness at temperatures ranging from 150-200 °C, and then reconstituted in 0.1 M HCl before being divided between two micro-centrifuge vials.

Upon transportation to the MSU radiochemistry laboratory, gamma spectroscopic measurements were conducted with each Eppendorf vial, after which this activity was further concentrated through evaporation. The concentrated solution was then pipetted onto a 1x1 $cm^2$ tantalum foil, which measured 6 µm in thickness (99.9% purity, Goodfellow). This process involved repeatedly pipetting 10-12 µL droplets onto the foil while heating it to temperatures of 150-200 °C using a hot plate. Subsequently, these tantalum foil source samples, with the $^{7}$Be deposited, were then transported to NSCL.

#### 5.2.3.2 $^{7}$Be Beam delivery

The tantalum foils having $^{7}$Be deposits underwent a tight folding process before their insertion into BMIS oven. Typically, one foil sample was introduced into the BMIS oven during each operation. The oven was resistively heated to temperatures ranging from 700 - 1800 °C. $NF_3$ gas served as a reactive carrier gas, introduced into the oven to facilitate the conversion of $^{7}$BeO, a refractory compound, into $^{7}$Be-$F_x$ adduct molecules possessing higher vapor pressure. Subsequently, the evaporated sample materials effused through a tantalum transfer tube into the

VD5 ion source, where the molecules underwent ionization, primarily being extracted as $[^{7}Be\text{-}F_x]^+$ molecular ions.

Control over the $^{7}Be$ ion beam rate was achieved by regulating the oven temperature and $NF_3$ gas flow (partial pressure). The extracted ion beam, comprising the $^{7}Be$ molecular ions alongside other stable contaminants, was accelerated to 30 keV and sent to the magnetic mass separator, where the desired $^{7}Be$ molecular ions were selectively isolated. Eventually, the selected ion beam was transported to the stopped-beam area (LEBIT) or the ReA accelerator post-charge breeding to the $4^+$ atomic charge state. Four $^{7}Be$ sources were employed to provide beams for five experiments.

**5.3 Results and discussion**

5.3.1 Theoretical production yield determination of $^{7}Be$

For the calculation of the theoretical production yields before the irradiations were carried out, the Stopping and Range of Ions in Matter (SRIM) compilation was used to determine the entrance and exit proton energies in a boron target, using the measured density of (1.40 ± 0.3) $g/cm^3$ (**Table C.1 and C.2**). According to the SRIM compilation, for Type 1 targets, the proton beam entered the boron target after passing through the tantalum degrader with 11.5 MeV energy and left the boron pellet with 5.8 MeV energy (**Figure 5.5**). The proton beam was finally stopped in the first 0.1 mm of the 0.5 mm Ta backing of the coin. The experimental (p,α) reaction cross-section data for $^{10}B$ target nuclei were retrieved from the Experimental Nuclear Reaction Data database over the 0.5 - 12 MeV proton energy range, while the theoretical reaction cross-section data was computed with the TALYS-2019 code and retrieved from the TENDL library (**Figure 5.6**). The production calculations were made using Equation 5.1 below and the integral was approximated by numerical integration over the energy range of 11.5 - 5.8 MeV.

$$\boldsymbol{P} = \int_{E_i}^{E_f} \frac{\boldsymbol{\sigma(E) N_A \rho}}{\boldsymbol{S_P(E) * M}} \boldsymbol{dE} \tag{5.1}$$

P is the production rate of $^{7}$Be (atoms/proton), σ is the energy-dependent reaction cross section ($cm^2$), $N_A$ is the Avogadro constant (6.02 x $10^{23}$ atoms/mol), ρ is the density of $^{10}$B, dE is the difference in energy (MeV), $S_P$ is the stopping power of the beam in the target material (MeV/cm) and M is the molar mass of the target material (g/mol). Equation 5.2 was used to compute the produced activity of $^{7}$Be over the irradiation time where A is the activity of produced $^{7}$Be (Bq/μA*h), P is the production rate of $^{7}$Be(atoms/proton), obtained from Equation 5.1, I is the beam current (protons/s), λ is the decay constant ($s^{-1}$) and t is the irradiation time (s).

$$\boldsymbol{A = P * I\left(1 - e^{-\lambda t}\right)} \tag{5.2}$$

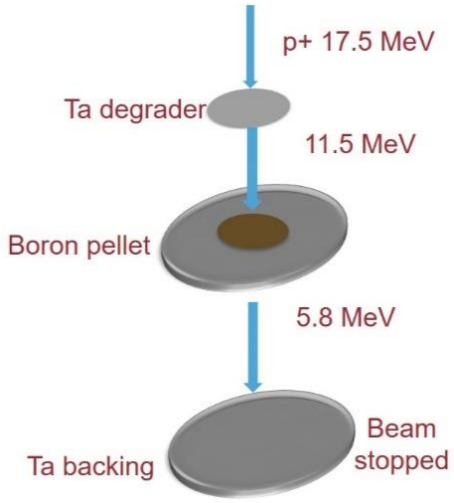


**Figure 5.5:** A schematic of the 17.5 MeV proton beam traversing the tantalum degrader, boron pellet, and finally stopping in the tantalum coin backing is shown.

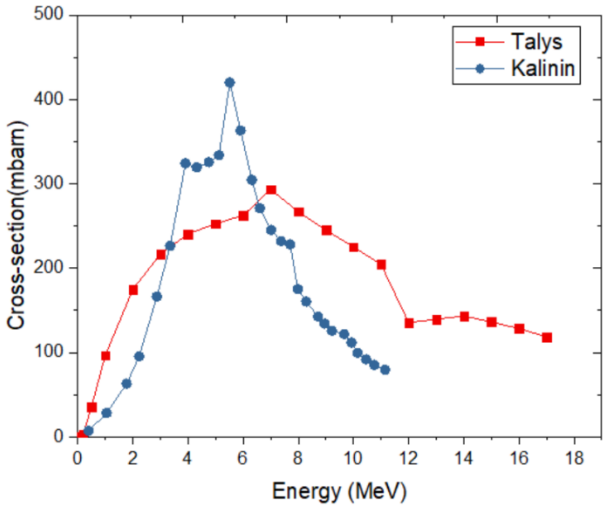


**Figure 5.6:** Cross-section versus energy for the $^{10}B(p,\alpha)^{7}Be$ nuclear reaction is shown where the experimental data was chosen from Kalinin, 1957 and is largely comparable to the data set obtained from the TALYS-2019 code [37], [38].

5.3.2 Proton irradiation of boron targets

Table 5.1: The parameters for the irradiations of boron target Type 1 and Type 2 and the experimental yields are given. *note the targets for irradiations 5 and 7 were combined for the measurement of activity.

| **Irradiation** | **Target type** | **Target** | **Irradiation Time (h)** | **Proton Beam current (μA)** | **μAh** | **Total $^{7}$Be MBq (μCi) experimental** |
|---|---|---|---|---|---|---|
| 1 | Type 1 | $^{nat}B$ | 0.5 | 5 | 2.5 | 1.3 ± 0.03 (33.7) |
| 2 | Type 1 | $^{nat}B$ | 0.5 | 10 | 5 | 2.3 ± 0.1 (62.5) |
| 3 | Type 1 | $^{nat}B$ | 1 | 10 | 10 | 4.8 ± 0.1 (129.1) |
| 4 | Type 2 | $^{10}B$ | 3 | 5 | 15 | 44.5 ± 0.3 (1203.8) |
| 5 | Type 2 | $^{10}B$ | 6 | 6 | 36 | |
| 6 | Type 2 | $^{10}B$ | 4 | 6 | 24 | 72.9 ± 0.5 (1969.5) |
| 7 | Type 2 | $^{10}B$ | 7 | 6 | 42 | |
| 5+7 (combined)* | Type 2 | $^{10}B$ | | | 78 | 217.4 ± 1.3 (5876.2) |

The boron targets underwent irradiation using proton beam currents ranging from 5-10 μA. During this process, noticeable scorching or burn marks were detected on the second and third targets when subjected to a beam current of 10 μA. As a result of this observation, adjustments were made to lower the beam currents for subsequent irradiations. Detailed parameters for all irradiations involving both Type 1 and Type 2 targets can be found in **Table 5.1**.

For these experiments, another nuclear-reaction channel was $^{11}B(p,n)^{11}C$, with a theoretical production rate of 7.74 GBq $^{11}C$/μAh, making it the only other radioisotope with a half-life greater than 1 minute. The resulting $^{11}C$ was allowed to decay prior to target processing. Notably, the contribution of the $^{11}B(p,\alpha n)^{7}Be$ nuclear reaction to the $^{7}Be$ production was considered negligible, given its minimal cross-section below the 11.2 MeV threshold [30], [31].

The values obtained for the yields are roughly $5 \times 10^{-1}$ MBq $^{7}Be$/μAh for type 1 targets, and $3 \times 10^{0}$ MBq $^{7}Be$/μAh for Type 2 targets. These irradiations were not designed for precise determination of nuclear data but rather practical $^{7}Be$ production. In the above cases, it was not possible to determine if all of the delivered beam current actually interacted with the boron target because the entire target body, including the retaining ring, was conductive. This is why the experimental yield numbers are not meaningful to compare to theoretical yields.

A gamma spectrum of the assembled target coin # 6 after irradiation is shown in **Figure 5.7**, which is representative of other irradiated targets. The presence of $^{56}Co$ is due to the activation of the retaining ring, which can be seen in another gamma spectrum of only the retaining ring and tantalum foil, shown in the **Figure 5.8**. Through the γ-spectroscopic measurements, the total activity of $^{7}Be$ measured in seven targets was 343.2 ± 1.4 MBq.

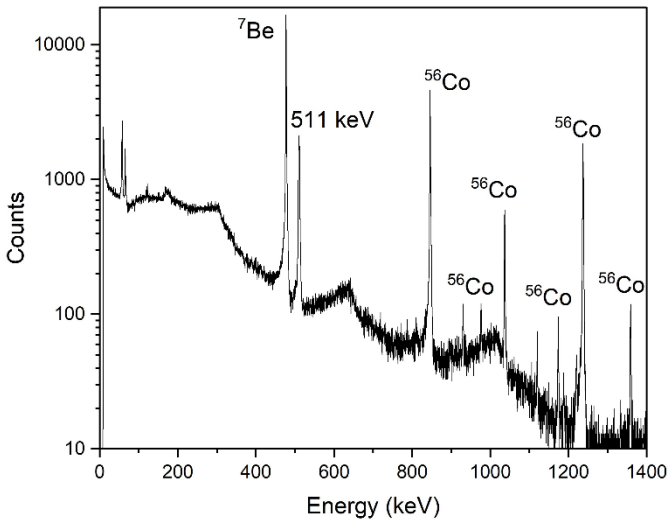


**Figure 5.7:** The gamma spectrum of the assembled target #6, counted for 30 minutes is shown where the $^{56}$Co peaks are due to the activation of the retaining ring.

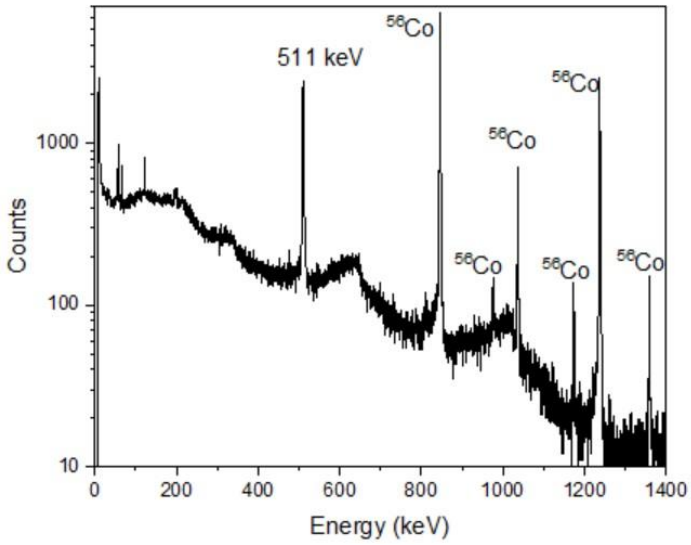


**Figure 5.8:** The gamma spectrum of the retaining ring and tantalum foil minus the boron pellet is shown.

5.3.3 Separation of $^{7}Be$ from $^{nat}B$ and enriched $^{10}B$ targets

Earlier research has shown that elemental boron can be dissolved through treatment with nitric acid, either with or without the addition of hydrogen peroxide [32]. In this study, the use of hot concentrated nitric acid alone led to the complete dissolution of both natural and enriched boron pellets. It's worth noting that the dissolution process involving boron and nitric acid produced brown $NO_x$ fumes, emphasizing the necessity for adequate ventilation during such procedures. Subsequent evaporation and reconstitution of the targets using 0.1 M nitric acid proved to be straightforward in all cases.

Table 5.2: Distribution coefficient values obtained for Be(II) in the nitric acid medium is shown [28].

| | **0.1 M $HNO_3$** | **0.2 M** | **0.5 M** | **1.0 M** | **2.0 M** | **3.0 M** | **4.0 M** |
|---|---|---|---|---|---|---|---|
| **Be(II)** | 553 | 183 | 52 | 14.8 | 6.6 | 4.5 | 3.1 |

For the seven irradiations outlined in **Table 5.1**, a total of six separation attempts were undertaken. To evaluate the reliability of the separation procedure, targets 5 and 7 were combined prior to chemical processing. The separation relied on the fact that boron, as boric acid, does not absorb onto cation exchange resin AG MP-50, whereas beryllium is strongly adsorbed by cation exchange resin from low-molarity nitric acid, as shown by the distribution coefficient ($K_d$) values in **Table 5.2** [28], [33].

During the passage of load solutions through the columns, boron was completely eluted in every separation, with no detectable breakthrough of $^{7}Be$, even when the boron content was increased (approximately 404 mg) by combining targets 5 and 7. Additionally, there was no discernible difference in elution efficiency between natural boron and enriched $^{10}B$.

For the combined targets (5 and 7), the ICP-MS analysis yielded a calculated mass of (359.8 ± 2.2) mg for $^{10}B$ in the load fractions where initially, the total mass of targets 5 and 7 was 404 mg. To ensure the complete elution of boron, additional rinse fractions containing 0.1 M $HNO_3$ were employed, followed by a subsequent increase in molarity to 1 M $HNO_3$, guaranteeing the thorough removal of boron while preserving the adsorption of $^{7}Be$ [34]. The quantity of boron, as determined by ICP-MS analysis of the combined targets (5+7) in the rinse fractions, amounted to (3.3 ± 0.2) mg. Subsequently, the elution of $^{7}Be$ was achieved by raising the molarity to 4 M $HNO_3$, resulting in an average recovery of (99.4 ± 3.7)% compared to the loading solution, within 8-9 mL eluate each [33]. The overall error in these measurements encompasses both the dilution and activity measurement errors.

The gamma spectrum of the load solution and $^{7}Be$ fraction, captured before and immediately after the separation of the foils, is depicted in **Figure 5.9** and **Figure 5.10**, respectively. **Figure 5.11** illustrates a representative elution profile of the separation process involving the target # 6.

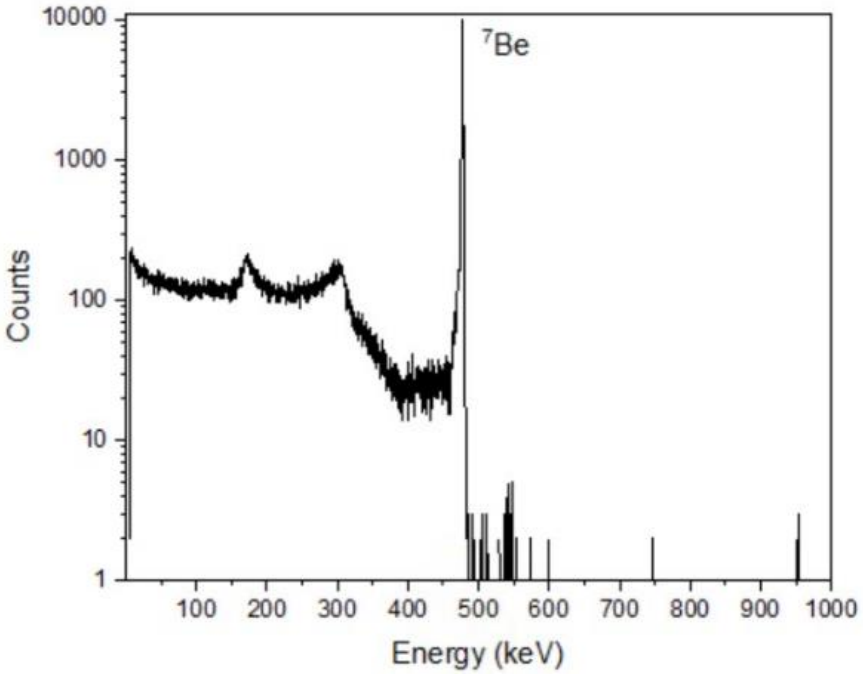


**Figure 5.9:** The gamma spectrum of the load solution before attempting radiochemical processing is shown.

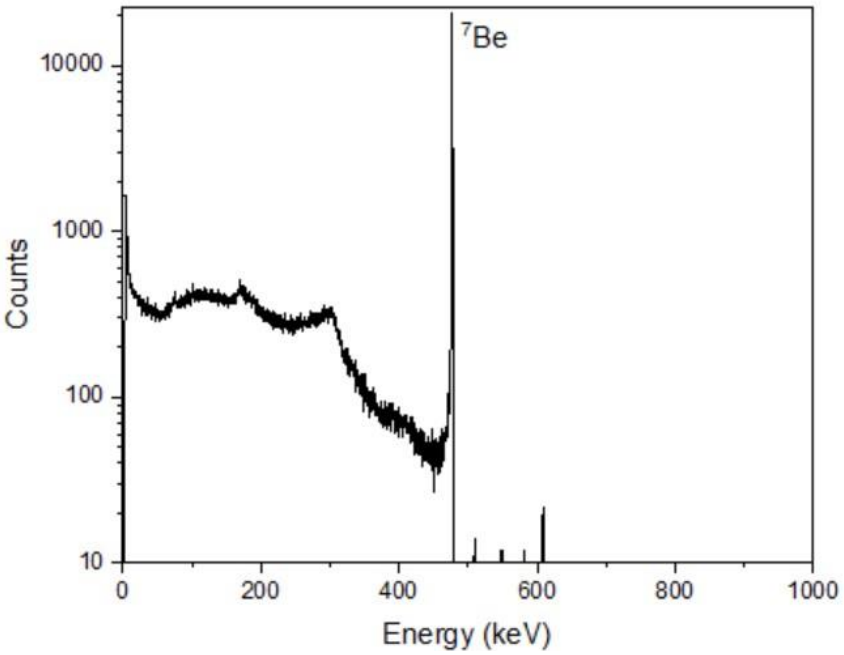


**Figure 5.10:** The gamma spectrum of the purified $^{7}$Be fraction, obtained after the radiochemical separation, counted for an hour, is shown.

5.3.4 Quantification of boron with ICP-MS

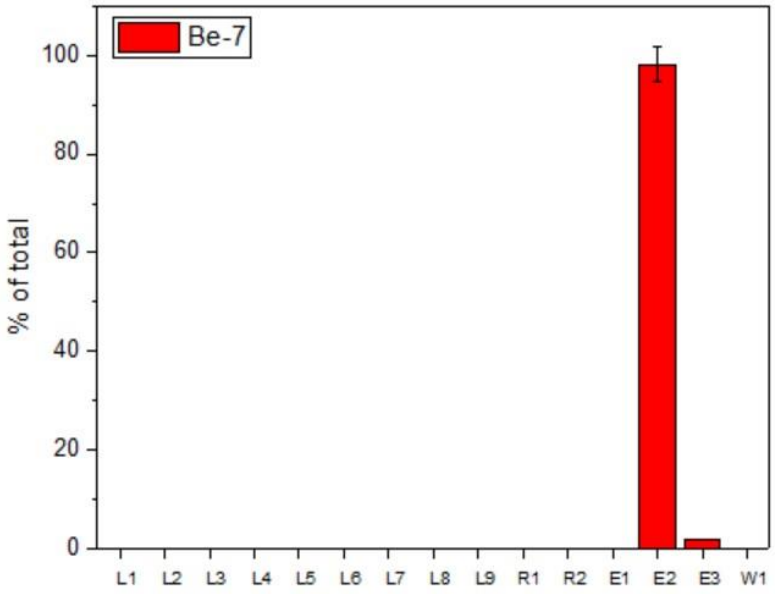


**Figure 5.11:** The elution profile obtained for separation with target # 6 using AG MP-50 resin for the extraction of $^{7}$Be is shown. The load fractions (L1 - L9) comprising of 0.1 M $HNO_3$ are approximately 33 mL each. The rinse fraction R1 is 10 mL 0.1 M $HNO_3$ followed by rinse fraction R2 which is 6 mL of 1 M $HNO_3$, and the elute fractions (E1 - E3) are 9 mL each of 4 M $HNO_3$ containing $^{7}$Be. This is followed by wash fraction W1 comprising water.

Samples were extracted from each eluate and measured to ascertain the boron distribution in the fractions. The ICP-MS findings for the combined targets (5 and 7) are outlined in **Figure 5.12** and in **Table 5.3**. The boron collection fraction exhibited an average recovery of 359.8 ± 2.2 mg, corresponding to approximately 89% recovery from the initial mass of the two targets, totaling 404 mg. Both elution 1 and the wash displayed minimal presence of $^{10}$B and $^{11}$B, with ≤0.03 mg detected, thereby confirming the efficacy of the purification method for isolating the $^{7}$Be radionuclide from the $^{10}$B target. Elution 2 and 3 were not directly measured due to elevated levels of radioactivity; however, their estimated masses were extrapolated using data from

elution 1. The estimated boron content for combined elutions 1-3 amounted to 0.05 mg of $^{10}B$ and less than 0.01 mg of $^{11}B$.

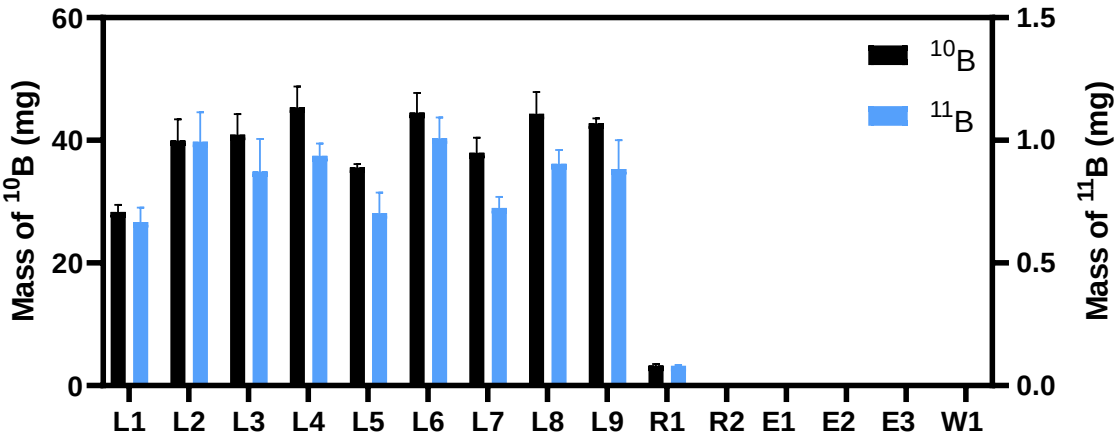


**Figure 5.12:** The elution profile for $^{10}B$ and $^{11}B$ for the combined targets 5 and 7 is shown. The mass of recovered $^{10}B$ and the mass of the recovered $^{11}B$ is reported on left and right y-axis, respectively. The concentrations of E2 and E3 were estimated using E1. The load fractions (L1 - L9) comprising of 0.1 M $HNO_3$ are approximately 33 mL each. The rinse fraction R1 is 10 mL 0.1 M $HNO_3$ followed by rinse fraction R2 which is 6 mL of 1 M HNO3. The elute fractions (E1 - E3) are 9 mL each of 4 M $HNO_3$ containing $^{7}Be$. This is followed by wash fraction W1 comprising 13.5 mL of water. Image provided by Shelbie Cingoranelli.

Table 5.3: The ICP-MS results of the $^{10}B$ and $^{11}B$ separation. Note that those marked *are estimated mass of B based on measured FR12 (E1).

| FRACTION | MATRIX | $^{10}B$ MG | | S.D | $^{11}B$ MG | S.D |
|---|---|---|---|---|---|---|
| **L1** | 0.1 M $HNO_3$ | 28.31 | | 1.16 | 0.67 | 0.06 |
| **L2** | 0.1 M $HNO_3$ | 39.99 | | 3.45 | 0.99 | 0.12 |
| **L3** | 0.1 M $HNO_3$ | 40.94 | | 3.35 | 0.87 | 0.13 |
| **L4** | 0.1 M $HNO_3$ | 45.37 | | 3.39 | 0.94 | 0.05 |
| **L5** | 0.1 M $HNO_3$ | 35.59 | | 0.55 | 0.70 | 0.08 |
| **L6** | 0.1 M $HNO_3$ | 44.54 | | 3.20 | 1.01 | 0.08 |
| **L7** | 0.1 M $HNO_3$ | 38.00 | | 2.41 | 0.72 | 0.04 |
| **L8** | 0.1 M $HNO_3$ | 44.31 | | 3.54 | 0.90 | 0.06 |
| **L9** | 0.1 M $HNO_3$ | 42.78 | | 0.77 | 0.88 | 0.12 |
| **R1** | 0.1 M $HNO_3$ | 3.27 | | 0.28 | 0.08 | <0.01 |
| **R2** | 1 M $HNO_3$ | <0.01 | | <0.01 | <0.01 | <0.01 |

Table 5.3 (cont'd)

| | | | | | | |
|---|---|---|---|---|---|---|
| **E1** | 4 M $HNO_3$ | 0.02 | | <0.01 | <0.01 | <0.01 |
| **E2** | | 0.02 | | * | <0.01 | * |
| **E3** | | 0.02 | | * | <0.01 | * |
| **W1** | Water | 0.01 | | <0.01 | <0.01 | <0.01 |

5.3.5 Source preparation & $^{7}$Be beam delivery

**Figure 5.13** shows the $^{7}$Be pipetted on the tantalum foil for making the source and when it was folded tightly and inserted into the BMIS oven. The rates of $^{7}Be^{4+}$ ion beam was assessed post-Re-accelerator, with the highest rate achieved when fine-tuning the pre-separator to direct the $([^{7}Be]BeF_2)^{+}$ molecular ion beam into the charge breeder across the entire temperature range of the oven (700-1800 °C). There was no notable alteration in molecular composition throughout the operating temperature range for the formation of BeF, $BeF_2$, and $BeF_3$ at various temperatures. **Figure 5.14** illustrates that the purity of the delivered beam was 100%, independently confirmed via mass spectroscopy conducted by LEBIT at FRIB [35].

The overall efficiency of the ion source for $^{7}$Be was determined to be 3%, utilizing a 0.126 μCi (4.7 kBq) $^{7}$Be-loaded foil. A comprehensive account of the procedure and results pertaining to the efficiency measurement can be found in Sumithrarachchi et al. [3]. The remaining three sources, having activities of 1.2 mCi (44.4 MBq), 1.8 mCi (66.6 MBq), and 1 mCi (37 MBq), were allocated for three ReA experiments and one experiment in the LEBIT

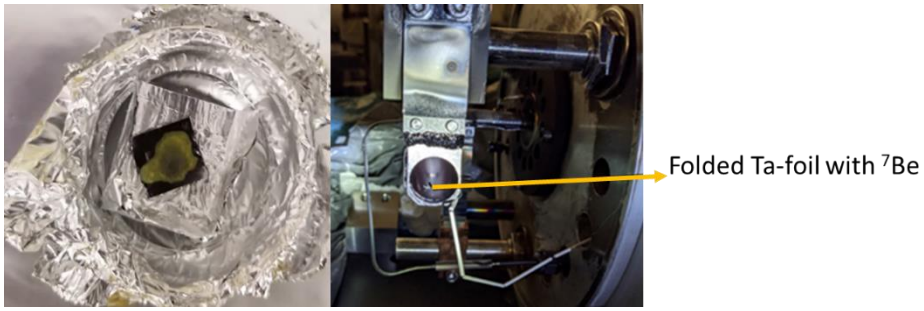


**Figure 5.13:** (left) $^{7}$Be pipetted on the tantalum foil for the purpose of making the $^{7}$Be source (right) The tantalum foil is folded and placed inside the BMIS oven. Images provided by Dr. Katharina Domnanich.

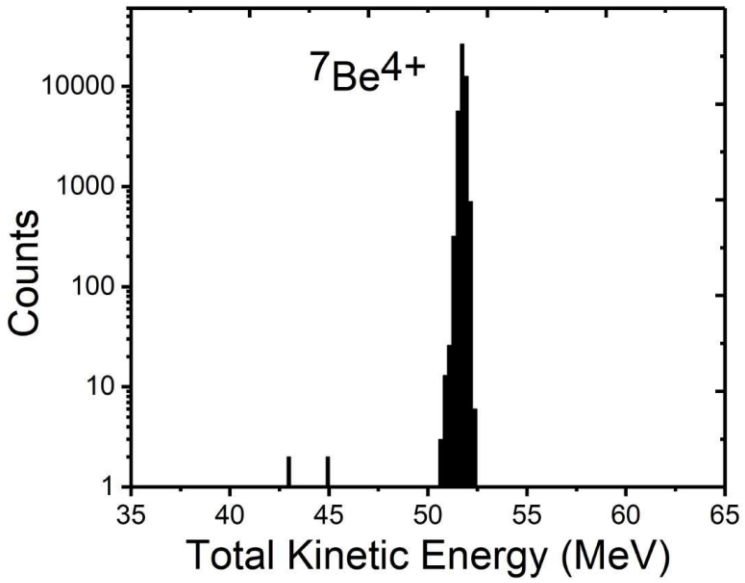


**Figure 5.14:** Silicon-detector spectrum of $^{7}Be^{4+}$ beam measured after the ReA accelerator when the magnetic mass separator was selected at mass of 45 amu ($[^{7}Be]BeF_2$). The silicon detector measures the total kinetic energy of the incident particle which is a characteristic identification of $^{7}$Be before experiments [3]. Image provided by Dr. Chandana Sumithrarachchi.

area. An average rate of $5x10^5$ particles per second (pps) was supplied to all experiments over a total duration of 350 hours.

## 5.4 Conclusion

The findings of this study includes the production of $^{7}$Be utilizing both natural and enriched boron targets. A highly efficient separation method was devised, employing a cation-exchange resin, resulting in pure $^{7}$Be fractions with an average extraction efficiency of (99.4 ± 3.7)% and 100% radionuclidic purity (within the limit of detection).

Following this, preparation of $^{7}$Be source samples was conducted, and these samples were provided to the BMIS group to generate a $^{7}$Be beam. Subsequently, the beam was utilized

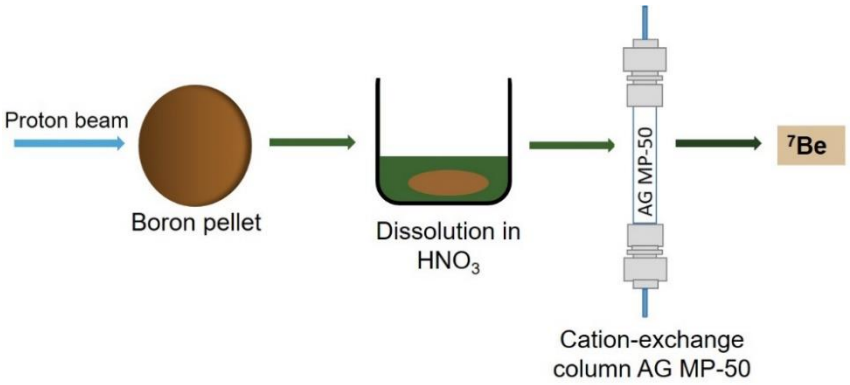


**Figure 5.15:** A schematic of the entire process till obtaining pure $^{7}$Be.

in four nuclear physics experiments at the NSCL. This study demonstrated the comprehensive process involved in establishing offline radioactive beams at the NSCL, encompassing $^{7}$Be isotope production, separation from boron target material, source sample preparation, and the delivery of $^{7}Be^{4+}$ beams to scientific users. This was also the first source sample prep where the entire pipeline was demonstrated, from production to source sample prep and is demonstrated in the schematic in **Figure 5.15**.

## REFERENCES


[1] "National Nuclear Data Center." Accessed: Mar. 22, 2024. [Online]. Available: https://www.nndc.bnl.gov/nudat3/

[2] C. Broggini, L. Canton, G. Fiorentini, and F. L. Villante, "The cosmological 7Li problem from a nuclear physics perspective," *Journal of Cosmology and Astroparticle Physics*, vol. 2012, no. 6, Jun. 2012, doi: 10.1088/1475-7516/2012/06/030.

[3] C. S. Sumithrarachchi *et al.*, "The new Batch Mode Ion Source for stand-alone operation at the Facility for Rare Isotope Beams (FRIB)," *Nucl Instrum Methods Phys Res B*, vol. 541, pp. 301–304, Aug. 2023, doi: 10.1016/j.nimb.2023.05.061.

[4] A. Lapierre *et al.*, "Commissioning results of the ReA EBIT charge breeder at the NSCL: First reacceleration of stable-isotope beams," *Nucl Instrum Methods Phys Res B*, vol. 317, no. PART B, pp. 399–401, Dec. 2013, doi: 10.1016/j.nimb.2013.06.034.

[5] L. Penescu, R. Catherall, J. Lettry, and T. Stora, "Development of high efficiency Versatile Arc Discharge Ion Source at CERN ISOLDE," in *Review of Scientific Instruments*, 2010. doi: 10.1063/1.3271245.

[6] K. A. Domnanich *et al.*, "Preparation of stable and long-lived source samples for the stand-alone beam program at the Facility for Rare Isotope Beams," *Applied Radiation and Isotopes*, vol. 200, Oct. 2023, doi: 10.1016/j.apradiso.2023.110958.

[7] M. Gaelens, M. Cogneau, M. Loiselet, and G. Ryckewaert, "Post-acceleration of 7Be at the Louvain-la-Neuve radioactive ion beam facility," in *Nuclear Instruments and Methods in Physics Research, Section B: Beam Interactions with Materials and Atoms*, May 2003, pp. 48–52. doi: 10.1016/S0168-583X(02)01889-X.

[8] N. Gharibyan *et al.*, "Production and separation of carrier-free 7Be," *Applied Radiation and Isotopes*, vol. 107, pp. 199–202, Jan. 2016, doi: 10.1016/j.apradiso.2015.10.028.

[9] H. R. Haymond, W. M. Garrison, J. G. Hamilton, and E. Org, "Lawrence Berkeley National Laboratory Recent Work Title CARRIER-FREE RADIOISOTOPES FROM CYCLOTRON TARGETS. XII. PREPARATION AND ISOLATION OF Be 7 FROM LITHIUM Permalink https://escholarship.org/uc/item/74j712fb Publication Date," 1950. [Online]. Available: https://escholarship.org/uc/item/74j712fb

[10] L. Gialanella *et al.*, "Off-line production of a 7Be radioactive ion beam," *Nucl Instrum Methods Phys Res B*, vol. 197, no. 1, pp. 150–154, 2002, doi: https://doi.org/10.1016/S0168-583X(02)01386-1.

[11] T. Ohtsuki, S. I. Fujikawa, and H. Yuki, "Preparation of carrier-free 7Be by ion-exchange following charged particle and photonuclear reactions," *Applied Radiation and Isotopes*, vol. 59, no. 4, pp. 221–223, Oct. 2003, doi: 10.1016/S0969-8043(03)00200-8.

[12] F. Maekawa, Y. M. Verzilov, D. L. Smith, and Y. Ikeda, “Experimental study on beryllium-7 production via sequential reactions in lithium-containing compounds irradiated by 14 MeV neutrons,” *Journal of Nuclear Materials*, vol. 283–287, pp. 1448–1452, 2000, doi: https://doi.org/10.1016/S0022-3115(00)00182-3.

[13] M. Loiselet, M. Gaelens, and G. Ryckewaert, “THE DEVELOPMENT OF A BE-7 RADIOACTIVE BEAM : FROM NUCLEAR PHYSICS TO APPLICATIONS FOR INDUSTRY,” 2004. [Online]. Available: https://api.semanticscholar.org/CorpusID:225101083

[14] M. Wiescher, R. J. Deboer, J. Görres, and R. E. Azuma, “Low energy measurements of the B 10 (p,α) Be 7 reaction,” *Phys Rev C*, vol. 95, no. 4, Apr. 2017, doi: 10.1103/PhysRevC.95.044617.

[15] A. J. Hidy *et al.*, “A new 7Be AMS capability established at CAMS and the potential for large datasets,” *Nucl Instrum Methods Phys Res B*, vol. 414, pp. 126–132, Jan. 2018, doi: 10.1016/j.nimb.2017.11.017.

[16] A. Caciolli *et al.*, “A new study of 10B(p, α)7Be reaction at low energies,” *European Physical Journal A*, vol. 52, no. 5, May 2016, doi: 10.1140/epja/i2016-16136-8.

[17] A. Caciolli, “Nuclear Astrophysics at LNL: The 25Mg(α,n)28Si and 10B(p,α)7Be cases,” in *Journal of Physics: Conference Series*, Institute of Physics Publishing, Jan. 2018. doi: 10.1088/1742-6596/940/1/012035.

[18] G. G. Rapisarda *et al.*, “Study of the 10B(p, α1)7Be reaction by means of the Trojan Horse Method,” *European Physical Journal A*, vol. 54, no. 11, Nov. 2018, doi: 10.1140/epja/i2018-12622-3.

[19] L. Lamia *et al.*, “Boron depletion: indirect measurement of the 10B(p,α)7Be S(E)-factor,” *Nucl Phys A*, vol. 787, no. 1-4 SPEC. ISS., pp. 309–314, May 2007, doi: 10.1016/j.nuclphysa.2006.12.049.

[20] A. N. N. M. BOESGAARD, “STELLAR ABUNDANCES OF LITHIUM, BERYLLIUM, AND BORON,” *Publications of the Astronomical Society of the Pacific*, vol. 88, no. 524, pp. 353–366, 1976, [Online]. Available: http://www.jstor.org/stable/40675939

[21] C. ~P. Deliyannis, “Lithium and Beryllium as diagnostics of stellar interior physical processes,” in *Stellar Clusters and Associations: Convection, Rotation, and Dynamos*, R. Pallavicini, G. Micela, and S. Sciortino, Eds., in Astronomical Society of the Pacific Conference Series, vol. 198. Jan. 2000, p. 235.

[22] R. Depalo *et al.*, “New direct measurement of the 10B(p, α)7Be reaction with the activation technique,” in *EPJ Web of Conferences*, EDP Sciences, Dec. 2017. doi: 10.1051/epjconf/201716501021.

[23] L. Mabit and W. Blake, *Assessing recent soil erosion rates through the use of beryllium-7 (Be-7)*. Springer International Publishing, 2019. doi: 10.1007/978-3-030-10982-0.

[24] H. Nagai, W. Tada, and T. Kobayashi, “Production rates of 7Be and 10Be in the atmosphere,” *Nucl Instrum Methods Phys Res B*, vol. 172, no. 1, pp. 796–801, 2000, doi: https://doi.org/10.1016/S0168-583X(00)00124-5.

[25] E. A. Maugeri *et al.*, “Preparation of 7Be targets for nuclear astrophysics research,” *Journal of Instrumentation*, vol. 12, no. 2, Feb. 2017, doi: 10.1088/1748-0221/12/02/P02016.

[26] S. ~M. ~R. Puglia *et al.*, “Study of the ^10B(p,alpha )^7Be reaction via the Trojan Horse Method .,” *Memorie della Societa Astronomica Italiana Supplementi*, vol. 14, p. 43, Jan. 2010.

[27] T. Rauscher and G. Raimann, “Astrophysical reaction rates for 10 B"p,… 7 Be and 11 B"p,… 8 Be from a direct model,” 1996.

[28] F. W. E. Strelow, R. Rethemeyer, and C. J. C. Bothma, “Ion Exchange Selectivity Scales for Cations in Nitric Acid and Sulfuric Acid Media with a Sulfonated Polystyrene Resin,” *Anal Chem*, vol. 37, no. 1, pp. 106–111, 1965, doi: 10.1021/ac60220a027.

[29] S. L. Queern *et al.*, “Production of Zr-89 using sputtered yttrium coin targets 89Zr using sputtered yttrium coin targets,” *Nucl Med Biol*, vol. 50, pp. 11–16, Jul. 2017, doi: 10.1016/j.nucmedbio.2017.03.004.

[30] W. J. Huang, M. Wang, F. G. Kondev, G. Audi, and S. Naimi, “The AME 2020 atomic mass evaluation (I). Evaluation of input data, and adjustment procedures,” *Chinese Physics C*, vol. 45, no. 3, Mar. 2021, doi: 10.1088/1674-1137/abddb0.

[31] M. Wang, W. J. Huang, F. G. Kondev, G. Audi, and S. Naimi, “The AME 2020 atomic mass evaluation (II). Tables, graphs and references,” *Chinese Physics C*, vol. 45, no. 3, Mar. 2021, doi: 10.1088/1674-1137/abddaf.

[32] J. M. Donaldson and F. Trowell, “Dissolution of Elemental Boron.,” *Anal Chem*, vol. 36, no. 11, p. 2202, Oct. 1964, doi: 10.1021/ac60217a057.

[33] J. Korkisch, *Handbook of Ion Exchange Resins: Their Application to Inorganic Analytical Chemistry Volume VI*. Boca Raton / London / Tokyo: CRC Press, 2017. doi: 10.1201/9781315140520.

[34] J. Korkisch, *Handbook of Ion Exchange Resins: Their Application to Inorganic Analytical Chemistry Volume 5*. New York, 1989.

[35] S. Schwarz *et al.*, “The low-energy-beam and ion-trap facility at NSCL/MSU,” *Nucl Instrum Methods Phys Res B*, vol. 204, pp. 507–511, 2003, doi: https://doi.org/10.1016/S0168-583X(02)02122-5.

[36] “Virtual tour.” Accessed: Mar. 22, 2024. [Online]. Available: https://nscl.msu.edu/public/virtual-tour.html

[37] S. P. Kalinin, A. A. Ogloblin, and Yu. M. Petrov, “Excitation functions for the reactions Li7(p. n)Be7, B10(p.α)Be7, and B11(p. n)C11, and energy levels in Be8, C11, and C12 nuclei,”

*The Soviet Journal of Atomic Energy*, vol. 2, no. 2, pp. 193–196, 1957, doi: 10.1007/BF01832091.

[38] A. J. Koning, D. Rochman, J. C. Sublet, N. Dzysiuk, M. Fleming, and S. van der Marck, "TENDL: Complete Nuclear Data Library for Innovative Nuclear Science and Technology," *Nuclear Data Sheets*, vol. 155, pp. 1–55, 2019, doi: 10.1016/j.nds.2019.01.002.

# APPENDIX

## $^{7}$Be PRODUCTION CALCULATIONS

Table C.1: Theoretical $^{7}$Be activities are shown for the $^{10}$B(p,α)$^{7}$Be reaction, for each Type II target.

| # target | t irradiation [h] | I [μA] | μA*h | A, predicted [μCi] |
|---|---|---|---|---|
| 4 | 3 | 5 | 15.0 | 2542.6 |
| 5 | 6 | 6 | 36.0 | 6102.2 |
| 6 | 4 | 6 | 24.0 | 4068.1 |
| 7 | 7 | 6 | 42.0 | 7119.3 |
| 5+7 | | | 78.0 | 13221.5 |
| | | | **Sum** | **19832.2** |

Table C.2: Theoretical $^{7}$Be activities are shown for the $^{10}$B(p,α)$^{7}$Be reaction, for each Type I target.

| # target | t irradiation [h] | I [μA] | μA*h | A, predicted [μCi] |
|---|---|---|---|---|
| 1 | 0.5 | 5 | 2.5 | 54.8 |
| 2 | 0.5 | 10 | 5.0 | 109.6 |
| 3 | 1 | 10 | 10.0 | 219.2 |
| | | | **Sum** | **383.6** |

# CHAPTER 6: CONCLUSIONS AND RECOMMENDATIONS

To summarize, the Isotope harvesting program at NSCL/FRIB has been identified as a source of otherwise-difficult-to-obtain radioisotopes for use in multiple basic and applied research fields. The goal of this dissertation was to establish a solid-phase isotope harvesting program, complement the already existing aqueous-phase and gaseous-phase isotope harvesting program, and establish proof of concept methodologies which also find wide applicability in studies at different facilities aiming towards the extraction and chemical processing of different radionuclides from solid targets.

As FRIB ramps up beam power for the higher production of radioisotopes, more accelerator parts like beam dumps, fragment catchers, mass slits, will become available for harvesting opportunities in the future. This necessitated testing on components such as the decommissioned beam blocker from NSCL and other materials that were part of this dissertation. Moreover, at FRIB, the complexity of extraction chemistry is anticipated to increase due to the considerable size of the aqueous beam dump, approximately 8000 L, and the prolonged residence time of several hours for radionuclides before encountering the extraction medium, which makes solid-phase isotope harvesting approach a viable alternative [1], [2], [3].

Establishing this solid-phase isotope harvesting approach in this dissertation composed of achieving four aims viz. harvesting $^{88}$Zr from a tungsten target, where a proof-of-concept irradiation was carried out at NSCL with tungsten foils (commonly used material at FRIB and other radioactive ion beam facilities), and (92.3 ± 1.2)% $^{88}$Zr was recovered. Moreover, the long-lived isotopes of zirconium hold significant importance in practical nuclear research. Hence, the exploration of solid-phase extraction methods for zirconium was a valuable pursuit, particularly

when considering the challenges associated with extracting it from aqueous solutions, as discussed in Chapter 1 and Chapter 2.

Having understood chemistry of tungsten and zirconium from the experiment in Chapter 2, the knowledge was utilized in designing methodologies for processing the tungsten beam-blocker where $^{172}$Hf was extracted from the tungsten beam-blocker and other co-embedded radionuclides followed by establishing the $^{172}$Hf/$^{172}$Lu generator and the $^{172}$Lu generated was used for PAC experiments. This was followed by comparison of generators set up with those from the conventional method to produce $^{172}$Hf (through the proton irradiation of a natural lutetium target) where the generators on different resins were eluted cyclically to carry out PAC and radiolabeling studies with the ZR resin set up as the higher activity generator. Additionally, the ease of separation, elution, and the long shelf-life of the $^{172}$Hf/$^{172}$Lu generator system makes it suitable for experiments where pure lutetium isotope is needed and procuring $^{177}$Lu is not always feasible. Furthermore, beryllium and boron chemistry was also explored with the production of $^{7}$Be, its separation from boron target material, source preparation efforts, and $^{7}$Be beam delivery. In all cases, experiments were first conducted with stable elements, to understand the chemistry of the selected element and then replicated with radionuclides.

**6.1 Chemical methodologies applicability**

The techniques and methodologies developed in this work will find applicability in chemical separation to extract Hf and Zr isotopes from irradiated tungsten parts in the accelerator beamline at heavy-ion beam facilities like FRIB. These extracted radioisotopes can then be used to establish generators that will provide pure daughter radioisotopes for an extended period of time.

Other facilities harboring tungsten parts are the European Spallation Source (ESS) in Sweden, Los Alamos Neutron Science Center (LANSCE) facility at Los Alamos National Laboratory (LANL), and the Spallation Neutron Source (SNS) at Oak Ridge National Laboratory (ORNL) amongst others. At the ESS, the heavy metal, tungsten target is a 2.6 m diameter stainless steel disk/wheel weighing almost five tons [4]. At the LANSCE facility, a water-cooled tungsten target assembly is used to produce spallation neutrons [5]. The SNS facility houses a rotating tungsten target, which is hit by a 700-kilowatt proton beam resulting in spallation [6].

When the tungsten parts at these facilities are decommissioned or have run their service period, many exotic radionuclides can be harvested due to years of operation. There can be many other components in the beamline that would accumulate radionuclides due to years of operation at these facilities as well.

**6.2 Future work**

Conducting the experiments mentioned in this thesis also resulted in the identification of future directions to investigate to improve these methodologies. Further scope for improvement remains in the context of the purified fractions from the tungsten beam-blocker generators to achieve radiopurity. While it was not a major obstacle for PAC experiments, radiopurity needs to be achieved for radiolabeling study purposes, followed by exploration of more novel ligand systems to bind the eluted $^{172}$Lu. For the radiolanthanides eluted from the LN resin with the load solution fractions in Chapter 3, further separation can be achieved using a DGA resin column to harvest the radiolanthanides as well apart from $^{172}$Hf. Furthermore, entrapped gases can be harvested from the tungsten beam-blocker. More novel ligand systems can also be synthesized and explored for chelation with $^{172}$Lu eluted from higher activity ZR resin generator set up in Chapter 4. In context of $^{7}$Be, the BMIS extraction efficiency can be improved.

Further exploration can be conducted into additional materials suitable for online implantation and activation that are capable of regeneration between experiments. Among the promising candidates are vitreous carbon and alumina, known for their ability to withstand high temperatures and resistance against beam damage during irradiation. Notably, these materials have large surface to volume ratios, meaning that embedded radionuclides would be close to surfaces. This proximity to the surface streamlines the removal process via an acid wash post-irradiation, or could allow thermal distillation in an ISOL-like process.

Furthermore, depending on the end use of the harvested radionuclides, the purity of the beam at the location of the collector must be considered. In instances where solid collections occur on the slits of mass separators, encountering less mass and a potentially smaller array of radionuclides compared to those found in the beam dump is expected due to the prior selectivity in the fragment separator at this point.

### 6.3 Final remarks

Through this work, different target materials like tungsten, lutetium, and boron have been tested and chemical methodologies were developed, and the first true test of the solid-phase harvesting capabilities at the NSCL was demonstrated. The insight gained from the experiments performed here will lead to successful solid-phase harvesting experiments at FRIB to produce and collect useful radionuclides. The capability to harvest and study rare isotopes has significant implications in fields like nuclear medicine, where they are used for diagnosis and treatment, as well as in basic scientific research to understand the fundamental properties of matter. Additionally, considering the specific radionuclide under investigation and the desired balance between quantity and purity, certain modes may present advantages over others. Therefore, it is

imperative to thoroughly explore all avenues through which the nuclear science community can harness the wealth of radionuclides generated at FRIB.

## REFERENCES


[1] A. Visser and N. Scielzo, “Feasibility of Harvesting Radon from FRIB Beam Dump,” *Llnl-Tr-709438*, 2016.

[2] M. Avilov *et al.*, “Thermal, mechanical and fluid flow aspects of the high power beam dump for FRIB,” *Nucl Instrum Methods Phys Res B*, vol. 376, pp. 24–27, 2016, doi: 10.1016/j.nimb.2016.02.068.

[3] S. Satija *et al.*, “Harvesting 88Zr from heavy-ion beam irradiated tungsten at the National Superconducting Cyclotron Laboratory,” *Applied Radiation and Isotopes*, vol. 197, p. 110831, 2023, doi: https://doi.org/10.1016/j.apradiso.2023.110831.

[4] “How the ESS Target works,” 2024, Accessed: Mar. 22, 2024. [Online]. Available: https://europeanspallationsource.se/target/how-it-works

[5] A. T. Nelson, J. A. O’Toole, R. A. Valicenti, and S. A. Maloy, “Fabrication of a tantalum-clad tungsten target for LANSCE,” *Journal of Nuclear Materials*, vol. 431, no. 1–3, pp. 172–184, Dec. 2012, doi: 10.1016/j.jnucmat.2011.11.041.

[6] “Second Target Station Target Systems ,” 2024, Accessed: Mar. 22, 2024. [Online]. Available: https://sns.gov/sts/sts-target-systems